

Western  Graduate&PostdoctoralStudies

Western University  
Scholarship@Western

---

Electronic Thesis and Dissertation Repository

---

1-15-2013 12:00 AM


# The Study of Optoelectronics in Semiconductor and Metallic Nanoparticle Hybrid Systems

Daniel G. Schindel  
*The University of Western Ontario*

Supervisor  
Dr. Mahi R. Singh  
*The University of Western Ontario*

Graduate Program in Physics  
A thesis submitted in partial fulfillment of the requirements for the degree in Doctor of Philosophy  
© Daniel G. Schindel 2013

Follow this and additional works at: <https://ir.lib.uwo.ca/etd>

 Part of the [Condensed Matter Physics Commons](#), [Optics Commons](#), and the [Quantum Physics Commons](#)

---

## Recommended Citation

Schindel, Daniel G., "The Study of Optoelectronics in Semiconductor and Metallic Nanoparticle Hybrid Systems" (2013). *Electronic Thesis and Dissertation Repository*. 1136.  
<https://ir.lib.uwo.ca/etd/1136>

This Dissertation/Thesis is brought to you for free and open access by Scholarship@Western. It has been accepted for inclusion in Electronic Thesis and Dissertation Repository by an authorized administrator of Scholarship@Western. For more information, please contact [wlsadmin@uwo.ca](mailto:wlsadmin@uwo.ca).

THE STUDY OF OPTOELECTRONICS IN SEMICONDUCTOR AND  
METALLIC NANOPARTICLE HYBRID SYSTEMS  
(Spine title: The study of Optoelectronics in Nanoparticle Hybrid Systems)  
(Thesis format: Integrated Article)

by

Daniel Schindel

Graduate Program in Physics

A thesis submitted in partial fulfillment  
of the requirements for the degree of  
Doctor of Philosophy

The School of Graduate and Postdoctoral Studies  
The University of Western Ontario  
London, Ontario, Canada

© Daniel Grant Schindel 2013

# Abstract

The Study of Optoelectronics in Semiconductor and Metallic Nanoparticle Hybrid Systems

by

Daniel Schindel

Department of Physics and Astronomy

The University of Western Ontario

This thesis examines optoelectronics of photonic crystals and photonic nanofibers, especially with quantum dots and metallic nanoparticles doped into them. The simulations produced focus on the quantum dots, which are presented in an ensemble of 3-level systems.

In order to consider a photonic nanofiber in isolation, a model was developed for the density of photonic states. We studied two profiles, a square cross-section and a circular cross-section. In addition, we consider two architectures, one where a photonic crystal surrounds a dielectric fiber, and one where the fiber is another photonic crystal. We found several photonic nanofibers with a single bound photonic state and calculated the density of states.

We studied dipole-dipole interactions through photon absorption in three-level quantum dots doped in a photonic nanofiber. The density matrix method was used to calculate the absorption coefficient and the mean field approximation was used to incorporate dipole-dipole interactions. It was found that a transparent state can become an absorbing state if the dipole-dipole interactions are switched on. It is also predicted that one absorbing peak can be split into two absorbing peaks through judicious selection of the resonance energies of the quantum dots and the location of the bound photon state in the nanofiber.

We calculated the energy transfer and photoluminescence in donor and acceptor quantum dots which were embedded in a nonlinear photonic crystal. These quantum dots interacted

via the dipole-dipole interaction. It was found that the photoluminescence of the acceptor quantum dot could be controlled by a pump laser.

We have also studied the interactions between a metallic nanosphere and a quantum dot embedded on a dielectric substrate. Dipole-dipole interactions between them caused energy absorption, evaluated with the density matrix method. The absorption spectrum was found to switch from one peak to two peaks when the intensity of the control laser increased. Adding a metallic nanosphere can also cause splitting. Additionally, fluorescence efficiency in the quantum dot was found to be quenched by the presence of the metallic nanosphere.

Finally, we studied quantum coherence and interference phenomena in a quantum dot and metallic nanorod hybrid system. It was predicted that the power absorption spectrum of the metallic nanorod can be switched from two transparent states to one transparent state by the control laser.

These findings can be used to create ultrafast all-optical switching and sensing nanodevices. Also, the systems discussed here have applications in photovoltaics, quantum computation, and cryptography, among others.

**Keywords:** dipole-dipole, nanofiber, photoluminescence, photonic crystal, quantum dot, plasmon-polariton

*To my parents*

*Rick and Maureen Schindel*

## Acknowledgements

I would like to express my heart-felt thanks to my supervisor, Prof. Mahi R. Singh, whose encouragement, insight, discernment, and most of all patience, has made my time here at Western a wonderful experience. Without his guidance, inspiration, and his knack for explaining things clearly and unequivocally, this would have been a far more arduous process. He has helped me more than I can say.

I would like to thank my parents, Maureen and Rick Schindel, for proofreading, and especially for their support during the final push to finish this document. Their love and support has been instrumental in my continued progress, and a bountiful source of strength and inspiration.

I owe a lot to my colleagues, Ali Hatef, Joel D. Cox, and Chris Racknor for many helpful discussions and assistance in preparing my presentation. In particular, I would like to thank Ali and Chris, who co-authored two of the chapters in this thesis, for their assistance. I would also like to thank Prof. Aaron Sigut for his help and encouragement.

I would also like to thank Joel Cox, Prof. Mike Cottam, Dr. Reinhard Helbing, Kathy Meadows, and Rev. Steve Johnston for proofreading. Special thanks goes to Clara Buma, Anne Brooks, and Jodi Guthrie for taking care of business.

I also wish to thank my 3 pastors for their prayers and support, Pastor Jim for many enlightening and encouraging discussions that helped place things in perspective, Pastor Bob for several delightful talks over lunchtime, and Pastor Steve for many phone calls that helped keep me on track. Everyone at Trinity Lutheran Church has been a great source of enthusiasm and endurance. In particular I'd like to mention the choir where I sang, the Men's Club, and the 'lunch bunch.' Your support and fellowship has really seen me through this. I especially appreciate Laurie, Kathy, Reinhard, and Vivian for their support.

Finally, thank you to my whole family, a rock and foundation that can weather any storm. Thank you to my extended family, and my younger brother Adam who never fails to make me laugh. Thank you for your prayers everyone, and with God's help I can do my best.

## List of Abbreviations

DDI	dipole-dipole interaction
DOS	density of states
EBP	electron-bound photon
EIT	electromagnetically induced transparency
ETR	energy transfer rate
FCC	Face-Centred Cubic
MNP	metallic nanoparticle
MNR	metallic nanorod
MNS	metallic nanosphere
PL	photoluminescence
QD	quantum dot
SPP	surface plasmon-polariton
TE	transverse electric
TM	transverse magnetic

# Contents

<b>Abstract</b>	<b>ii</b>
<b>Dedication</b>	<b>iv</b>
<b>Acknowledgements</b>	<b>v</b>
<b>List of Abbreviations</b>	<b>vi</b>
<b>List of Figures</b>	<b>ix</b>
<b>1 Introduction</b>	<b>1</b>
1.1 Photonic Crystals and applications . . . . .	1
1.2 Thesis outline . . . . .	11
<b>2 Fundamentals</b>	<b>14</b>
2.1 Photonic Crystals and Photonic Nanowires . . . . .	14
2.1.1 Photonic Crystal Fabrication and Doping of Quantum Dots . . . . .	17
2.1.2 Photonic Nanowires . . . . .	19
2.2 Quantum Dots . . . . .	22
2.3 Metal Nanoparticles . . . . .	27
<b>3 The theory of cylindrical photonic wires</b>	<b>29</b>
3.1 Introduction . . . . .	29
3.2 Photonic Crystal Wires . . . . .	31
3.2.1 Cylindrical Wire . . . . .	33
3.2.2 Rectangular Wire . . . . .	34
3.2.3 Dielectric Wires . . . . .	36
3.3 Results and Discussion . . . . .	37
3.4 Conclusion . . . . .	42
<b>4 Photon absorption in interacting quantum dots doped in nanofibers</b>	<b>44</b>
4.1 Introduction . . . . .	44
4.2 Dipole-dipole interaction in photonic nanowires . . . . .	47
4.3 Density of States . . . . .	50
4.4 Dipole-Dipole Interaction . . . . .	51
4.5 Density Matrix Method . . . . .	52
4.6 Reduced Density Matrix . . . . .	53



4.7	Density Matrix Equations for a 3-level Quantum Dot . . . . .	54
4.8	Electric susceptibility . . . . .	55
4.9	Simulations of the Absorption Coefficient . . . . .	59
4.10	Conclusion . . . . .	65
<b>5</b>	<b>Controlling the photoluminescence of acceptor and donor quantum dots embedded in a nonlinear photonic crystal</b>	<b>66</b>
5.1	Introduction . . . . .	66
5.2	Quantum Dot Energy Transfer . . . . .	67
5.3	Interaction Hamiltonian . . . . .	71
5.4	Density Matrix Method . . . . .	72
5.5	Energy Transfer Mechanism . . . . .	73
5.6	Results and Discussion . . . . .	75
5.7	Conclusion . . . . .	79
<b>6</b>	<b>The study of fluorescence in a quantum dot and metallic nanosphere hybrid system</b>	<b>80</b>
6.1	Introduction . . . . .	80
6.2	Quantum Dot embedded on a Dielectric Medium . . . . .	82
6.3	External Electric Fields . . . . .	84
6.4	Interaction Hamiltonian . . . . .	85
6.5	Quantum Dot-Metallic Nanosphere Hybrid System . . . . .	86
6.6	Density Matrix Formulation . . . . .	90
6.7	Power Absorption and Fluorescence efficiency . . . . .	91
6.8	Results and Discussion . . . . .	92
6.9	Conclusion . . . . .	97
<b>7</b>	<b>Dipole-dipole interaction in a quantum dot and metallic nanorod hybrid system</b>	<b>99</b>
7.1	Introduction . . . . .	99
7.2	Exciton-plasmon coupling . . . . .	101
7.3	Density Matrix Method . . . . .	103
7.4	The Energy Exchange . . . . .	105
7.5	Results and Discussion . . . . .	105
7.6	Conclusion . . . . .	110
<b>8</b>	<b>Concluding Remarks</b>	<b>111</b>
	<b>Bibliography</b>	<b>114</b>
	<b>Copyright and Reprint Permissions</b>	<b>124</b>
	<b>Curriculum Vitae</b>	<b>131</b>

# List of Figures

2.1	Potential geometries for 2D and 3D photonic crystals. Note that they have periodic arrangements of dielectric materials so as to reflect light in multiple directions. . . . .	15
2.2	Dispersion relation for a simple photonic structure in 1 dimension, showing a single valence and conduction band. Note the band gap where photons cannot propagate. . . . .	16
2.3	A log cabin geometry for a photonic crystal. 4 layers are shown in different colours for a photonic crystal. Each layer consists of rods of the same material. . . . .	18
2.4	A wire shape with a square cross section cut out of a larger material. For all wires considered in this document, the larger material is a photonic crystal, but the central region may be a dielectric or another photonic crystal. That is, the blue region, region B is a photonic crystal. Region A is also a photonic crystal, but may be replaced by region C, a dielectric. In figure (b), we see the band structure for this system when there is a photonic crystal in the centre. A photon of energy $\varepsilon_p$ is confined within the wire. In figure (c), there is a dielectric material C in the wire, but the photon is still confined to the wire. . . . .	20
2.5	A two-dimensional photonic crystal with two waveguides. If this is a thin sheet, the waveguides may be nanofibers. Quantum dots are shown resting on the surface of the thin sheet, effectively doped into the interior of the nanofiber. . . . .	21
2.6	A substrate with a resist being exposed. First, the substrate is coated with a resist, and then an electron beam exposes a portion of the resist in the desired shape of the eventual quantum dot. . . . .	24
2.7	A substrate with a quantum dot laid down. The exposed portion of the resist was removed by a developer, and then a layer of the desired material for the quantum dot was laid down. . . . .	25
2.8	A substrate with only the quantum dot remaining. The resist was dissolved away, taking the excess material with it. . . . .	25
2.9	A V-type 3-level quantum dot. The only disallowed transition is the $ 2\rangle \leftrightarrow  3\rangle$ transition. . . . .	26
2.10	A ladder-type 3-level quantum dot. The only disallowed transition is the $ 1\rangle \leftrightarrow  3\rangle$ transition. . . . .	27
2.11	A $\Lambda$ -type 3-level quantum dot. The only disallowed transition is the $ 1\rangle \leftrightarrow  2\rangle$ transition. . . . .	27

3.1	Here we see a cross-section of two photonic crystals with different photonic crystal wires running through them. On the left, we have a circular cross-section, and on the right it is square. Each photonic crystal in this example uses the same materials, the only difference being the lattice constant. The lattice constant though, is enough to make the difference between photonic crystal <i>A</i> and photonic crystal <i>B</i> . . . . .	31
3.2	Density of States for our Photonic Nanowire, with a square cross-section. Note that the well is nominally between 0.381 and 0.399 eV, and the second and fourth states shown here have degeneracies. . . . .	39
3.3	Density of States for our Photonic Nanowire, with a circular cross-section. Note that there is only a single TE mode. Any other photonic states in this wire would either be a TM or a hybrid mode. . . . .	40
3.4	Allowed photon modes in a photonic nanowire with a square cross-section and a dielectric core. . . . .	41
3.5	Allowed photon modes in a photonic nanowire with a circular cross-section and a dielectric core. . . . .	42
4.1	Schematic diagram is shown for a photonic nanofiber (top view). The nanofiber is made from embedding a dielectric material into a photonic crystal <i>A</i> . Quantum dots are doped into the embedded material. . . . .	46
4.2	Schematic diagram of a three-level quantum dot. The levels are denoted by $ 1\rangle$ , $ 2\rangle$ , and $ 3\rangle$ . A control laser couples $ 3\rangle$ and $ 1\rangle$ whereas a probe laser couples $ 2\rangle$ and $ 1\rangle$ . Levels $ 3\rangle$ and $ 2\rangle$ decay to level $ 1\rangle$ due to the electron-bound photon interaction. . . . .	47
4.3	The absorption coefficient $Im(\chi_{dd}/\chi_0)$ is plotted as a function of the normalized probe detuning $\delta_{21}$ when the control field is absent. The solid and dashed lines correspond to $C_{21} = 0$ and $C_{21} = 2$ , respectively. Note that the absorption peak shifts to the right due to the DDI. Linewidths are calculated when both resonance energies $\varepsilon_{21}$ and $\varepsilon_{31}$ lie far away from $\varepsilon_{00}$ . . . . .	61
4.4	The absorption coefficient $Im(\chi_{dd}/\chi_0)$ is plotted as a function of the normalized probe detuning $\delta_{21}$ when the control field is present. The solid and dashed lines correspond to $C_{31} = 0$ and $C_{31} = 5$ , respectively. Note that the absorption peak splits into two peaks due to the dipole-dipole coupling $C_{31}$ . The $C_{21}$ coupling is taken as $C_{21} = 2$ . Linewidths are calculated when both resonance energies $\varepsilon_{21}$ and $\varepsilon_{31}$ lie far away from $\varepsilon_{00}$ . . . . .	62
4.5	In this figure, the effect of the EBP interaction due to the linewidth $\Gamma_{31}$ is presented. The absorption coefficient $Im(\chi_{dd}/\chi_0)$ is plotted as a function of the normalized probe detuning $\delta_{21}$ when the control field is present. Parameters are taken as $C_{31} = 5$ and $C_{21} = 2$ . The solid, dashed, and dotted lines are calculated when resonance energy $\varepsilon_{31}$ lies at 1330, 1260 and 1256, respectively. . . . .	63
4.6	The normalized DOS is plotted as a function of energy near the photon bound state $\varepsilon_{00}$ . . . . .	64

5.1	Schematic diagram of a three level atom embedded in the photonic crystal. The parameters used in the present calculation are taken as $n_a = 1.59$ , $n_b = 1$ , $a = 100$ nm, and $L = 400$ nm. The band gap of this photonic crystal has been calculated to lie between energies $\varepsilon_v = 1.031$ eV and $\varepsilon_c = 1.358$ eV. The induced dipole moment of the QD is taken as $\mu_{12} = \mu_{23} = 0.4$ e nm and its dielectric constant is $\varepsilon_d = 6$ . The vacuum decay rates for the QD are taken as $\Gamma_2^0 = \Gamma_3^0 = 1$ $\mu$ eV. . . . .	69
5.2	Power loss from the donor QD as a function of probe field detuning, $\delta_2$ , for $I_p = 0$ GW/cm <sup>2</sup> (dashed curve) and $I_p = 60$ GW/cm <sup>2</sup> (dotted curve). Inset: DDI parameter is plotted as a function of $I_p$ . . . . .	76
5.3	PL efficiency as a function of donor to acceptor QD separation, $R$ , for $I_p = 0$ GW/cm <sup>2</sup> (dashed curve) and $I_p = 60$ GW/cm <sup>2</sup> (dotted curve). Inset: PL efficiency is plotted as a function of $R$ in the absence of interference. Dashed and dotted curves represent $I_p = 0$ GW/cm <sup>2</sup> and $I_p = 60$ GW/cm <sup>2</sup> , respectively. . . . .	78
6.1	An ensemble of 3-level quantum dots deposited on a substrate. The black dots are QDs. The QD has three states, $ 1\rangle$ , $ 2\rangle$ , and $ 3\rangle$ . . . . .	83
6.2	A 3-level quantum dot with a nearby metallic sphere and two external fields applied to this system. The probe field, $\omega_2$ excites the ground state of the quantum dot and the control field, $\omega_3$ drives the metal sphere at its resonance frequency while exciting the quantum dot to the uppermost level. The dipole-dipole interaction (DDI) couples the metal nanosphere to the quantum dot. The complete system would consist of an ensemble of quantum dots interacting with a metal nanosphere atop a dielectric substrate. . . . .	87
6.3	Power Absorption due to the quantum dot as a function of probe detuning, plotted in ns <sup>-1</sup> . The solid curve has no MNS, and $I_c = 0$ W/m <sup>2</sup> , the dotted curve has no MNS, and $I_c = 40$ W/cm <sup>2</sup> , the dashed curve also has no MNS, and $I_c = 800$ W/cm <sup>2</sup> . . . . .	94
6.4	Power Absorption due to the quantum dot as a function of probe detuning, plotted in ns <sup>-1</sup> . The solid curve has no MNS, the dotted curve has an MNS, but only with the $\Pi_3$ component of the dipole-dipole interaction. The dashed curve has the full dipole-dipole interaction, including the $\Lambda_3$ term. . . . .	95
6.5	Power Absorption due to the quantum dot as a function of probe detuning, plotted in ns <sup>-1</sup> . The solid, dotted and dashed curves are plotted for $R = 11$ nm, 14 nm, and 50 nm, respectively. . . . .	96
6.6	Power Absorption due to the quantum dot as a function of the distance between the quantum dot and metal sphere. The solid curve shows power loss without DDI effects, and the dotted curve shows the power loss with DDI effects. Note that the solid curve has a constant value of 0.028 pW. . . . .	97
6.7	Fluorescence Efficiency in the quantum dot as a function of the distance between the quantum dot and the metal sphere. . . . .	98
7.1	A schematic diagram of the quantum dot and metallic nanorod. . . . .	100

7.2	$W_m$ (W) is plotted as a function of $\delta_{12}$ ( $\text{ns}^{-1}$ ) where the solid curve and dashed curve correspond to when only the probe field or both the probe and control fields are applied, respectively. The control field has an intensity of $I_c = 10 \text{ W/cm}^2$ . . . . .	106
7.3	$W_m$ (W) is plotted as a function of $\delta_{12}$ ( $\text{ns}^{-1}$ ) where the solid and dashed curves are plotted for ellipticity ratios of $l_m/r_m = 4$ and $l_m/r_m = 1.2$ , respectively. The control field has an intensity of $I_c = 10 \text{ W/cm}^2$ . . . . .	107
7.4	$W_m$ (W) is plotted as a function of $\delta_{12}$ ( $\text{ns}^{-1}$ ). The solid and dashed curves correspond to $I_c = 0.4 \text{ W/cm}^2$ and $I_c = 10 \text{ W/cm}^2$ , respectively. . . . .	108
7.5	$W_m$ (W) is plotted as a function of $\delta_{12}$ ( $\text{ns}^{-1}$ ) with $I_p = 0.1 \text{ W/cm}^2$ and $I_c = 0.5 \text{ W/cm}^2$ . The solid curve and dashed curve correspond to $R = 13 \text{ nm}$ and $R = 15 \text{ nm}$ , respectively. . . . .	109

# Chapter 1

## Introduction

### 1.1 Photonic Crystals and applications

The aim of this thesis is to study optoelectronic properties of quantum dots and metallic nanoparticles doped in photonic crystals and photonic crystal nanofibers. The field of photonic crystals has seen a plethora of study and has impacted a wide variety of other fields because of the current and future potential applications in optoelectronic and all-optical devices [1], [2], [3], [4], [5]. With photonic crystals and photonic nanofibers, the optical properties are determined not only by the bulk atomic structure properties, but also by the geometry of where the groups of atoms are placed. In other words, visible light implies a length scale of a few hundred nanometers, so optical photonic crystals behave according to shapes of  $\sim 100 - 1000$  nm in length, in addition to the properties of atomic structures of sizes  $\sim 0.1 - 1$  nm. The simplest photonic crystal is often called a Bragg reflector, and was first described by Lord Rayleigh in 1888 [6]. This simple reflector qualifies as a 1-dimensional photonic crystal, but 2- and 3-D photonic crystals were not produced until one hundred years later [7], [8]. It should be mentioned though, that these were cm-scale constructs which affected microwaves, but optical photonic crystals didn't have to wait another hundred years. [9].

Photonic crystals reflect light because they have photonic bands which are separated by a band gap in their photonic energy spectrum. Unlike metallic reflectors, which absorb most of the photons that manage to penetrate the surface, photonic crystals absorb virtually nothing

and simply don't have any allowed modes for propagation within the band gap of the crystal. When the wavelength of light lies within the bands of the photonic energy spectrum, light passes through and the photonic crystal transmits the light. However, when the wavelength of the light in question lies within the band gap, the light is totally reflected. In that case, the photonic crystal acts as a reflector [7], [8], [10], [11], [12], [13], [14], [15], [16], [17].

One reason this field is such a diverse and fertile area of study is that smaller and faster optoelectronic devices are seen as important. Photonic nanofibers, which are long cylinders which confine light to a line with a thickness in the nanometer scale, would qualify as a promising field to produce such devices [15], [18]. The terms photonic nanowire and nanofiber will be used interchangeably in this document, as their theoretical treatment is identical. The purpose of a nanofiber in a photonic circuit is to transmit light and possibly select frequencies to block or allow through.

It is also possible to use an ensemble of quantum dots to allow some frequencies of light through, while others are preferentially absorbed. Strictly speaking, they don't need to have the same length scales as the photonic structures discussed above, but the photons that they absorb and emit can depend on the size and shape of the dot, rather than depending only on the bulk properties of the materials used. In other words, while the sizes of quantum dots are much smaller than the wavelengths of light in question, their optoelectronic properties depend strongly on the size of these quantum dots. That is, quantum dots have energy levels which can be adjusted significantly when the sizes of the quantum dots are changed. In that sense, quantum dots can be an integral part of a photonic circuit, defined as a series of photonic wires connecting elements which modify light in more interesting ways [19], [20], [21], [22], [23]. Quantum dots were first built in the early 1980s by two groups, [24], [25] but the term 'quantum dot' was not used until 1988 [26].

While a 1-D photonic crystal has been around for a long time, a 0-D photonic object (a box with inward facing mirrors) did not strike the authors of the Bragg reflector as particularly useful. More recently, 0-D, 1-D, and 2-D photonic objects have found applications in lab-

on-chip devices, [27], quantum computation, [28], cryptography, [29], optical switching, [30], optical detection, [31], etc. [14], [15], [32], [33], [34]. To be clear on terminology here, a gap between two 1-D photonic crystals creates a 2-D photonic object. A 3-D photonic object is simply a dielectric, since light is free in all directions. Therefore, a 0-D photonic object usually requires a 3-D photonic crystal to confine light in all 3 dimensions. The 1-D photonic heterostructure, where photons are confined to a line, would then typically require at least a 2-D photonic crystal to fabricate. These have been referred to as photonic nanofibers to emphasize the connection to fiber-optic cables, or as photonic nanowires to emphasize how photons are confined within the wire. The nanowire term also helps illustrate connections between semiconductor confinement of electrons and photonic crystal confinement of photons. In other words, the photonic band gap in photonic crystals is analogous to the electronic band gap in semiconductors, and the nanowire term emphasizes this more than the nanofiber term.

Some of these items require some additional clarification. In [27], photonic crystals are used to slow the propagation of light down so that there is more opportunity for absorption. Then, infrared light is used, at a frequency where methane absorbs strongly. In this way, the device is an efficient methane detector. In [28], a photonic crystal waveguide, of the type depicted in figure 2.5, was used to couple two photonic cavities. In the first cavity, quantum dots emitted into a cavity mode, and in the second, single photons from the first cavity were observed. In this way, a photonic fiber was used to connect two elements in a potential photonic circuit, for use in quantum information processing. In [29], a 2-D photonic crystal cavity with 1 or 2 quantum dots inside is used as a source for single photons of a predefined energy, direction, and polarization. The use for quantum cryptography is that this source is needed. This need is illustrated in [35], where a broad description of many different schemes for quantum cryptography is given. The first of which involves a set of bits sent from Alice to Bob to be measured in either the + basis or the X basis. If eavesdropping takes place, 25% of the eavesdropped on bits will be wrong, and normal error correction methods which are necessary would detect this eavesdropping. Thus, the single photon generation with a



well-defined polarization is indeed a requirement for this type of encoding.

To further describe some of the results referenced here, in [30], a non-linear photonic crystal made of polystyrene and air is used as an ultrafast switch, shifting a band gap, so that light will be blocked and one end or allowed through at the other. In this way, a non-linear photonic crystal can, by itself, form an ultrafast all-optical switch. In [31], a photonic crystal fiber is used to confine a light beam, and then probe molecules such as DNA or antibodies are used to coat the inner surface of the air-holes within the photonic crystal (2D). A thin layer of some protein would then attach to the probe molecules, creating a thin layer with a different index of refraction, but enough to detect the molecules in question.

Photonic nanowires or nanofibers technically describe any construct in which light is confined to a line of nanoscopic thickness, but in this document, we restrict ourselves to those made with photonic crystals. Nanowires have some highly unusual optical properties. One example of such a property being quantized photonic states. A broad range of new optical devices have been, and are being produced [13], [14], [33], [36]. Photonic nanowires by themselves though, can only provide a backdrop to adjust the flow of light. To exert control over that light, it is usually helpful to have other nanostructures involved. This control can be achieved when nanoparticles such as quantum dots are doped into photonic nanowires.

Photonic nanowires, also known as photonic nanofibers, can form a photonic circuit element with only the addition of quantum dots. When photonic fibers are doped with quantum dots, it often enables the fiber to act as a switch for certain frequencies of light. That is, when quantum dots are present in a photonic nanowire, one laser can turn on or off the transparency of the nanowire to another laser. Our technique for studying the coupling between quantum dots which are embedded in a photonic environment is that we consider dipole-dipole interactions (DDI) between quantum dots. The photonic environment for chapters 3 and 4 is a photonic nanofiber, for chapter 5 it is a photonic crystal substrate, and for chapters 6 and 7 it is simply a dielectric substrate. Our techniques have identical structure, in principle, whether using photonic or polaritonic crystals, which have a band gap due to the interactions between

phonons and the electronic structure rather than designed shapes of materials. That is, polaritonic crystals, like photonic crystals, have a photonic band gap, it just arises from a different mechanism. Polaritonic crystals are not considered here though, since they typically have a band gap in the microwave region, and we prefer the optical regime [11], [16], [17].

For photonic cavities (0-D objects) and photonic fibers (1-D objects) the usual method for measuring how much a photonic or polaritonic crystal will ‘leak’ photons is through the quality factor,  $Q$ . The quality factor is defined as the ratio of the energy stored in a resonator to the power loss within that resonator, multiplied by the resonant angular frequency of the waves in question. However, this is not what is typically measured. Measurements of the quality factor are generally performed in terms of the location of the resonant frequency and the width of the resonant peak. For all practical purposes, these definitions are equivalent, with the common measured quantity being:

$$Q = \frac{f_r}{\Delta f} \quad (1.1)$$

In the above,  $f_r$  is the resonant frequency, and  $\Delta f$  is full-width half-maximum of the cavity’s steady-state vibration spectrum. The quality factor has been measured and calculated for many different types of fibers and wave guides, several of which made use of photonic crystals. The  $Q$  factor is derived from transmission or absorption spectra of bound photon states. Values for the  $Q$  factor have been observed as high as 40 000 in some systems, and even as high as 600 000 [15], [16], in certain optical cavities designed with photonic crystals.

Whether making photonic crystal cavities, nanowires, or other nanostructures, the emphasis is usually on the production of smaller and faster optoelectronic devices. Photonic nanowires, or nanofibers, are studied here and can be made from photonic crystals [15], [18]. It is worth mentioning, given that the first description of photonic crystals themselves was only twenty-five years ago, nanophotonics is still an emerging research area. Photonic nanofibers have been produced with a significant and complete band gap in the optical spectrum. This affords a similar level of control over photons as semiconductors have for electrons [7], [8], [10], [11],

[12], [13], [14], [15], [16], [17].

As with semiconductors, photonic nanowires are promising structures, since they have many optical characteristics which would enable them to form the basis of many optical devices [13], [14], [33], [36]. Among the possible fields of application are quantum computation, optical switching, and optical detection [14], [15], [32], [33], [34], [37]. Investigating these systems may enhance our understanding of optoelectronic and nanoscale science.

When an oscillating external electromagnetic field is present, dipole moments will be induced in any quantum dots in the system. These induced dipole moments interact with each other. This interaction between quantum dots is called the dipole-dipole interaction (DDI). One common technique for evaluating the effects of the DDI is the local field approximation, wherein the DDI has been studied for atomic systems and nanostructures [38], [39], [40], [41]. Other phenomena that the DDI influences include quantum entanglement [42], quantum jumps [43], and resonance fluorescence [44] in two coupled atoms. Atomic gases have also shown several interesting new effects when DDI effects have been included, such as the enhancement of inversionless gain and index of refraction, or ultrafast optical switching.

For further clarification, in [42], the degree to which states of 2 two-level quantum dots are entangled are examined as a function of the distance between the quantum dots. The interactions between quantum dots which allow states to become entangled are dipole-dipole interactions here. In [43], ‘quantum jumps’ are investigated which result from dipole-dipole interactions between two ladder-type three-level quantum dots. A quantum jump is shown to be a situation where one dot is emitting light consistently, but then the other dot begins emitting at the same time that the first dot goes dark. This phenomenon was modeled to arise from dipole-dipole interactions between the quantum dots. In [44], the fluorescence of two quantum dots is investigated for two Lambda-type three-level dots with dipole-dipole interactions. They found that under some circumstances, the ‘steady state’ contains persistent oscillations in the observed fluorescence.

Interesting new effects arising from the DDI have been studied in photonic crystals as well

[45], [46], [47], [48]. Two noteworthy instances of DDI effects would be self-induced transparency and spontaneous emission, in this case in a photonic crystal doped with two-level atoms [45]. Also considered previously by Dr. Singh are the effects of the DDI using the mean field approximation in nanoparticles [46], [47], [48], [49], [50]. Other significant effects considered by him include electromagnetically induced transparency and the spontaneous emission cancellation, which have been calculated for photonic crystals doped with multi-level nanoparticles [46], [47], [48]. He has also studied a selected electronic transition's ability to inhibit two-photon absorption [49], [50]. Photonic crystals constitute an important way to adjust how photons will interact with nanoscopic systems.

Quantum dots are not the only nanoscopic systems where energy transfer is of current interest. In particular, metallic nanostructures have been considered in conjunction with quantum dots [51], [52]. Quantum dots have excitation energies defined by their size, so their tailored characteristics have been used to study the optical properties of metallic, biological, and chemical nanosystems [51], [52], [53]. Many optical properties can be significantly enhanced by the addition of metallic nanostructures. This enhancement is due to the interaction between the electromagnetic field from localized surface plasmons on the metallic nanostructure and the exciton within the quantum dot. Among the phenomena which these hybrid systems have been used to investigate are light harvesting [54] and surface plasmon-enhanced fluorescence [55].

To further elucidate, in [51], a two-level quantum dot is considered in the presence of a metal nanoparticle. They investigate interference effects between the dipole field of the quantum dot and the external field at the metal nanoparticle. This results in power loss in the metal nanoparticle having an asymmetric minimum. In [54], a two-level quantum dot is placed near one of several metal nanorods arranged in the form of a Yagi-Uda antenna which is resonant with the quantum dot transition frequency. This is used to enhance the directionality and uniform polarization of emission from the quantum dot. In this way, light is harvested by the quantum dot, and emitted in a preferred direction. In [55], two-level quantum dots are

considered in the presence of a rough metal substrate. Fluorescence from the quantum dots are enhanced three-fold or more. Thus, non-localized surface plasmons enhance the fluorescence of the quantum dots.

In particular, many studies have focused on fast optical switching mechanisms. In several chapters, we consider interactions between optical excitations of the components of the system in question, either quantum dots, metal nanospheres or nanorods, and point out transparent states which may be switched on or off. Optical excitations in quantum dots are excitons which arise due to transitions between discrete levels in the conduction and valence bands. The excitations in the metallic nanorod are called localized surface plasmons, which are nothing but collective oscillations of conduction band electrons. The surface plasmons arise from the dielectric contrast between the nanorod and the non-conductive environment. The resonance frequency of localized surface plasmons can be controlled by the shape and size of the metallic nanoparticle. When light of the right frequency is incident on a metal nanoparticle, it results in surface plasmon-polaritons. Interactions between excitons and localized surface plasmons occur when a metal nanoparticle and a quantum dot are in close proximity. In this hybrid system, the optical excitation frequencies of the two constituents are resonant with one another. A large variety of metal nanostructures have been used to study exciton-plasmon interactions such as gold, aluminum and silver.

For photovoltaic applications, quantum dots possess certain advantages over organic dyes. For example, their photon absorption and emission depends on the size of the quantum dots, they emit at a narrow and stable frequency, and quantum dots have a much higher quantum yield than conventional organic dyes [56]. Quantum dots have been used to label nano- and microscopic structures for biological imaging and sensing [57]. While quantum dots do emit at a narrow and stable frequency, they have a broad absorption spectra, which means they make excellent donors of light energy. Two additional hybrid systems based on quantum dots are solar cells [58] and bio-sensing [59]. Systems such as these take advantage of resonant energy states to drive energy from donor quantum dots to acceptor quantum dots. The mechanism

for this energy transfer is DDIs between quantum dots. These DDIs depend on the distance between the quantum dots, and the overlap between the resonance energies of the donor and acceptor quantum dots. Several quantum dot-based biosensors have been developed [59].

Many studies have been recently performed in the field of plasmonics within nanoscopic systems containing multiple elements. Plasmons, particularly when confined to a finite metal object, will often be far more localized than photons of the same energy. This can enable plasmons to transfer photon-excited energy better than photons. Efficient exciton-plasmon-photon conversion has been demonstrated, which means that quantum dots and metallic nanoparticles can produce many promising structures [54], [60], [61], [62]. Entanglement, for one thing, survives the conversion processes among these three energy packets, so several geometries involving quantum dots and metal nanoparticles have been considered for quantum information processing [63], [64], [65]. In addition, metal nanostructures have been investigated regarding the possibility of a two q-bit gate [65], [66]. The metal nanostructures we wish to consider further are metal nanoparticles near quantum dots.

For further clarification, in [60] and [61], energy transfer from an exciton to a surface plasmon on a long nanowire is demonstrated. At the end of the nanowire, emission of photons is observed. Efficient generation of surface plasmons from excitons is demonstrated. In [63] and [64], quantum dots are not present. Two entangled photons are created, one of them passes through a metal film. This excites a plasmon which reradiates the photon on the other side of the film. Entanglement of the final photon to its pair which did not pass through any film was found to be maintained. In [65], 2 two-level quantum dots are placed with a metal nanowire between them. The plasmons which travel between the quantum dots enable the quantum dots to become entangled. In [66], 2 three-level Lambda-type quantum dots are coupled by a metal nanowire between them. They then devise a 2-qbit quantum gate based on this coupling. This gate is meant to invert the phase of one and only one possible state of the system.

Quantum dots and metal nanoparticles have been coupled by linker molecules, [67], [68],

but these are not always necessary [69], [70], [71]. Some other examples of systems involving this pair of nanostructures are: fluorescence enhancement in the quantum dot, [72], [73], [74], [75], altering emission rates for the quantum dot, [76] enhancement of the Fano effect, [77], [78], as a pulse controller for a quantum dot, [74], and electromagnetically induced transparencies [51], [52], [79]. With regards to the shape of the metal nanoparticle, nanorods, nanospheres, and nanodiscs have been investigated, [69], [73], [80] and also multiple nanospheres [81].

To further outline some of these results, in [72], a metal sphere attached to an armature is maneuvered close to a two-level quantum dot. In the presence of the metal sphere, fluorescence of the quantum dot is enhanced. Also, the models used in this reference claim that plasmon dipole excitations are not significant, instead quadrupole excitations are more significant. In [73], a two-level quantum dot is considered in the presence of a metal nanorod. The simulations here show fluorescence enhancement in the quantum dot, and also energy loss in the metal, which shows the same behaviour as in [51]. In [74], a two-level quantum dot is considered in the presence of a metal nanosphere. The simulations here show fluorescence enhancement in the quantum dot, and also the metal sphere acts as a pulse controller for the quantum dot. In [75], silver nanodiscs are used to enhance fluorescence in two-level quantum dots. The polarization of the light in question is shown to make a significant difference between the absorption spectra for these quantum dots.

For additional clarification, in [76], a metal nanorod was placed near a two-level quantum dot. Emission rates for the quantum dot in the presence of the nanorod were calculated. Several configurations were considered as well as the ellipticity of the rod. In [77], a two-level quantum dot is examined in the presence of a metal nanosphere. A Fano peak, where interference between background photons and resonant excitations produces an asymmetric profile, is enhanced with the presence of the metal nanosphere. In [78], a two-level quantum dot is investigated in the presence of a metal nanosphere. In these simulations, fluorescence is enhanced by the metal sphere, and a Fano peak is also enhanced. In [79], a two level quantum

dot is considered in the presence of a metal nanosphere. The power loss in the metal was calculated to have the same type of behaviour seen in [51]. Also, a double-Fano peak was found for this system.

In this document, nanospheres and nanorods are considered as partners to quantum dots. The number of possible hybrid materials that can be built from existing nanostructures is enormous [51], [76], [78], [82], [83], [84], [85], [86], [87], [88]. The combination of a quantum dot and a metallic nanorod has been studied, [76] as well as a metal-dielectric nanoshell [88]. Another example would be [51] and [78], where studies of the effects of weak and strong exciton-plasmon coupling regimes on the power absorption in a QD-metallic nanoparticle system were undertaken by the authors. A three-level quantum dot interacting with a metallic nanoparticle in the presence of two external fields has been studied for both a ladder-type [83] and a V-type configuration [84], [85], [86], and [87].

## 1.2 Thesis outline

The thesis is organized as follows. In chapter 2 we have explained the fundamental physics needed to understand the thesis. For example, we have explained the basic physics of photonic crystals, quantum dots, and metallic nanoparticles.

In chapter 3, the energy modes for a photonic nanowire have been studied and calculated. We model our photonic crystals after reference [89], where logs of semiconductor material are stacked to produce photonic band gaps in both the near and far infrared regions. A nominal dispersion relation consistent with photonic crystals was adopted in order to achieve qualitatively useful results. Photonic wires were modeled in two schemes, each with two specific geometries. In the first scheme, a pillar of one photonic crystal is embedded in a larger photonic crystal to produce a wire. This pillar was modeled as having either a square or a circular cross section. In each case, the photonic density of states was calculated,



to describe the optical properties of the nanowire. The second scheme investigated was a dielectric material for the central pillar, rather than a photonic crystal. Again, circular and square cross sections were considered. It was found that many more modes fit into the near infrared band gap than the far infrared band gap, and that a circular cross section permits fewer modes. Finally, a dielectric pillar allows for a wire which is physically much smaller than a wire with a photonic crystal in the middle. As many photonic devices include such wires, these qualitative results could be useful in their design.

In chapter 4, we study the coupling between quantum dots through the dipole-dipole interaction in photonic nanofibers manufactured by embedding a dielectric material into a photonic crystal. The embedded dielectric material is doped with an ensemble of three-level quantum dots. A probe field is applied to monitor the absorption and a control field is applied to induce dipole moments in quantum dots. Dipoles are induced in quantum dots due to the external fields, and they are interacting with each other via the dipole-dipole interaction. Quantum dots are also interacting with the nanofiber through the electron-bound photon interaction. The absorption coefficient has been calculated using the density matrix method, and the dipole-dipole interaction has been evaluated in the mean field approximation. It is found that the absorption spectrum splits from one peak to two peaks in the presence of the dipole-dipole interaction. The splitting of peaks can be controlled by either the resonance energy of quantum dots or bound photon states of the nanofiber.

In chapter 5, we have studied energy transfer and photoluminescence in donor and acceptor quantum dots embedded in a nonlinear photonic crystal. The quantum dots are interacting with each other via the dipole-dipole interaction. The nonlinear photonic crystal modifies the dielectric constant of the quantum dots. Using the density matrix method, it is found that the energy transfer and photoluminescence in a donor quantum dot can be controlled by the pump field due to the nonlinearity of the photonic crystal. Additionally, our theoretical calculations agree with recent experiments [90], [91], [92]. This hybrid system can be used to fabricate ultrafast switching and sensing nanodevices.

In chapter 6, we studied energy absorption and interference in a quantum dot-metallic nanosphere system embedded on a dielectric substrate. A control field is applied to induce dipole moments in the nanosphere and the quantum dot, and a probe field is applied to monitor absorption. Dipole moments in the quantum dot or the metal nanosphere are induced by the external fields and each other's dipole fields, and they interact via the dipole-dipole interaction. The density matrix method was used to show that the absorption spectrum can be split from one peak to two peaks by the control field, and this can also be done by placing the metal nanosphere close to the quantum dot. In addition, the fluorescence efficiency can be quenched by the addition of a metal nanosphere. Again, it would be possible to produce ultrafast switching and sensing nanodevices using this hybrid system.

In chapter 7, we have studied quantum coherence and interference phenomena in a quantum dot (QD)-metallic nanorod (MNR) hybrid system. Probe and control laser fields are applied to the hybrid system. Induced dipole moments are created in the QD and the MNR and they interact with each other via the dipole-dipole interaction. Using the density matrix method, it was found that the power spectrum of the MNR has two transparent states, and they can be switched to one transparent state by the control field. Here also, ultrafast switching and sensing nanodevices could be produced using this model.

In chapter 8, the main results of the thesis are summarized. Also, possible future research directions have been proposed.

# Chapter 2

## Fundamentals

In this thesis we studied hybrid systems which are made from photonic crystals, quantum dots, and metal nanoparticles. Therefore, this chapter will review some basic properties of each of these constructs.

### 2.1 Photonic Crystals and Photonic Nanowires

In this section, basic properties inherent to photonic crystals will be discussed. The defining characteristic of photonic crystals is the reflection of light via interference effects from reflections at material interfaces. That is, a photonic crystal consists of a periodic arrangement of alternating layers of two different dielectric materials. A schematic diagram for two dimensional and three dimensional photonic crystals is shown in figure 2.1. In that figure, the two dielectric materials are shown as being red and yellow, with indices of refraction of  $n_A$  and  $n_B$ . The two materials are shown as having the same thickness in each direction, but these can be different. The two or three lengths involved could also be different, but then the band gaps would be different for each direction you consider. If the reflections interfere constructively, light will be unable to propagate through the crystal, and total reflection will be observed. In

1 dimension, this is called a Bragg reflector. For reflections in multiple directions, we call it a photonic crystal. An example of other kinds of reflection would be in metals where electric fields are simply excluded by the high concentration of ‘free’ charges.

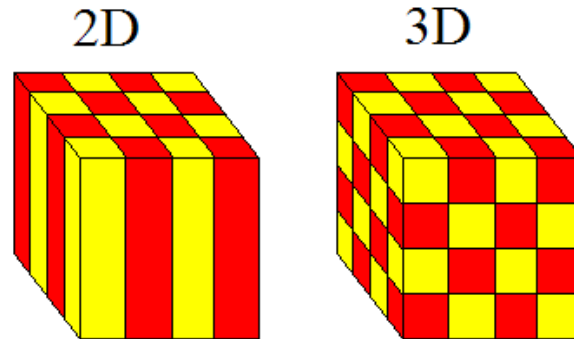


Figure 2.1: Potential geometries for 2D and 3D photonic crystals. Note that they have periodic arrangements of dielectric materials so as to reflect light in multiple directions.

An important feature of photonic crystals is that they have photonic bands, and these bands are separated by band gaps in which there is no propagation of light. The band referred to here is meant to evoke the semiconductor conduction and valence bands for electrons, which are separated by a band gap. One difference between the two is that photons are not bound to atoms, so they do not come with an energy level structure which is the origin of the band structure in solids. Instead, the band gaps in photonic crystals result from multiple reflections interfering constructively. That is, in a semiconductor, the atomic energy levels and the gaps between them result in bands and band gaps. In a photonic crystal, interference effects result in band gaps. One example of a photonic crystal would be silica for the red material and air for the yellow. Some other examples include titania and air, titania and silica, and aluminum arsenide and air. In figure 2.2, the dispersion relation, i.e. a plot of energy,  $\epsilon$ , vs. wave vector,  $k$ , for a simplified photonic crystal is shown.

Some other features of figure 2.2 are worth mentioning. Near the band edge there is a region where the effective index of refraction is large, since the slope here is small. In other words, the speed of light in this material is slow, since the slope of the energy vs. wave vector curve is small. This means that the effective index of refraction for that frequency

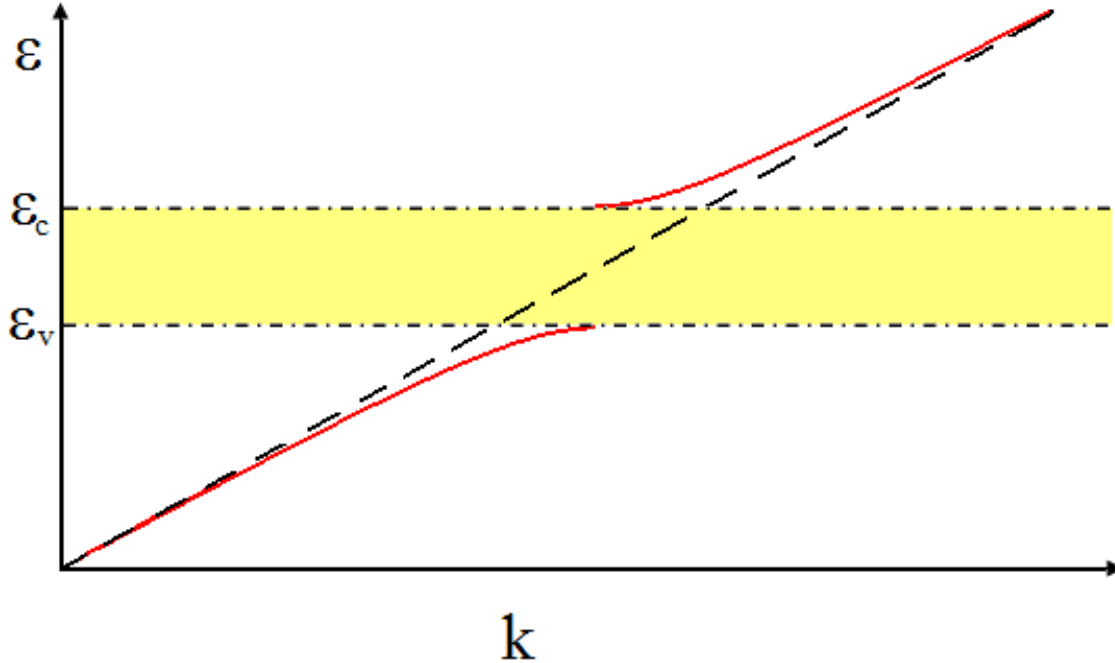


Figure 2.2: Dispersion relation for a simple photonic structure in 1 dimension, showing a single valence and conduction band. Note the band gap where photons cannot propagate.

is large. In real photonic crystals the dispersion relation tends to be highly directional [93]. For microwaves, where photon wavelengths are comparable in size to Lego blocks, photonic crystals as shown in figure 2.1 are attainable [94]. Note that for a 3D photonic crystal at typical ultraviolet wavelengths of  $\sim 10$  nm, this would be akin to stacking quantum dots. The dispersion relation for a photonic crystal in the visible spectrum is of interest for this thesis.

Given that the defining characteristic of a photonic crystal is the existence of a photonic band gap, the defining parameters for an extant photonic crystal tend to be the size, location, and directionality of the band gap in question [95]. The gap-to-midgap ratio, for example, is often used, [96] and it is defined as:

$$r_{gm} = \frac{2(\varepsilon_c - \varepsilon_v)}{\varepsilon_c + \varepsilon_v} \quad (2.1)$$

where  $\varepsilon_c$  is the energy at the upper edge of the band gap and  $\varepsilon_v$  is the energy at its lower edge. These letters are chosen to emphasize the similarities with semiconductors, where conduction

and valence bands exist. All models used here ignore any absorption within photonic crystals, so any skin depth that may be reported would not be considered here.

One way to increase the size of a band gap is to increase the refractive index contrast between the two materials used. It is worthwhile to have large band gaps, since the larger they are, the more control one would have in adjusting the behaviour of light within an arrangement of photonic crystals.

The simplest way to increase refractive index contrast is to have one high index material, such as silica, and let everything else be air or vacuum, which do not absorb significantly. Metals typically have a real part of their refractive index which drops below one, but this always accompanies some absorption [97].

It is worth pointing out that all photonic crystals discussed in this thesis are assumed to be isotropic. This would seem to be a problematic assumption to make, considering that no completely isotropic photonic crystals have yet been produced. However, omnidirectional band gaps do exist, so photonic crystals which have been produced have some frequencies which are excluded in every direction. These photonic crystals may be anisotropic in their band structure, but they do possess band gaps. The model employed in this thesis produces a band gap, so in any particular direction, the physics is correct. It is only when one considers the whole structure does the problem of anisotropic band structures arise. Also, the purpose of these calculations is to simulate qualitatively accurate effects, and not necessarily to provide quantitatively exact results. The isotropic model for photonic crystals is sufficient for that purpose.

### **2.1.1 Photonic Crystal Fabrication and Doping of Quantum Dots**

In this section, techniques to produce photonic crystals will be discussed. One way to produce a photonic crystal with a band gap in 3 dimensions is to arrange spheres periodically in a container, fill the empty spaces with a background material, and dissolve the spheres away [98].

This leaves air spheres with a background material acting as a photonic crystal. Another technique involves a photosensitive material which is exposed to several lasers that interfere constructively in order to cross the intensity threshold for exposure, after which either the exposed or unexposed portion is dissolved [89]. The geometry in that reference is also different, in that their crystal follows the ‘log cabin’ approach. This is where the high-index material is arranged in rods in a perpendicular cross-hatch, where one layer has lines parallel to the x-axis, and the next layer has lines parallel to the y-axis, as seen in figure 2.3. If the low index of refraction material is air or a vacuum, then that leaves a lot of empty space in which objects smaller than 100 nm or so (such as quantum dots) may be placed.

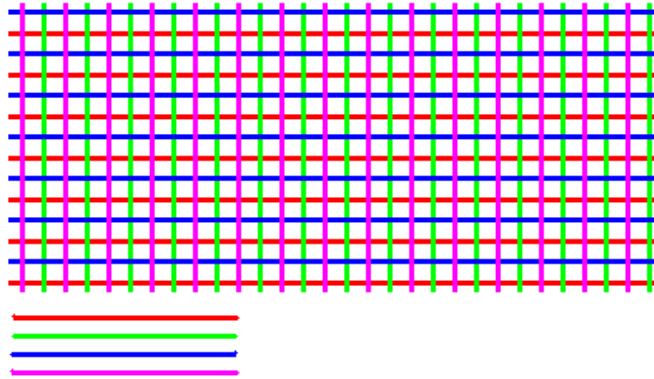


Figure 2.3: A log cabin geometry for a photonic crystal. 4 layers are shown in different colours for a photonic crystal. Each layer consists of rods of the same material.

Many of the results discussed in this thesis rely on having an ensemble of quantum dots within a photonic crystal. The dispersion relation of the photonic crystal, and the specific geometry of the system enables us to affect density of photonic states at the location of the quantum dots. The density of states is defined as the number of k-space photon modes allowed in the system per unit energy. That is,

$$D(\varepsilon) = \frac{dN}{d\varepsilon} = c_n(k) \frac{dk}{d\varepsilon} \quad (2.2)$$

where  $D$  is the density of states,  $k$  is the wave vector of photons,  $N$  is the number of allowed

photon modes, and  $c_n(k)$  is a prefactor that depends on the geometry of the system in question. The subscript  $n$  refers to the number of dimensions in the system. The density of states, in turn, affects the decay rates for the various energy levels of the quantum dots, as per Fermi's golden rule. Thus, we wish to have quantum dots doped into the photonic crystal, which is to say that we want them dispersed within the photonic crystal or dielectric which defines the photonic circuit element we wish to simulate. Many photonic crystals have a large fraction of their volume as air [99], [100]. If this is the case, a liquid can be filtered through the crystal, and then removed. In some cases, this liquid can be a solution of quantum dots, many of which are left behind in the photonic crystal structure [101]. Since the typical dimensions of a photonic crystal unit cell are  $\sim 500$  nm for visible light, and the dimensions of a typical quantum dot are  $\sim 3$  nm, quantum dots do not interfere with light propagation through the photonic crystal except when an exciton is excited.

Another technique for doping quantum dots into photonic crystals is to use ultrasound to disperse quantum dots into the photonic crystal structure, i.e. sonication [102]. If the doping is to be done into a photonic nanowire or certain other structures, it can be accomplished effectively by growing them on top of the structure, prior to the formation of the photonic crystal [103]. The growth of quantum dots is discussed in section 2.2, and the doping process is discussed at the end of section 2.1.2. The process relies on the specific geometry for the nanowire.

### **2.1.2 Photonic Nanowires**

In this section, different types of structures made from different photonic crystals will be discussed. Nanowires, or nanofibers, are fabricated by embedding a cylindrical section of a photonic crystal or dielectric material into an existing photonic crystal. The light is free to move along the interior of the cylinder, and it is confined in the perpendicular directions. This configuration is shown in figure 2.4. Note that a photonic crystal is still a composite structure.



A cross section is shown in figure 3.1 for a photonic crystal core, or figure 4.1 for a dielectric core with quantum dots. For reference, the 1-dimensional band structure is shown in figure 2.4b and 2.4c. The interior of the nanowire in that figure is either a dielectric and labeled as C, or labeled as photonic crystal A. The photonic crystal that forms the background of everything is labeled as photonic crystal B. Thus, the energies displayed in that figure are:  $\epsilon_{cB}$ , the conduction or upper band edge for photonic crystal B,  $\epsilon_{cA}$ , the conduction or upper band edge for photonic crystal A,  $\epsilon_{vB}$ , the valence or lower band edge for photonic crystal B,  $\epsilon_{vA}$ , the valence or lower band edge for photonic crystal A, and  $\epsilon_p$ , the energy of a trapped photon.

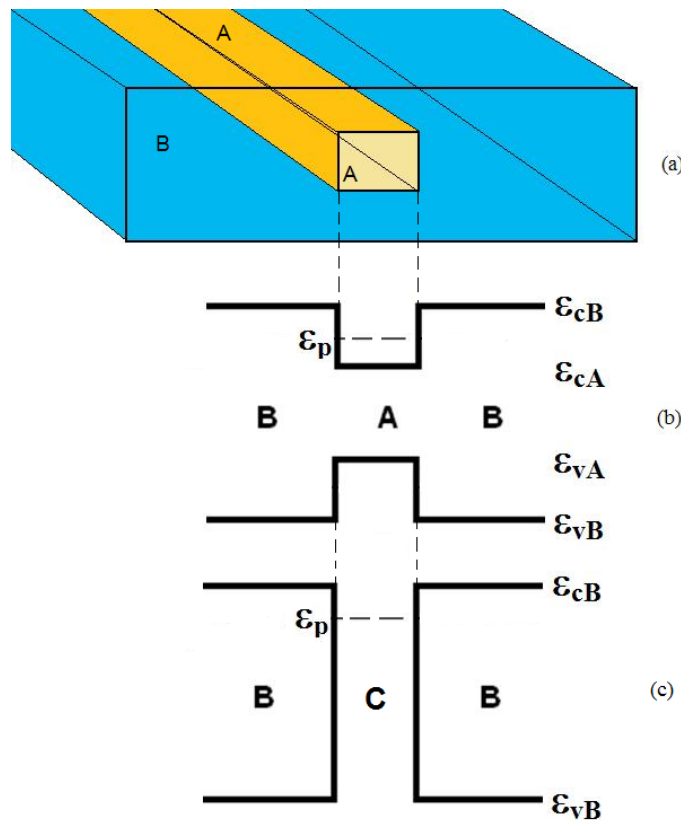


Figure 2.4: A wire shape with a square cross section cut out of a larger material. For all wires considered in this document, the larger material is a photonic crystal, but the central region may be a dielectric or another photonic crystal. That is, the blue region, region B is a photonic crystal. Region A is also a photonic crystal, but may be replaced by region C, a dielectric. In figure (b), we see the band structure for this system when there is a photonic crystal in the centre. A photon of energy  $\epsilon_p$  is confined within the wire. In figure (c), there is a dielectric material C in the wire, but the photon is still confined to the wire.

A completely different geometry for a photonic nanofiber is a flat sheet with holes drilled in

it so that it acts as a photonic crystal in the two dimensions of the plane of the flat sheet. This is shown in figure 2.5. In the upper half of that flat sheet, there is a continuous 2D photonic crystal, and below that is a horizontal region where light in the band gap may pass through. Thus, light is confined by the photonic crystal in the direction from the top of the diagram to the bottom, and is free to propagate horizontally. In addition, the thin, flat sheet confines the light due to total internal reflection. In this way, light can be confined on nanoscopic scales by two different mechanisms.

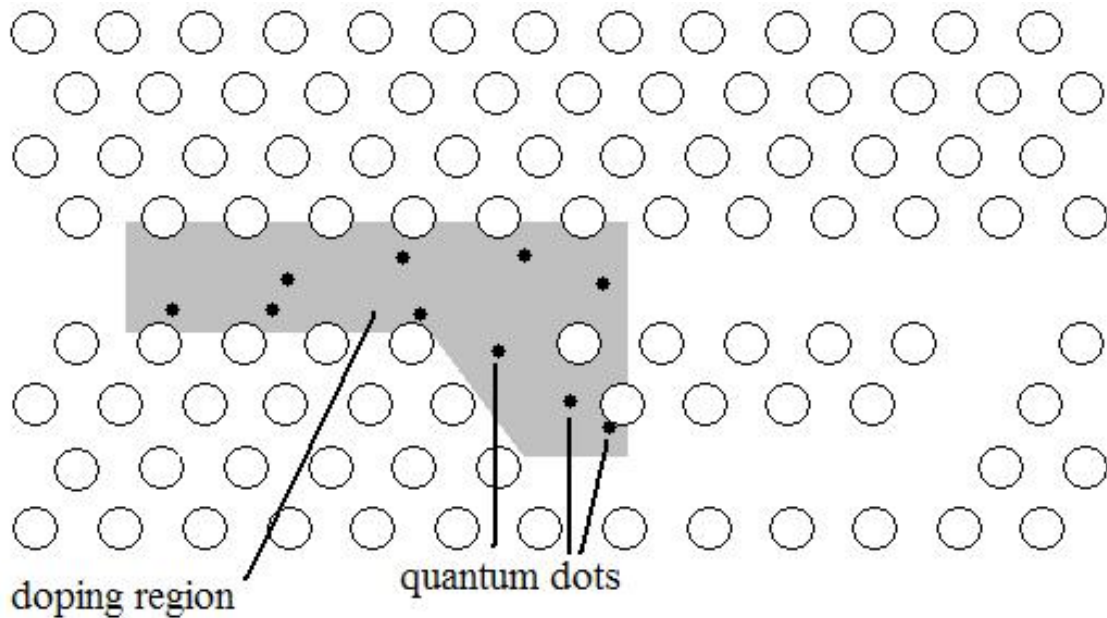


Figure 2.5: A two-dimensional photonic crystal with two waveguides. If this is a thin sheet, the waveguides may be nanofibers. Quantum dots are shown resting on the surface of the thin sheet, effectively doped into the interior of the nanofiber.

Another facet of figure 2.5 is the quantum dots which lie on the surface of the nanofiber. Given the typical sizes mentioned, quantum dots would be much smaller than depicted, and presumably there would be more of them. Also, according to the fabrication method of figures 2.6-2.8, the quantum dots can be grown in place prior to etching out the circles of figure 2.5. This means that, for that fabrication method, the photonic nanofiber shown in figure 2.5 would be appropriate. This method produces quantum dots attached to a surface, and the evanescent field of any light passing through the nanofiber would be able to interact

with quantum dots on the surface. Therefore, quantum dots are interacting with the photon modes which are confined to photonic nanofiber. Finally, this scheme can lay out nanofibers according to a desired circuit pattern, and quantum dots can form a photonic circuit element. Just what that circuit element does is the subject of each chapter. However, it is worth noting that the geometry of figure 2.5 is not discussed further in this document, only the geometry of figure 2.4.

## 2.2 Quantum Dots

In this section, some basic properties as well as fabrication methods for quantum dots will be discussed. Quantum dots are studied further in chapters 4, 5, 6, and 7. A quantum dot is defined as any nanoscopic structure with a small number of discrete energy levels. Given that an atom satisfies these criteria, but is around 10 to 100 times smaller, (diameter, not volume) quantum dots are sometimes referred to as artificial atoms. Typically, quantum dots are spheres that are around 3 nm in diameter, and are made of semiconductors such as CdTe or GaAs. It may be sufficient to confine an electron with a homogeneous nanostructure, but it is sometimes preferable to have additional confinement. This can be achieved if a sphere of one semiconductor is surrounded by a shell of another semiconductor, when the band structure is set up similar to figure 2.4b. Electrons are confined in a quantum dot and have quantized energy levels which for a spherical dot are:

$$E_n = \frac{s_{nl}^2 \hbar^2}{2mR^2} \quad (2.3)$$

where  $s_{nl}$  is the normalization factor associated with the  $n^{\text{th}}$  zero of the  $l^{\text{th}}$  spherical Bessel function of the first kind,  $m$  is the mass of an electron, and  $R$  is the radius of the inner sphere. This is only an approximation, derived for an impenetrable spherical boundary. In a real quantum dot there would be some penetration of the wave function into the shell. The main point here

being that the energy levels of a quantum dot can be set at desired levels by adjusting the size of the quantum dots in question. For the purposes of this thesis, however, the internal structure of a quantum dot is largely ignored, and an energy-level structure is assumed. Quantum dots hold localized excitons and they interact with photons and each other through dipole-dipole interactions.

However, it is worth examining briefly how quantum dots are produced. After all, any theoretical calculation remains a thought experiment until something physical is built based on that calculation. One way to create quantum dots is through molecular beam epitaxy. In molecular beam epitaxy, atoms are laid down on a substrate at an arbitrarily slow rate, such that one has enough control to lay down one layer of one species, followed by a single atomic layer of another species. When molecular beam epitaxy is used to produce a slab of one material on top of a slab of another material, the lattice constants of the two materials in question need to match. For a single layer this doesn't really matter, the new species will simply fit itself onto the lattice of the substrate, but with successive layers, the bulk properties of the new material will assert itself, and its lattice structure will eventually take over. If the mismatch is too great, the new material won't form nice single layers anymore, but instead form 'bubbles' or 'islands' where the new material builds up. These structures, while consisting of a wide variety of sizes, do function as quantum dots [104].

Another method of producing quantum dots, one which provides significantly more control over the energy levels of the finished product, also employs molecular beam epitaxy. This sort of quantum dot works best with the nanowire geometry found in figure 2.5. To produce this sort of quantum dot, one starts with a substrate coated in a thin layer of something that will dissolve, known as a resist. A desired pattern (such as a circle for a disc-shaped quantum dot) is then etched into the resist. This is done with an electron beam to alter the chemical structure of the resist in a pre-defined area. This can be seen in figure 2.6. A developer removes only the exposed portion of the resist, and a layer of metal or semiconductor is laid down. This phase is shown in figure 2.7. Finally, the remainder of the resist is dissolved away leaving a

quantum dot on the surface of a specified size and shape, as in figure 2.8. So long as the layer of metal that will form the quantum dot is thinner than the resist, the quantum dot will not be connected to the rest of the layer, and when the underlying resist is dissolved away, only the quantum dot remains [105].

If it is necessary for the particular application, a more complicated series of resists and layers can result in a more elaborate geometry [106], such as a semiconductor sandwich on top of the substrate or another resist. Different types of resists can be used that dissolve in different solvents, so that a quantum dot can be produced with an inner and outer semiconductor. Then, if it is necessary, the sides of this sandwich could be coated with another exposure to the coating semiconductor. All quantum dots discussed in this thesis are assumed to be precisely controlled, not only in their energy levels, but also in the allowed transitions.

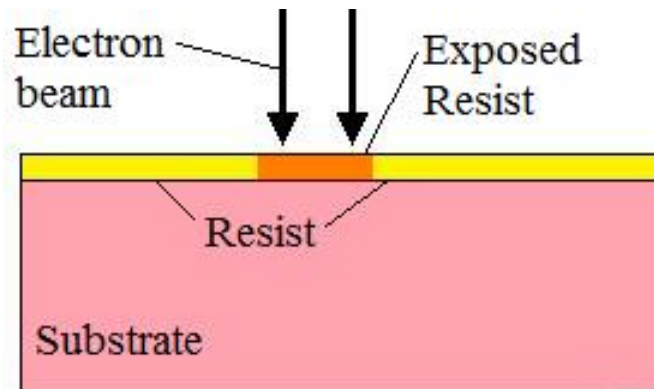


Figure 2.6: A substrate with a resist being exposed. First, the substrate is coated with a resist, and then an electron beam exposes a portion of the resist in the desired shape of the eventual quantum dot.

To dope quantum dots in something in the form of figure 2.4, it may not be sufficient to use the techniques described above. One could certainly have one more layer of a different type of resist, so that when this layer underneath everything is dissolved away it carries the quantum dot with it, and the quantum dot exists in solution. If this mechanism does not provide quantum dots with the requisite properties, or does so at too high a cost, another technique may be necessary. Many techniques have been employed, including assembly by viruses [107], but the only remaining one that will be described further here is colloidal synthesis. When certain

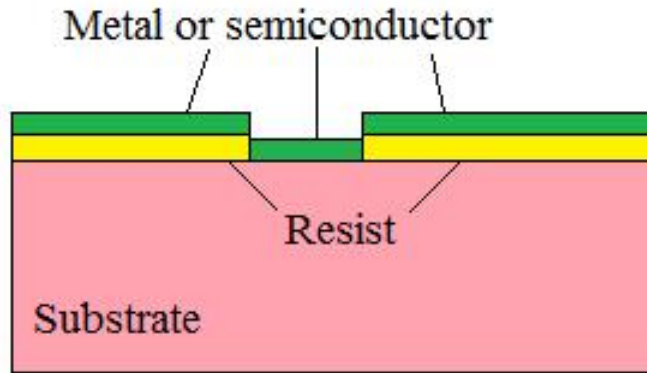


Figure 2.7: A substrate with a quantum dot laid down. The exposed portion of the resist was removed by a developer, and then a layer of the desired material for the quantum dot was laid down.

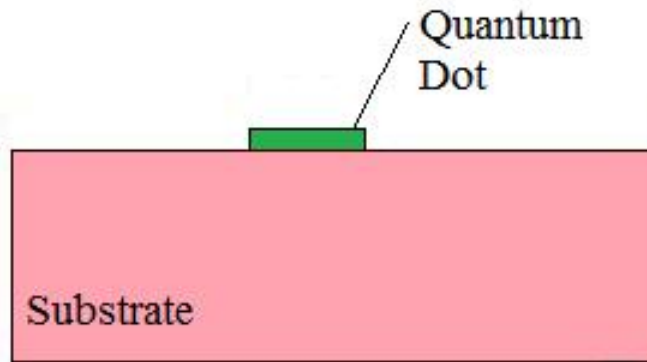


Figure 2.8: A substrate with only the quantum dot remaining. The resist was dissolved away, taking the excess material with it.

compounds are heated sufficiently in solution, they dissolve and transform into monomers. Normal crystal growth happens when there are nucleation sites and a supersaturated solution, and the strategy usually does not include nucleation sites beyond the monomers themselves. Once crystal growth has begun, the equations of state for the system will define a critical size, where crystals neither grow nor shrink. With careful timing of different chemical processes, the final solution will contain quantum dots with very similar sizes [108].

The allowed transitions for a quantum dot is another important consideration. That is, as with atoms, not every transition is allowed within a quantum dot. For dipole transitions, those that take place with only a single photon, the angular momentum quantum number must

change by exactly one. This means that for a 3-level quantum dot, which is the case for all quantum dots considered in this thesis, one level may transition to either of the others, but those other two may not transition between each other. In other words, one level is ‘special’, and those levels which are not ‘special’ can only decay or be excited to the ‘special’ level. The level transition scheme is often denoted as quantum dots which are: V-type [109], (the ground state is the special one) ladder type [110], (the middle state is the special one) or  $\Lambda$ -type [111] (the highest energy level is the special one). V-type quantum dots are investigated in chapters 4 and 7, with an example being figure 2.9. Ladder-type quantum dots are investigated in chapters 5 and 6, with an example being figure 2.10. The level structure for a  $\Lambda$ -type 3-level quantum dot is shown in figure 2.11.

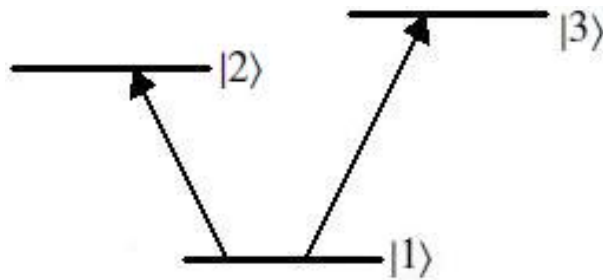


Figure 2.9: A V-type 3-level quantum dot. The only disallowed transition is the  $|2\rangle \leftrightarrow |3\rangle$  transition.

Finally, quantum dots can interact with one another in addition to interactions with external electric fields. Much of chapters 4, 5, 6, and 7 describes these interactions, so it is worthwhile to outline them here. When a quantum dot is excited by an external fields, there is a transition dipole moment associated with that excitation. This dipole moment produces an electric field which other quantum dots can interact with. They interact, since each quantum dot will be excited, having its own transition dipole moment, and dipole moments have some energy of orientation in an electric field. In this way, external laser fields enable quantum dots to interact with one another. These interactions are called dipole-dipole interactions (DDIs).

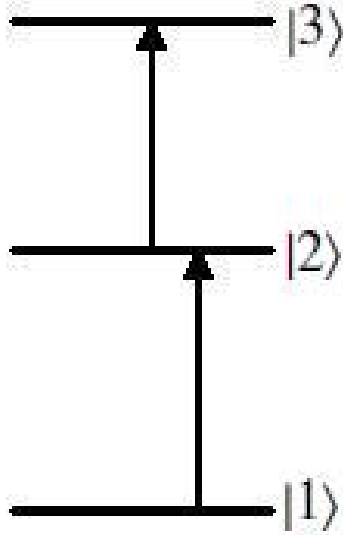


Figure 2.10: A ladder-type 3-level quantum dot. The only disallowed transition is the  $|1\rangle \leftrightarrow |3\rangle$  transition.

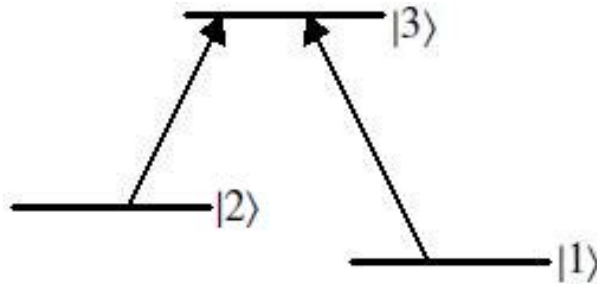


Figure 2.11: A  $\Lambda$ -type 3-level quantum dot. The only disallowed transition is the  $|1\rangle \leftrightarrow |2\rangle$  transition.

## 2.3 Metal Nanoparticles

In this section, the interactions between metallic nanoparticles and quantum dots are considered. For an ensemble of quantum dots, photonic crystals can be used to affect emission rates for these quantum dots, but there are other structures which can also have this effect. In chapters 6 and 7, a metal nanoparticle is paired with a quantum dot, which impacts the effective electric field that the quantum dot feels, since it is polarized by the laser, and produces a dipole electric field which is felt by the quantum dot. Metal nanoparticles can therefore be an important part in photonic circuit elements.



The effect of a metal nanoparticle on a quantum dot can proceed in this way: A typical size for metallic nanoparticles could be up to 600 nm, certainly enough that electrons are effectively free within them. However, for the purposes of this thesis, 1 - 20 nm is more appropriate [112], [113]. This is small enough that collective oscillations of electrons, known as plasmons, are dominant at the surface, not the interior. These surface plasmons are excited by the electric field at the metallic nanoparticle's location. For those systems under consideration, the energy of these localized surface plasmons is similar to that of an exciton transition in the nearby quantum dot, so in this way, they can interact. Therefore, energy may be transferred between an external field and the metal nanoparticle, or between a quantum dot and that metal nanoparticle.

Energy may also be transferred to the metal nanoparticle when it is polarized by the quantum dot's dipole field. That is, dipole-dipole interactions may be considered, as they were for quantum dots alone. This means that the decay rate of the quantum dot from an excited state has been affected. Finally, the polarization of the metal nanoparticle by the dipole field of the quantum dot may be felt in turn by the quantum dot. When modelling these interactions, a metal nanoparticle may be treated as another quantum dot, in that it will be excited at a specific resonance energy, but there are a few differences. For one, at the energies considered here, the excitations are localized surface plasmons, so that the fields they produce are not screened by the interior of the nanostructure in question. Another difference is the fact that the dielectric function of a metal is generally more complicated than that for a semiconductor, not to mention complex. An imaginary part to the dielectric function introduces another source of energy loss in the system. These effects will be examined further in chapters 6 and 7.

# Chapter 3

## The theory of cylindrical photonic wires<sup>1</sup>

In the previous chapter some background material was given. In this chapter, photonic nanowires, also known as nanofibers, are investigated, and energy levels and the density of states are calculated.

### 3.1 Introduction

There has been much interest in finding materials for use in the production of smaller and faster optoelectronic devices. One such group studied here is the nanophotonic wires made from photonic crystals [15], [18]. It is worth pointing out that nanophotonics is an emerging research area, and has applications in signal processing, information technology, cryptography, and in sensing and imaging applications. Even photonic crystals themselves are barely twenty years old as structures with a multidimensional band gap.

By definition, photonic crystals have an energy gap in their photonic energy spectrum. That is, some wavelengths of light will be reflected, in a band, but most wavelengths will pass

---

<sup>1</sup>Material in this chapter has been published: M. R. Singh and D. Schindel, Solid State Communications, vol. 151, p. 582, (2011).

through. There has been considerable interest in photonic crystals recently, because they can be used to control the properties of light in the same way semiconducting materials can control the propagation of electrons [7], [8], [10], [11], [12], [13].

When a photonic crystal is used as a cladding in something like a fiber optic cable application, it is referred to as a photonic wire. If it is small enough, the term photonic nanowire may be used. Work on photonic nanowires as a class of structures shows great potential as they have intriguing optical properties, and can be used to create a broad range of new types of optical devices [13], [14], [33], [36]. Several of these were discussed in chapter 2; in this chapter, we focus on the energy structure for photons in nanowires themselves. We hope that by studying these systems we can enhance our knowledge of nanoscale science and optoelectronic technology.

The aim of this chapter is to calculate the energies and the density of states for the various photonic bound states within a photonic nanowire, using nominal parameters for existing materials. The transfer matrix method was used to find bound state energies, and the density of states is used in numerical simulations. It is found that the density of states has singularities near the bound states. It is also found that the number of bound states depends on the cross-sectional area of the nanowire.

Nanowires can be made by embedding a three dimensional (3D) photonic crystal into another photonic crystal. A schematic diagram of the nanofiber is shown in figure 3.1. Another view of a fiber was shown in figure 2.4, as with the band structures that will be discussed. Due to this band structure engineering, the photons are confined within the embedded crystal. Hence, this structure acts as a nanowire. The central crystal in a photonic wire is referred to as the ‘core’, and the photonic crystal that surrounds it will be referred to as the ‘jacket’. Note that the jacket photonic crystal is infinitely large. We have modeled the core photonic crystal with either a square or circular cross-section. We have also investigated photonic wires made by embedding a dielectric material such as silica into a photonic crystal. A dielectric core was examined with either a square or circular cross-section.

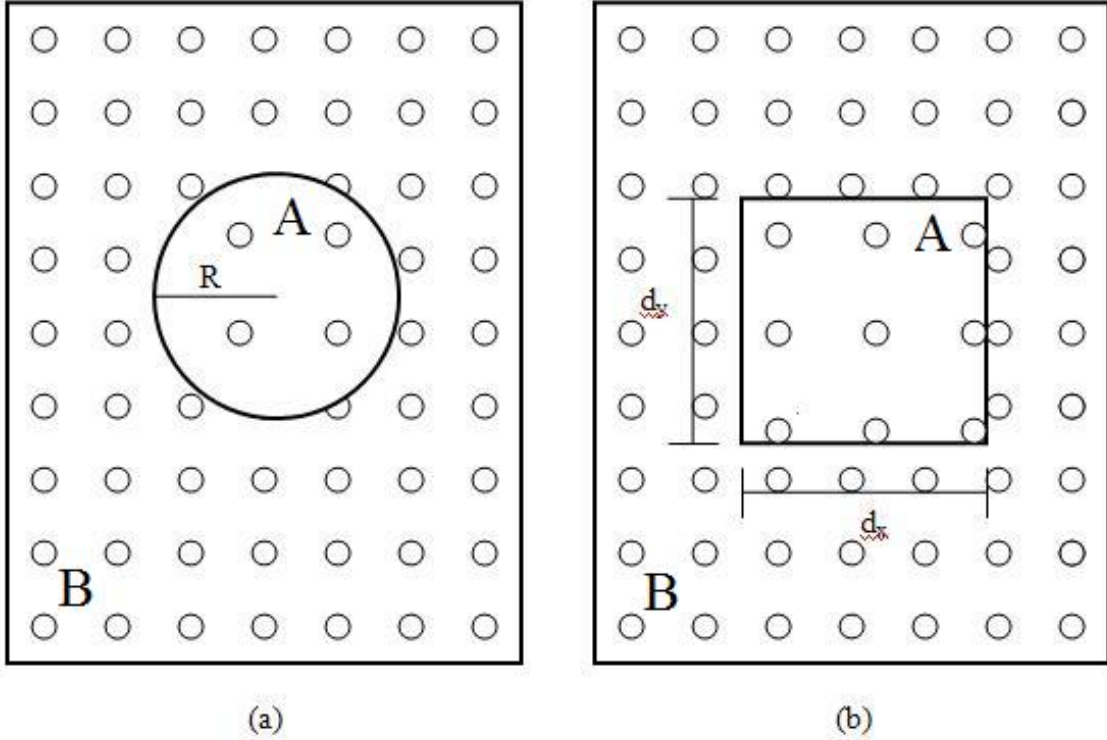


Figure 3.1: Here we see a cross-section of two photonic crystals with different photonic crystal wires running through them. On the left, we have a circular cross-section, and on the right it is square. Each photonic crystal in this example uses the same materials, the only difference being the lattice constant. The lattice constant though, is enough to make the difference between photonic crystal A and photonic crystal B.

### 3.2 Photonic Crystal Wires

In this section we study a photonic crystal wire made from two 3D photonic crystals,  $A$  and  $B$ , where  $A$  is embedded in  $B$ . The wire lies along the  $z$ -direction, and its length is taken as  $d_z$ . Both crystals  $A$  and  $B$  are fabricated from dielectric spheres which are arranged periodically in a background material. These types of crystals have been widely fabricated by many research groups [114], [115]. For example, Wijnhoven used air spheres in a titania background [100]. The refractive indices of a sphere and the background material in crystal  $A$  are taken as  $n_A^s$  and  $n_A^b$ , respectively. Likewise, for crystal  $B$  we have  $n_B^s$  and  $n_B^b$ . Diameters of the spheres in crystals  $A$  and  $B$  are denoted by  $2r_A$  and  $2r_B$ , respectively.

We consider a system where the band gap of crystal  $A$  lies within the band gap of the  $B$

crystal. Therefore, in this geometry, photons with energies lying within the band gap of the  $B$  crystal, but outside the band gap of the  $A$  crystal are confined within the wire.

To calculate the Bloch wave vectors for photonic crystals we have used the dispersion relation derived for a three-dimensional photonic crystal by John's group [116]. This model has been widely used to calculate optical properties of three-dimensional photonic crystals. According to this model, the components of Bloch wave vectors in photonic crystals  $A$  and  $B$  are written as:

$$k_A = \sqrt{f_A^2(\varepsilon_k) - k_z^2} \quad (3.1a)$$

$$k_B = \sqrt{k_z^2 - f_B^2(\varepsilon_k)} \quad (3.1b)$$

where  $k_z$  is the component of the Bloch wave vector along the  $z$ -direction. The function  $f_j(\varepsilon_k)$  is written as:

$$f_j(\varepsilon_k) = \frac{1}{L_j} \arccos(M_j - F_j) \quad (3.2a)$$

$$M_j = \frac{(n_j^s + n_j^b)^2}{4n_j^s n_j^b} \cos \left[ \frac{2\varepsilon_k (n_j^s r_j + n_j^b b_j)}{\hbar c} \right] \quad (3.2b)$$

$$F_j = \frac{(n_j^s - n_j^b)^2}{4n_j^s n_j^b} \cos \left[ \frac{2\varepsilon_k (n_j^s r_j - n_j^b b_j)}{\hbar c} \right] \quad (3.2c)$$

where  $j = A, B$ ,  $2b_a = L_A - 2r_a$ , and  $2b_b = L_B - 2r_b$ . Here,  $L_A$  and  $L_B$  are the lattice constants for crystals  $A$  and  $B$ , respectively.

With the help of equation (3.1),  $k_B$  can be expressed in terms of  $k_A$ :

$$k_B = \sqrt{f_A^2(\varepsilon_k) - f_B^2(\varepsilon_k) - k_A^2} \quad (3.3)$$

### 3.2.1 Cylindrical Wire

First we consider a photonic wire which has a cylindrical shape (see figure 3.1a). The cross section of the wire  $A$  is circular, and its diameter is taken as  $d$ . The cylindrical coordinates for the wire are taken as  $(r, \theta, z)$ . Using boundary conditions at  $r = d/2$  and a particular angle  $\theta$  for the Bloch waves at the interfaces between crystal  $A$  and  $B$ , the following dispersion relations for bound photons have been obtained as [117]:

$$D_m - \left(\frac{f_B}{f_A}\right)^2 N_m = m^2 G_m \quad (3.4a)$$

where:

$$D_m = \frac{J_{m-1}(k_A d/2) - J_{m+1}(k_A d/2)}{(k_A d/2) J(k_A d/2)} \quad (3.4b)$$

$$N_m = \frac{K_{m-1}(k_B d/2) + K_{m+1}(k_B d/2)}{(k_B d/2) K_m(k_B d/2)} \quad (3.4c)$$

and functions  $J_m(x)$  and  $K_m(x)$  are the  $m^{\text{th}}$  order Bessel function and the  $m^{\text{th}}$  order modified Bessel function of the second kind, respectively. Also,  $k_A$  and  $k_B$  are the components of Bloch wave vectors perpendicular to the  $z$  direction, and along the radius of the circular wire. For what follows,

$$J_m = J_m(k_A d/2) \quad (3.5a)$$

$$K_m = K_m(k_B d/2) \quad (3.5b)$$

and now we can define:

$$G_m = \frac{S P J_m K_m}{Q_m} \quad (3.6a)$$

where:

$$S = \left[ (k_A R)^{-1} (k_B d/2)^{-3} + (k_A d/2)^{-3} (k_B d/2)^{-1} \right] \quad (3.6b)$$

$$P = \left[ \left(\frac{f_B}{f_A}\right)^2 (k_A d/2)^2 + (k_B d/2)^2 \right] \quad (3.6c)$$

$$Q_m = (k_B d/2) K_m [(J_{m-1} - J_{m+1})] - (k_A R) J_m [K_{m-1} + K_{m+1}] \quad (3.6d)$$

Also,  $m$  is the quantum number related to the angular coordinate  $\theta$ , and it has values  $m = 0, 1, 2$ , and so on. The above equation is valid both for transverse electric (TE) and transverse magnetic (TM) modes.

Therefore, by putting the value of  $k_B$  from equation (3.3) into equation (3.4), we can evaluate numerically the quantized values of  $k_A$  for a given value of quantum number  $m$ . We denote the quantized values of  $k_A$  as  $k_{mn}$ . Here, the quantum number  $n$  is due to the radial boundary condition. It has values  $n = 1, 2, 3$ , and so on. Therefore, in circular wires we have two quantum numbers,  $m$  and  $n$ . The energies of bound photons in the wire are denoted as  $\varepsilon_k = \varepsilon_{mnk_z}$ , and they can be obtained from equation (3.1). They are:

$$f_A(\varepsilon_{mnk_z}) = \sqrt{k_{mn}^2 + k_z^2} \quad (3.7)$$

where  $\varepsilon_{nm}$  is the energy of a bound state when  $k_z = 0$ .

For both TE and TM cases it has been shown [117] that  $m = 0$ . Bound photon energies are calculated from equation (3.4) by putting  $m = 0$ . This gives:

$$\frac{J_1(k_A d/2)}{J_0(k_A d/2)} = \left(\frac{f_B}{f_A}\right)^2 \left( \frac{k_A}{\sqrt{f_A^2 - f_B^2 - k_A^2}} \right) \frac{K_1(k_B d/2)}{K_0(k_B d/2)} \quad (3.8)$$

where quantized energies are denoted as  $\varepsilon_{0nk_z}$ .

### 3.2.2 Rectangular Wire

Let us consider a rectangular wire. The width and height of the wire are assigned  $d_x$  and  $d_y$ , respectively. (see figure 3.1b) For convenience, we set the origin in the middle of the wire, so that the boundaries occur at  $x = \pm d_x/2$  and  $y = \pm d_y/2$ . Photons propagate along

the z-direction in the wire and exponentially decay in crystal *B*. Using boundary conditions for the Bloch waves at the interfaces of crystals *A* and *B*, the following dispersion relations for photons confined in the wire have been obtained [18]:

$$k_x \tan(k_x d_x - m \frac{\pi}{2}) = \frac{f_A^2(\epsilon_k)}{f_B^2(\epsilon_k)} \sqrt{f_A^2(\epsilon_k) - f_B^2(\epsilon_k) - k_x^2} \quad (3.9)$$

$$k_y \tan(k_y d_y - n \frac{\pi}{2}) = \frac{f_A^2(\epsilon_k)}{f_B^2(\epsilon_k)} \sqrt{f_A^2(\epsilon_k) - f_B^2(\epsilon_k) - k_y^2} \quad (3.10)$$

where  $m = 0, 1, 2, \dots$  and  $n = 0, 1, 2, \dots$ . Here,  $k_x$  and  $k_y$  are x and y components, respectively, of the Bloch wave vector  $\mathbf{k}_A$ .

The wave vectors  $k_x$  and  $k_y$  in equations (3.9 and 3.10) are quantized and have quantization number  $m$  and  $n$ , respectively. Let us rename  $k_x$  and  $k_y$  to be  $k_m$  and  $k_n$ , respectively. The quantized energy is found from equation (3.7), where  $k_{mn}^2 = k_n^2 + k_m^2$ .

Now we calculate the density of states (DOS) for these nanowires. As we know, the DOS plays a very important role in calculations of the refractive index, absorption coefficient, and photo-luminescence studies. The DOS was discussed briefly in chapter 2, section 2.1.1. The expression for the DOS for square and circular nanowires is calculated in reference [14], and it is written as:

$$\rho(\epsilon) = \frac{d_z}{\pi} \sum_{m,p} \frac{f_A(\epsilon) \zeta(\epsilon)}{\sqrt{f_A^2(\epsilon) - f_A^2(\epsilon_{mn})}} \Theta(\epsilon - \epsilon_{mn}) \quad (3.11a)$$

where:

$$\zeta(\epsilon_{mpk_z}) = \frac{1}{L_a} \frac{\eta_+(\epsilon_{mnk_z}) - \eta_-(\epsilon_{mnk_z})}{\sqrt{1 - \cos^2[f_A(\epsilon_{mnk_z})L_a]}} \quad (3.11b)$$

$$\eta_{\pm}(\epsilon_{mpk_z}) = \frac{(n_a^s \pm 1)^2 (n_a^s r_a \pm b_a)}{2n_a^s \hbar c} \kappa_{\pm}(\epsilon_{mpk_z}) \quad (3.11c)$$

$$\kappa_{\pm}(\epsilon_{mpk_z}) = \sin\left(\frac{2\epsilon_{mnk_z} n_a^s r_a}{\hbar c} \pm \frac{2\epsilon_{mnk_z} b_a}{\hbar c}\right) \quad (3.11d)$$

Here we comment on the validity and limitations of our theoretical equations (3.1-3.11).



These equations are derived for photonic crystal and dielectric wires under the assumption that the interface between the embedded material (core) and the host material (jacket) is smooth and does not have any roughness or defects. For photonic crystal wires (i.e. (3.8-3.10)) we have assumed that the core photonic crystal must have a perfect band gap. It means that there is no leakage of photons from the core to the jacket. In other words, the core should be a perfect reflector when the energy of photons lies within the band gap of the core photonic crystal. It is experimentally found that if there are less than 10 unit cells, the photonic crystal is not a perfect reflector and there is a leakage of photons [118]. In our formulation we have used the band structure for 3D photonic crystals from reference [89]. This band structure was obtained for photonic crystals containing an infinite number of lattice cells. Therefore, when the core has less than about 10 lattice cells, the theoretical equations derived for photonic crystals are not valid.

### 3.2.3 Dielectric Wires

Now we study the dielectric wires which are fabricated by embedding a dielectric material  $A$  (the core) into photonic crystal  $B$  (the jacket). In the literature, we can see that these types of wires have been fabricated widely [13]. Let the refractive index of the dielectric material be  $n_d$ . The equations derived for bound photon states for the rectangular (equations (3.9 and 3.10)) and circular wires (equations (3.4 and 3.8)) in the previous subsections are valid for these types of wires, except for the following equation. The function  $f_A$  for both wires (circular or square cross section) should be replaced by the following function:

$$f_A(\epsilon_k) = \left( \frac{\epsilon_k}{\hbar c} \right) n_d \quad (3.12)$$

Finally, we calculate bound states and DOS of nanowires whose core is made from a dielectric material. The expression for the DOS for a square nanowire is calculated in reference

[116], and is written as:

$$\rho(\varepsilon_{nmk_z}) = \frac{d_z}{\pi} \sum_{m,p} \left( \frac{n_d d_z}{\pi \hbar c} \right) \frac{\varepsilon}{\sqrt{\varepsilon_{nmk_z}^2 - \varepsilon_{nm}^2}} \Theta(\varepsilon_{nmk_z} - \varepsilon_{nm}) \quad (3.13)$$

### 3.3 Results and Discussion

We modeled 3D photonic crystal *A* (core) as GaAs spheres with the background material, air. The refractive indices for GaAs and air are taken as  $n_A^s = 3.32$  and  $n_A^b = 1$ , respectively. The diameter of GaAs spheres is  $a_A = 175$  nm, and the lattice constant for this photonic crystal is  $L_A = 700$  nm. Using the band structure model of reference [89], we have calculated the band structure of this crystal and found that the upper and lower band edge of the band gap lies at  $\varepsilon_A^u = 0.381$  eV and  $\varepsilon_A^l = 0.179$  eV, respectively. Hence the band gap of this crystal is  $\varepsilon_A^{gap} = \varepsilon_A^u - \varepsilon_A^l = 0.202$  eV.

On the other hand, we have considered a 3D photonic crystal *B*, (jacket) made from AlAs spheres and air. The refractive index for AlAs is taken as  $n_B^s = 2.87$ . The diameter of AlAs spheres is  $a_B = 175$  nm, and the lattice constant for the photonic crystal *B* is  $L_B = 700$  nm. For this crystal, the upper and lower band edges lie at  $\varepsilon_B^u = 0.399$  eV and  $\varepsilon_B^l = 0.205$  eV, respectively, and  $\varepsilon_B^{gap} = \varepsilon_B^u - \varepsilon_B^l = 0.194$  eV. Note that the upper edge of the band gap in the core crystal is lower than that of the jacket crystal. Therefore, it satisfies the band gap engineering requirements. The difference between the upper band edges of the core and jacket energies is calculated as  $\Delta\varepsilon_c = \varepsilon_B^u - \varepsilon_A^u = 0.018$  eV. We call this the well depth of the nanowire. In other words, when a photon propagates within the core crystal and its energy lies within  $\Delta\varepsilon_c$ , this photon will be confined within the core. For example, photons with wavelengths from 3111 nm to 3256 nm could be trapped within the core crystal. All simulations were performed using the software package, Maple.

We have calculated bound states for a trapped photon within a nanowire which has a square shape. The size of the wire is  $d_x = d_y = 7000$  nm. Using equations (8) and (9), we have found four bound states located at  $\varepsilon_{00} = 0.385$  eV,  $\varepsilon_{10} = \varepsilon_{01} = 0.391$  eV,  $\varepsilon_{11} = 0.396$  eV, and  $\varepsilon_{20} = \varepsilon_{02} = 0.398$  eV. Note that energies for quantum numbers  $n = 1, m = 0$  and  $n = 0, m = 1$  are degenerate. When we decrease the size of the square wire, such as  $d_x = d_y = 2800$  nm, we get only one bound state, the ground state of the wire, and it lies at  $\varepsilon_{00} = 0.395$  eV. If we reduce the size of the wire further there will be no bound states in the wire. This means that by changing the size of the wire, the number of bound states will be controlled.

A wire with a circular shape, with diameter  $d = 7900$  nm was also considered. Using equation (3.8), and thereby limiting ourselves to TE modes, we have found only one bound state located at  $\varepsilon_{10} = 0.391$  eV. In this case we do not have degenerate states as we had in a square nanowire. Note that the number of bound states is less than that of the square nanowire, while the diameter of the circular nanowire has almost the same magnitude as the square nanowire. This is because we have not calculated the hybrid modes for the circular wire. We have only calculated the TE modes here.

The DOS is plotted in figure 3.2 for the square nanowire. The figure contains four peaks which correspond to four bound states. Note that the DOS has very large values near the bound photon energies. The second state appears broader than the other three because it is degenerate and has a contribution from two states. The fourth state is also degenerate, and would appear broader, but the jacket photonic crystal band gap extends less than 1 meV above that state, so the broadening is not shown. That is, photons with higher energy would not be confined in the wire, so the region where this state would appear broadened is cut off.

The density of states for a photonic wire with a circular cross section, considering only the TE modes, is plotted in figure 3.3. There is only a single state within the band gap of the jacket photonic crystal. We point out that uses for photonic wires (for example, by doping them with quantum dots and using the wire as a switching mechanism) are often easier to control if there is only one bound state in the photonic wire [18].

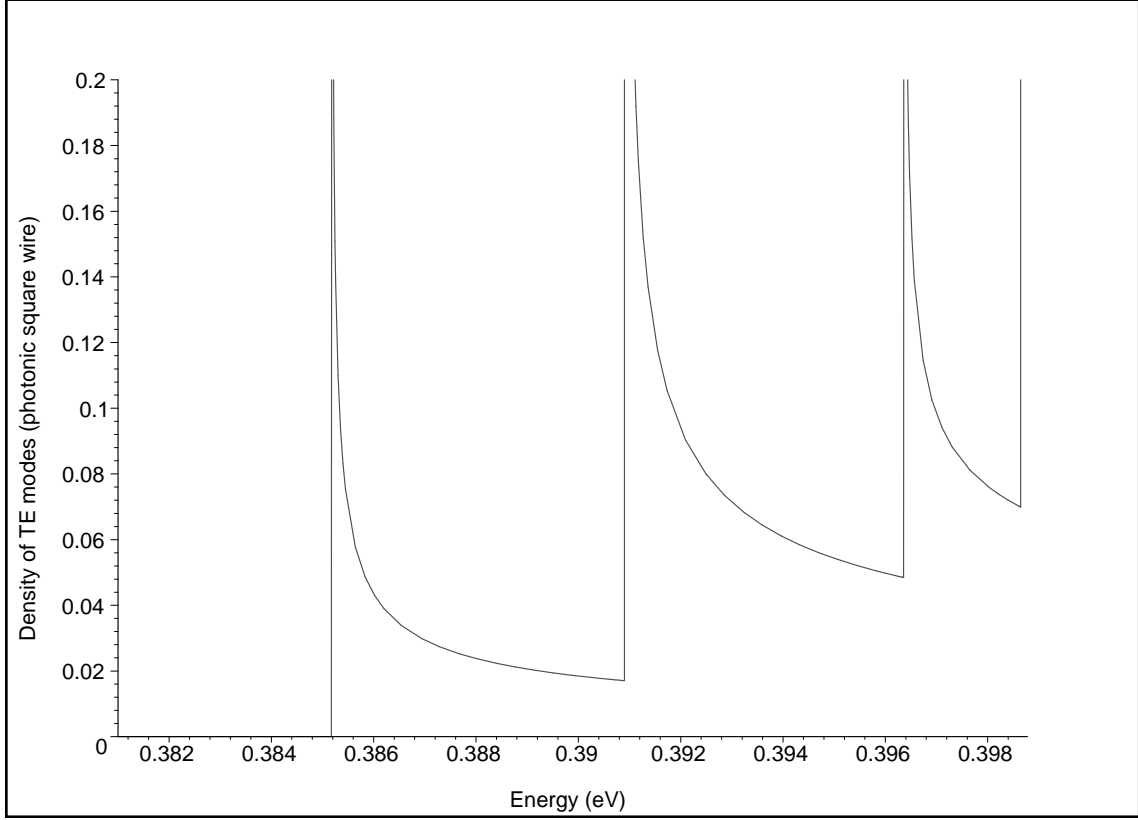


Figure 3.2: Density of States for our Photonic Nanowire, with a square cross-section. Note that the well is nominally between 0.381 and 0.399 eV, and the second and fourth states shown here have degeneracies.

If the spheres in photonic crystal A (core) are made up of  $\text{Al}_x\text{Ga}_{1-x}\text{As}$ , then the well depth of the wire will be smaller than this one,  $\Delta\varepsilon_c = 0.018 \text{ eV}$ . This is because the index of refraction of  $\text{Al}_x\text{Ga}_{1-x}\text{As}$  lies between AlAs and GaAs. For example, we consider spheres made from  $\text{Al}_{0.5}\text{Ga}_{0.5}\text{As}$  with refractive index  $n_A^s = 3.01$ . For the nanowire with  $d_x = d_y = 7000 \text{ nm}$  we found one bound state located at  $\varepsilon_{00} = 0.397 \text{ eV}$ . This means that the number of bound states within the wire can be controlled by adjusting the proportions of  $\text{Al}_x\text{Ga}_{1-x}\text{As}$ .

We have calculated the bound states of the square nanowire when the core is made from dielectric materials such as air and silica. To get the bound states within the band gap of the jacket photonic crystal, we have to adjust the width  $d_x$  of the wire. For example, we found one bound state within the band gap of the jacket crystal for air and silica cores when  $d = 1200 \text{ nm}$  and  $d = 800 \text{ nm}$ , respectively. As we increase the size of the nanowire from  $d = 800 \text{ nm}$

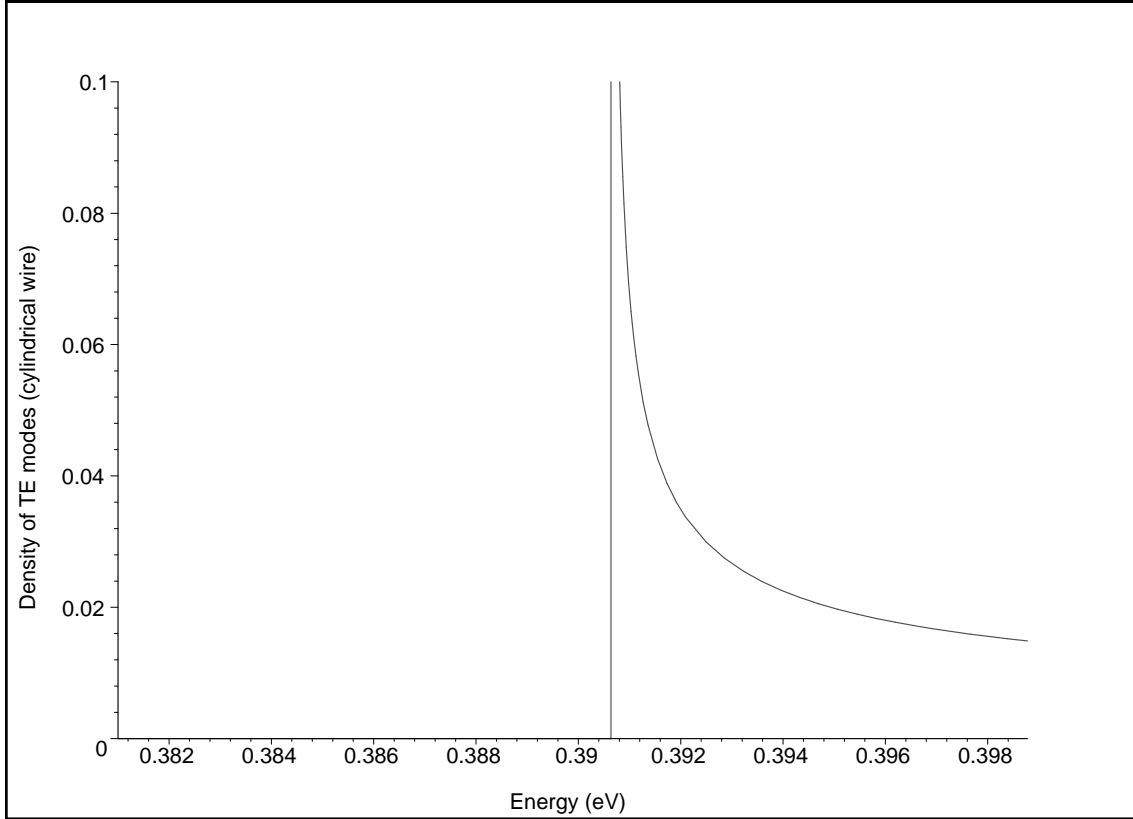


Figure 3.3: Density of States for our Photonic Nanowire, with a circular cross-section. Note that there is only a single TE mode. Any other photonic states in this wire would either be a TM or a hybrid mode.

to  $d = 1600$  nm, the number of bound states increases from one to two. Similarly, we have also calculated the bound states for air and silica circular nanowires. We found one bound state when the diameter of the air and silica nanowire were  $d = 6300$  nm and  $d = 4300$  nm, respectively.

In figure 3.4, we have plotted bound energy levels for a square nanowire with a dielectric core as a function of width  $d_x$  and the index of refraction  $n_d$  of the dielectric. The energy of the allowed state drops with increasing width and increasing index of refraction. Note that this is for a square cross-section, and in this region, a state exists. This may be due to an overestimate of the size of the band gap in this system, and in [89], we may only see the low energy region of this plot. However, we may still conclude that there will be a single state in the wire for many possible widths and dielectric constants of the core of this wire.

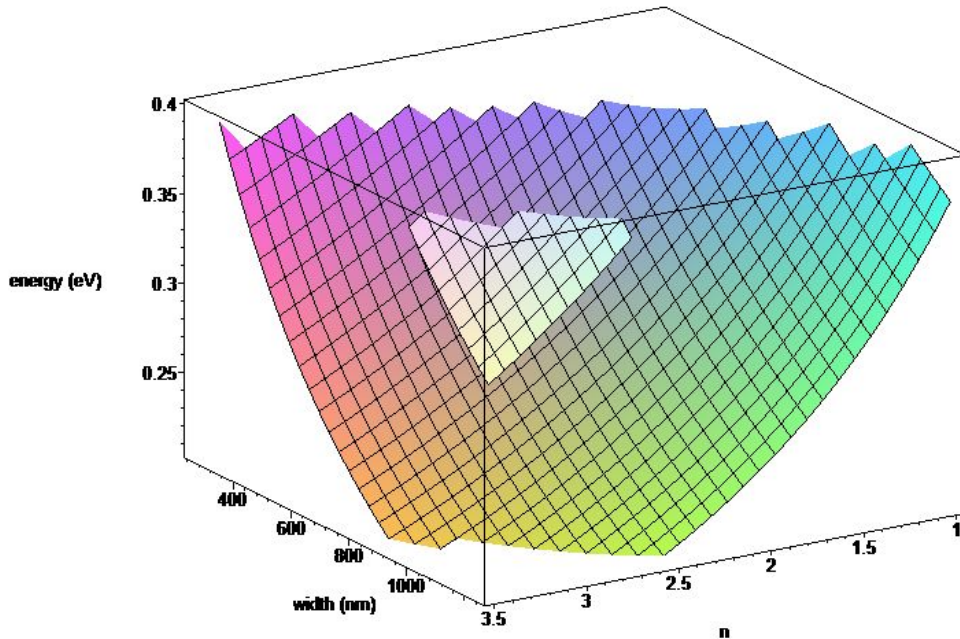


Figure 3.4: Allowed photon modes in a photonic nanowire with a square cross-section and a dielectric core.

Finally, when the dielectric core has a circular cross-section, a larger wire seems to be necessary. The calculated modes for such a wire are shown in figure 3.5. Since we restricted ourselves to TE modes, the wires needed to be somewhat thicker in order to contain bound photon states. It is worth noting that for the narrow strip of states at  $n = 3.5$  and  $d = 655$  nm, for example, there are two allowed modes everywhere in that region. Even though the circular cross-section geometry needs a larger wire to propagate TE modes, it is worth mentioning that this is still much narrower than a wire with a photonic crystal core, which cannot be made much thinner than 7000 nm [118].

Our theory is suitable for all types of photonic crystal structures. The only requirement for our theory is that both core and jacket photonic crystals must have band gaps, and the energy at the upper edge of the band gap of the core must be lower than that of the jacket. The model band structure used in this chapter produces a band gap and also gives correct physics for a

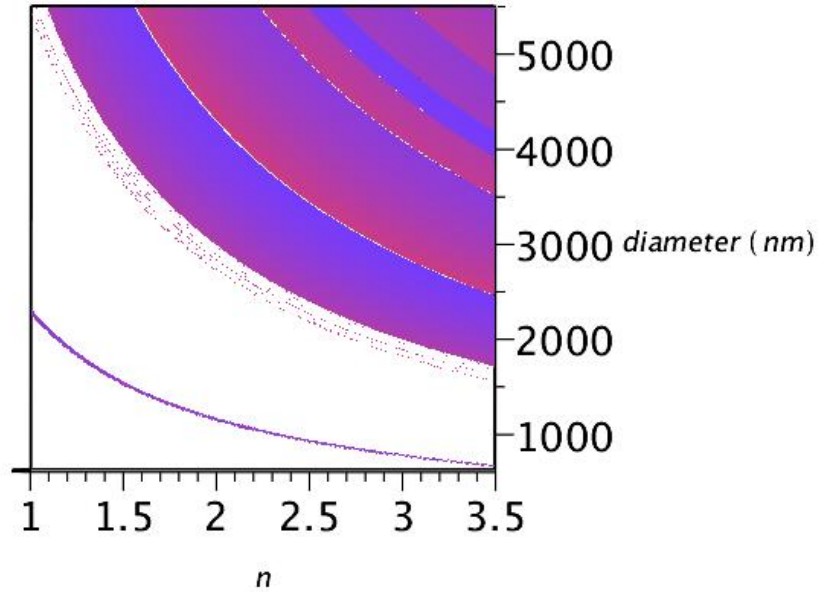


Figure 3.5: Allowed photon modes in a photonic nanowire with a circular cross-section and a dielectric core.

photonic crystal [12]. It does not have information about the crystal structure containing the specific unit cell. This model is similar to the effective mass approximation band structure model used in semiconductors. The effective mass approximation gives the correct physics but does not have information about the unit cell of the crystal structure.

### 3.4 Conclusion

The allowed photon modes for a photonic nanowire have been studied for several different setups. The photonic crystals were modeled using the transfer matrix method, [18], adopting parameters from an existing three dimensional photonic crystal [89]. When two different photonic crystals were used to produce the nanowire, several photon modes were found. The num-

ber of modes can be reduced as much as desired by adjusting the proportions of  $\text{Al}_x\text{Ga}_{1-x}\text{As}$  used to produce either photonic crystal. Square and circular cross-sections were considered for the wire, which shifted the energy levels of the photon modes. It was also found that when we have a photonic crystal in the core of our wire, it was easier to produce a wire with only a single allowed photon mode if we have a circular cross-section and restrict ourselves to TE modes. Having a photonic nanowire with a core that is a dielectric material was considered, and it was found that more options arise for producing nanowires with only a single mode. The wire can be made much smaller, and many different materials could be used to produce a nanowire with only a single photon mode. In modeling the circular cross-section wire with a dielectric core, the wire needed to be thicker, though not as thick as was the case with a photonic crystal core. These results, while only meant to be qualitative, can be useful to those producing new photonic devices. Photonic wires can be doped with quantum dots to better control the emission and absorption properties of the quantum dots.



# Chapter 4

## Photon absorption in interacting quantum dots doped in nanofibers<sup>1</sup>

In the previous chapter, various forms of photonic wires were discussed, and the density of photonic states was calculated. In this chapter, the optoelectronic properties of photonic nanofibers doped with quantum dots are calculated.

### 4.1 Introduction

There has been considerable interest in studying quantum optics of photonic fibers which are made from photonic crystals [14], [15]. They will play an important role in quantum computation, optical switching, and optical detection [14], [15], [32], [33], [34], [37]. In this chapter we study the coupling between quantum dots through the dipole-dipole interaction (DDI) on nanofibers doped with an ensemble of quantum dots. Photonic and polaritonic crystals are materials which have an energy gap in their photonic spectrum [11], [16], [17]. Many inter-

---

<sup>1</sup>Portions of this chapter have been published: M. R. Singh and D. Schindel, Journal of the Optical Society of America B, vol. 27, p. 2759, (2010).

esting phenomena are predicted due to the existence of such energy gaps [11], [16], [17]. The quality factor,  $Q$ , has been measured and calculated for many different fibers and wave guides made from photonic crystals. The  $Q$  factor is calculated from the transmission or absorption spectra of bound photon states. Values of the  $Q$  factor have been observed as high as 40 000 in some systems, and even as high as 600 000 [15], [16] in certain optical cavities made from photonic crystals.

The effect of the DDI in the local field approximation has been investigated in multi-level atomic systems [38], [39], [40], and also in nanostructures [41]. The inclusion of the DDI has led to many fascinating effects in atomic gases. For example, the ultrafast optical switching and the enhancement of inversionless gain and index of refraction have been predicted in gases. The DDI has also been investigated in quantum entanglement [42], quantum jumps [43], and resonance fluorescence [44], in two coupled atoms.

Some work has also been done to investigate the effect of DDI in photonic crystals [45], [46], [47]. For example, both self-induced transparency and spontaneous emission in the presence of this interaction have been studied in photonic crystals doped with two-level atoms [45]. We have also investigated the effect of the DDI using the mean field approximation in nanoparticles [46], [47], [48], [49], [50]. Additionally, electromagnetically induced transparency (EIT) and spontaneous emission cancellation have been calculated for photonic crystals doped with multi-level nanoparticles [46], [47], [48]. The inhibition of two-photon absorption due to a selected electronic transition has also been investigated [49], [50].

We have considered a photonic nanofiber which is fabricated by embedding a dielectric material such as silica into a photonic crystal. A schematic diagram of a nanofiber is shown in figure 4.1. The embedded dielectric material has been doped with an ensemble of three-level quantum dots. Without the quantum dots, this was one of the four geometries studied in chapter 3. Recently, quantum dots have been doped in photonic crystals by several groups, and the typical size of a doped quantum dot varies between 5 nm and 14 nm [119]. Quantum dots have been used as multi-level atoms to study interference and coherence phenomena

[120], [121]. The size and configuration of the quantum dot does not matter in the present calculation, as any quantum dot that has been produced is too small for the size to come into play here. Any quantum dot which has three levels is suitable for the present work.

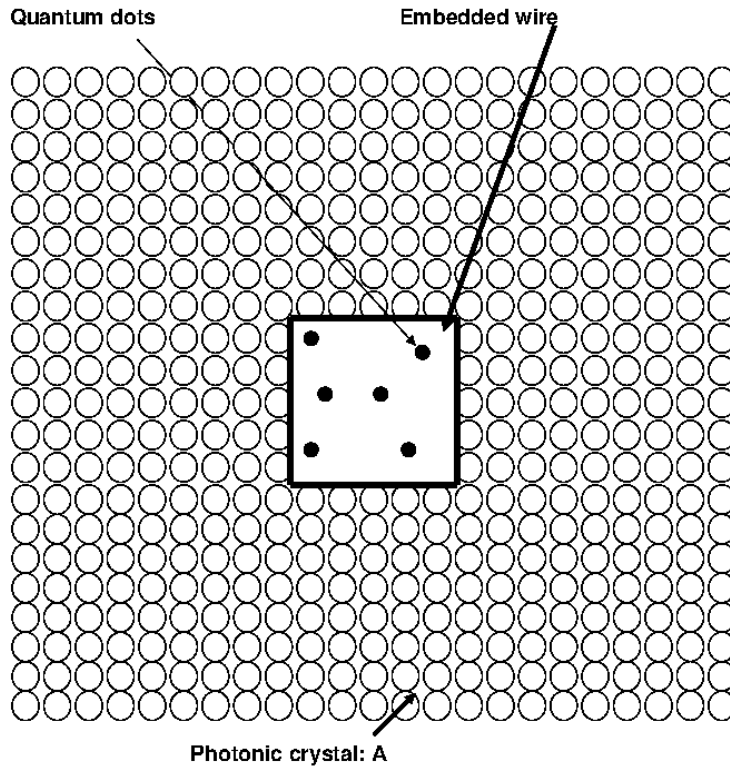


Figure 4.1: Schematic diagram is shown for a photonic nanofiber (top view). The nanofiber is made from embedding a dielectric material into a photonic crystal A. Quantum dots are doped into the embedded material.

A probe field is applied to monitor the absorption process in quantum dots, and a control field is then applied to manipulate said absorption process. In figure 4.2, a schematic diagram of a three-level quantum dot is shown. As pointed out in chapter 2, this is called a V-type structure. Quantum dots contain dipole moments due to electronic transitions induced by the probe and control fields. Hence, quantum dots are interacting with one another via the DDI.

Photonic wires have bound photon energy states, which were evaluated in chapter 3. Therefore, doped quantum dots are interacting not only with each other, but also with the nanofiber

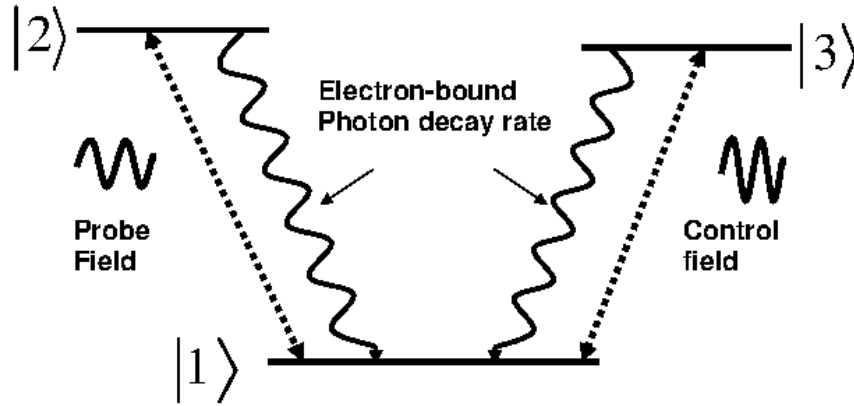


Figure 4.2: Schematic diagram of a three-level quantum dot. The levels are denoted by  $|1\rangle$ ,  $|2\rangle$ , and  $|3\rangle$ . A control laser couples  $|3\rangle$  and  $|1\rangle$  whereas a probe laser couples  $|2\rangle$  and  $|1\rangle$ . Levels  $|3\rangle$  and  $|2\rangle$  decay to level  $|1\rangle$  due to the electron-bound photon interaction.

via the electron-bound photon (EBP) interaction. The absorption coefficient has been calculated using the density matrix method, and the DDI has been included in the mean field approximation. Numerical simulations have been performed to find the absorption coefficient. It was found that the absorption peak splits into a transparent state and two absorbing peaks due to a strong DDI. The mechanism for this splitting can be explained by the physics of dressed states. It has also been predicted that the splitting of the photon absorption peak can be controlled by tuning either the resonance energies of quantum dots or the bound photon states in the nanofiber.

## 4.2 Dipole-dipole interaction in photonic nanowires

Within the last five years, photonic fibers have been fabricated by inserting a dielectric material into a photonic crystal [16]. Photonic crystals are used as a cladding material since they are a perfect reflector of light within their band gap. In this chapter, a photonic crystal is made from dielectric spheres which are arranged periodically in a background material. The background material is taken as air with a refractive index of 1.

The isotropic band structure model developed by John's group [122] has been used in this chapter. This model has been used widely in photonic crystal literature to study optical properties [12], [122], [123], [124], [125], [126]. The dispersion relation for the photonic crystal is written as [122]:

$$\varepsilon_{k_p} = \frac{\hbar c}{4n_p r} \arccos \left( \frac{4n_p \cos(k_p L) - (n_p - 1)^2}{(n_p + 1)^2} \right) \quad (4.1)$$

where  $n_p$  is the refractive index of spheres. Parameters  $L$  and  $r$  are the lattice constant and radius of the dielectric spheres, respectively. Finally,  $k_p$  is the wave vector for photons in the crystal, and  $c$  is the vacuum speed of light.

The dispersion relation for the embedded dielectric nanofiber is taken as:

$$\varepsilon_{k_d} = \frac{\hbar c}{n_d} k_d \quad (4.2)$$

where  $n_d$  is the refractive index of the embedded material and  $k_d$  is the wave vector for photons in the dielectric material.

We have taken the nanofiber as having a square cross-section, because analytical expressions for the quantized energies and the density of states (DOS) are easily obtained in that case. However, the end results of the present work do not depend on the shape of the nanofiber. The width and height of the nanofiber are denoted as  $d_x$  and  $d_y$ , respectively. The nanofiber lies along the z-direction, and is assigned the length  $d_z$ . The value of  $d_z$  is taken to be very large (i.e.  $d_z \rightarrow \infty$ ). Using the transfer matrix method of references [14], [117], [127], and [128], we found the following energy states for photons in the nanofiber:

$$k_n \tan(k_n d_x / 2 - n \frac{\pi}{2}) = \sqrt{k_d^2 (\varepsilon_{nmk_z}) - k_p^2 (\varepsilon_{nmk_z}) - k_n^2} \quad (4.3)$$

$$k_m \tan(k_m d_y / 2 - m \frac{\pi}{2}) = \sqrt{k_d^2 (\varepsilon_{nmk_z}) - k_p^2 (\varepsilon_{nmk_z}) - k_m^2} \quad (4.4)$$

where functions  $k_p$  and  $k_d$  are obtained from equations (4.1) and (4.2), respectively, and are written as:

$$k_p(\varepsilon_{nmk_z}) = \frac{\arccos[G_k - G_n]}{L} \quad (4.5)$$

where:

$$G_k = \frac{(n_p + 1)^2}{4n_p} \cos\left(\frac{4\varepsilon_{nmk_z} n_p r}{\hbar c}\right) \quad (4.6)$$

$$G_n = \frac{(n_p - 1)^2}{4n_p} \quad (4.7)$$

and of course, from equation (4.2):

$$k_d(\varepsilon_{nmk_z}) = \frac{n_d}{\hbar c} \varepsilon_{nmk_z} \quad (4.8)$$

Here,  $n$  and  $m$  are the quantum numbers.  $k_n$ ,  $k_m$ , and  $k_z$  are x-, y-, and z-components of the wave vector for a photon in the nanofiber. Solving for the values of  $k_n$  and  $k_m$  self-consistently from equations (4.3)-(4.8) yields the bound state energy for given quantum numbers  $n$  and  $m$ , and is obtained from equation (4.2):

$$\varepsilon_{nmk_z} = \frac{\hbar c}{n_d} \sqrt{k_z^2 + k_n^2 + k_m^2} \quad (4.9)$$

Finally, we would like to make a comment on the isotropic model used in equation (4.1). This model is a one-dimensional representation of an face-centered cubic (fcc) array of dielectric spheres. The fcc lattice of dielectric spheres does not have a complete photonic band gap in all directions [16]. It also yields a divergence in the photonic density of states. While this does not invalidate the main findings of the present work, it is worth pointing out that this model does not describe a real 3D photonic crystal [12].

### 4.3 Density of States

We calculate the density of states (DOS) of the nanofiber. Using the concept of the DOS, the summation over  $k_z$  is replaced by the integration over energy,  $\varepsilon_{nmk_z}$ :

$$\sum_{n,m} \sum_{k_z} = \sum_{n,m} \int D(\varepsilon_{nmk_z}) d\varepsilon_{nmk_z} \quad (4.10)$$

where  $D(\varepsilon_{nmk_z})$  is called DOS and is obtained as:

$$D(\varepsilon_{nmk_z}) = \frac{d_z}{\pi} \frac{dk_z}{d\varepsilon_{nmk_z}} \quad (4.11)$$

Note that the component  $k_z$  is responsible for photon propagation along the nanofiber. The expression for  $k_z$  is obtained from equation (4.2) to be:

$$k_z = \sqrt{\left(\frac{n_d}{\hbar c} \varepsilon_{nmk_z}\right)^2 - k_n^2 - k_m^2} \quad (4.12)$$

With the help of the above expression we get the following expression of the DOS:

$$D(\varepsilon_{nmk_z}) = \left(\frac{n_d d_z}{\sqrt{2}\pi \hbar c}\right) \frac{\sqrt{\varepsilon_{nm}}}{\sqrt{\varepsilon_{nmk_z} - \varepsilon_{nm}}} \quad (4.13)$$

where:

$$\varepsilon_{nm} = \frac{\hbar c}{n_d} \sqrt{(k_n^2 + k_m^2)} \quad (4.14)$$

It is important to note that the DOS of the nanofiber has a singularity at  $\varepsilon_{nmk_z} = \varepsilon_{nm}$ . This is the same form for the density of states found in chapter 3, which we would expect, since it is precisely one of the systems considered in that chapter.

## 4.4 Dipole-Dipole Interaction

The energy levels of quantum dots are denoted as  $|1\rangle$ ,  $|2\rangle$ , and  $|3\rangle$ . Two laser fields are applied to study the DDI in the nanofiber. A tunable probe field of energy  $\varepsilon_p$  and Rabi energy  $\Omega_{12}$  is applied to monitor the absorption coefficient between states  $|1\rangle$  and  $|2\rangle$ . A control laser field of energy  $\varepsilon_c$  and Rabi frequency  $\Omega_{13}$  is applied between states  $|3\rangle$  and  $|1\rangle$ . Dipole moments  $\mu_{21}$  and  $\mu_{31}$  are induced in quantum dots due to electronic transitions  $|1\rangle \leftrightarrow |2\rangle$  and  $|1\rangle \leftrightarrow |3\rangle$ , respectively.

Quantum dots are interacting with one another via the DDI. Following the method of the mean field approximation of references [49] and [50], the DDI Hamiltonian is obtained as:

$$H_{dd} = -2\gamma_0 [C_{21}\rho_{21} + C_{23}\rho_{31}] \sigma_{21}^+ e^{-i(\varepsilon_p - \varepsilon_{21})t/\hbar} - 2\gamma_0 [C_{31}\rho_{31} + C_{23}\rho_{21}] \sigma_{31}^+ e^{-i(\varepsilon_c - \varepsilon_{31})t/\hbar} + h.c. \quad (4.15)$$

where  $\rho_{j\ell}$  is the density matrix element for the transition  $|j\rangle \leftrightarrow |\ell\rangle$ . Here, *h.c.* stands for the Hermitian conjugate, and  $\gamma_0$  represents the linewidth for an electron in the quantum dot in a vacuum. The parameters  $C_{21}$ ,  $C_{31}$ , and  $C_{23}$  are called the dipole-dipole coupling constants and they measure the strength of the DDI. They are obtained as:

$$C_{21} = \left( \frac{N_0}{3\varepsilon_0\gamma_0} \right) \mu_{21}^2 \quad (4.16)$$

$$C_{31} = \left( \frac{N_0}{3\varepsilon_0\gamma_0} \right) \mu_{31}^2 \quad (4.17)$$

$$C_{23} = \left( \frac{N_0}{3\varepsilon_0\gamma_0} \right) \mu_{21} \cdot \mu_{31} \quad (4.18)$$

Here  $N_0$  is the concentration of quantum dots. Note that the coupling constants are measured with respect to  $\gamma_0$ .



Quantum dots are also interacting with bound photons through the EBP interaction. Therefore, excited states  $|3\rangle$  and  $|2\rangle$  decay to  $|1\rangle$  due to the EBP interaction. The EBP Hamiltonian for the system is written as:

$$\begin{aligned}
H_{EBP} = & \sum_{j=2,3} \varepsilon_{j1} \sigma_{j1}^z + \sum_{n,m,k_z} \varepsilon_{nmk_z} P_{nmk_z}^+ P_{nmk_z} \\
& - \sum_{j=2,3} \sum_{n,m,k_z} \left( \sqrt{\frac{\varepsilon_{nmk_z} \mu_{j1}^2}{2\varepsilon_0 V}} \right) P_{nmk_z} \sigma_{j1}^+ e^{i(\varepsilon_{j1} - \varepsilon_{nmk_z})t/\hbar} + h.c.
\end{aligned} \tag{4.19}$$

where  $\sigma_{j\ell}^+ = |j\rangle \langle \ell|$  and  $\sigma_{j1}^z = |j\rangle \langle j| - |1\rangle \langle 1|$ . Here,  $j$  and  $\ell$  stand for energy levels of a quantum dot. The resonant energy  $\varepsilon_{j\ell}$  corresponds to transition  $|j\rangle \leftrightarrow |\ell\rangle$ . The first and second terms correspond to the Hamiltonian of a quantum dot and of bound photons in the nanofiber, respectively. The third term (the term with  $\mu_{j1}$ ) denotes the decay of levels  $|3\rangle$  and  $|2\rangle$  to the level  $|1\rangle$ . Operators  $p_{nmk_z}$  and  $p_{nmk_z}^+$  are the photon annihilation and creation operators for bound photon energy state  $\varepsilon_{nmk_z}$ , respectively. Also,  $V$  is the volume of the nanofiber.

## 4.5 Density Matrix Method

In the interaction picture of quantum mechanics, the expectation value for an observable can be calculated by:

$$\langle A \rangle = Tr(\rho A) \tag{4.20}$$

where:

$$\rho = |\psi\rangle \langle \psi| \tag{4.21}$$

We now take the Schrodinger equation:

$$i\hbar \frac{d|\psi\rangle}{dt} = H|\psi\rangle \tag{4.22}$$

and we simply differentiate equation (4.21) to find:

$$\frac{d\rho}{dt} = \frac{d}{dt} (|\psi\rangle\langle\psi|) = \frac{d|\psi\rangle}{dt} \langle\psi| + |\psi\rangle \frac{d\langle\psi|}{dt} \quad (4.23)$$

From equation (4.22) we know:

$$i\hbar \frac{d\langle\psi|}{dt} = -\langle\psi| H \quad (4.24)$$

This leads us to:

$$i\hbar \frac{d\rho}{dt} = [H, \rho] \quad (4.25)$$

## 4.6 Reduced Density Matrix

In the Hamiltonian given in equation (4.19), there are creation and annihilation operators for both photons and excitons. This means that the density matrix given in equation (4.25) will have elements both for photon states and exciton states in the quantum dots. We define a reduced density matrix for only the excitonic states. This means taking the trace over the photon reservoir states, so that only the excitonic states remain:

$$\rho_e \equiv Tr_R(\rho_{eR}) \quad (4.26)$$

In the interaction picture, the Hamiltonian is split up into two parts. First, there are the separate exciton and photon portions of the Hamiltonian,  $H_0$ , and second there are the interaction portions of the Hamiltonian,  $V$ . The density matrix is now defined as:

$$\rho_I = e^{iH_0t/\hbar} \rho e^{-iH_0t/\hbar} \quad (4.27)$$

so that:

$$i\hbar \frac{d\rho_I}{dt} = [V_I, \rho_I] \quad (4.28)$$

If we integrate this, we find:

$$\rho_{eR}(t) = \rho_{eR}(0) - \frac{i}{\hbar} \int_0^t dt' [V_{eR}(t'), \rho_{eR}(t')] \quad (4.29)$$

Next, this is used in equation (4.28) to yield:

$$\frac{d\rho_{eR}(t)}{dt} = -\frac{i}{\hbar} [V_{eR}(t), \rho_{eR}(0)] - \frac{1}{\hbar^2} \int_0^t dt' [V_{eR}(t), [V_{eR}(t'), \rho_{eR}(t')]] \quad (4.30)$$

Lastly, equation (4.26) is used to find:

$$\frac{d\rho_e(t)}{dt} = -\frac{i}{\hbar} Tr_R ([V_{eR}(t), \rho_{eR}(0)]) - \frac{1}{\hbar^2} Tr_R \left( \int_0^t dt' [V_{eR}(t), [V_{eR}(t'), \rho_{eR}(t')]] \right) \quad (4.31)$$

This is the master equation which is used to find the density matrix equations for individual quantum dot states. This will be used in all subsequent chapters.

## 4.7 Density Matrix Equations for a 3-level Quantum Dot

Following equation (4.31) and the Hamiltonian derived thus far for the system in this chapter, the following density matrix equations can be derived:

$$\begin{aligned}
\frac{d\rho_{22}}{d\tau} &= -2\Gamma_2\rho_{22} + i(\Omega_{12} + C_{21}\rho_{21} + C_{23}\rho_{31})\rho_{12} - i(\Omega_{12} + C_{21}\rho_{12} + C_{23}\rho_{13})\rho_{21} & (4.32) \\
\frac{d\rho_{33}}{d\tau} &= -2\Gamma_3\rho_{33} + i(\Omega_{13} + C_{31}\rho_{31} + C_{23}\rho_{21})\rho_{13} - i(\Omega_{13} + C_{31}\rho_{13} + C_{23}\rho_{12})\rho_{31} \\
\frac{d\rho_{32}}{d\tau} &= -(\Gamma_{32} - i\delta_{21} + i\delta_{31})\rho_{32} - i(\Omega_{12} + C_{21}\rho_{12} + C_{23}\rho_{13})\rho_{31} \\
&\quad + i(\Omega_{13} + C_{31}\rho_{31} + C_{23}\rho_{21})\rho_{12} \\
\frac{d\rho_{21}}{d\tau} &= -[(\Gamma_{21} + \Gamma_2) - i\delta_{21}]\rho_{21} + i(\Omega_{12} + C_{21}\rho_{21} + C_{23}\rho_{31})(\rho_{11} - \rho_{22}) \\
&\quad - i(\Omega_{13} + C_{31}\rho_{31} + C_{23}\rho_{21})\rho_{23} \\
\frac{d\rho_{31}}{d\tau} &= -[(\Gamma_{31} + \Gamma_3) - i\delta_{31}]\rho_{31} - i(\Omega_{12} + C_{21}\rho_{21} + C_{23}\rho_{31})\rho_{32} \\
&\quad - i(\Omega_{13} + C_{31}\rho_{31} + C_{23}\rho_{21})(\rho_{33} - \rho_{11})
\end{aligned}$$

where:

$$\Gamma_{32} = (\Gamma_2 + \Gamma_3) \quad (4.33)$$

Here,  $\Gamma_j$  is the spontaneous decay rate for the transition  $|1\rangle \leftrightarrow |j\rangle$  in the absence of the DDI. Note that in the above, the dipole approximation and the rotating wave approximation were used.

## 4.8 Electric susceptibility

To measure the absorption coefficient from transition  $|1\rangle \leftrightarrow |2\rangle$ , we have applied a probe field. The absorption coefficient is obtained from the susceptibility  $\chi$ . In the linear approximation, the expression for the susceptibility is written as [129]:

$$\chi = \frac{N_0\mu_{21}^2\gamma_0\rho_{21}}{2\epsilon_0\hbar x_p} \quad (4.34)$$

where  $x_p = \Omega_{12}/\gamma_0$  and  $\rho_{21}$  is the expression for a density matrix element, which is evaluated as being linear in  $x_p$  so that it cancels out from the numerator and the denominator of the susceptibility expression. Therefore, the susceptibility does not depend on the strength of the probe field (i.e.  $x_p$ ) in the linear approximation.

It is useful and interesting, both from the point of view of theory and experiment to find an analytical expression for the susceptibility. The density matrix method has been developed for three-level quantum dots in references [39] and [125]. Using the method of these references, density matrix  $\rho_{21}$  has been calculated. The following approximations have been used to find an analytical expression for the absorption coefficient.

We consider dipole moments  $\mu_{21}$  and  $\mu_{31}$  as being perpendicular to each other. This means that the  $C_{23}$  term does not contribute. The density matrix element  $\rho_{31}$  appearing in equation (4.15) is evaluated in the absence of the DDI. By making this approximation, the third and higher order terms of the DDI Hamiltonian containing the  $C_{31}$  term have been neglected. This means that only the second order terms in the  $C_{31}$  coupling have been included in our calculations. In fact, this is an excellent approximation. All orders of the  $C_{21}$  coupling have been included in this calculation. Similarly, all orders of the control field  $x_c = \Omega_{13}/\gamma_0$  are also included in the calculation of the susceptibility. Without the above two approximations, an analytical expression can not be obtained.

After some mathematical manipulations, the following expression for the susceptibility has been obtained from equation (4.34):

$$\chi_{dd} = \chi_0 \left( \frac{\xi_1 \xi_2 + \xi_3}{d_{13} (d_{21} d_{23} + |x_c + C_{31} \xi_4|^2) - C_{21} (\xi_1 \xi_2 + \xi_2)} \right) \quad (4.35)$$

The susceptibility expression has the effect of dipole-dipole coupling through the coupling constants  $C_{21}$  and  $C_{31}$ . Note that second order terms in  $C_{31}$  have been included in our calculations. The variable  $\chi_0$  is a constant and is written as:

$$\chi_0 = \frac{2N_0\mu_{21}^2}{\hbar\epsilon_0\gamma_0} \quad (4.36)$$

Functions  $\xi_1$ ,  $\xi_2$ ,  $\xi_3$ , and  $\xi_4$  are obtained as:

$$\xi_1 = i(2|x_c + C_{31}\xi_4|^2 - d_{23}d_{13}) \quad (4.37)$$

$$\xi_2 = \frac{|x_c|^2(d_{31} + d_{13})}{\gamma_{31}d_{31}d_{13} + 2|x_c|^2(d_{31} + d_{13})} \quad (4.38)$$

$$\xi_3 = i(d_{23}d_{13} - |x_c + C_{31}\xi_4|^2) \quad (4.39)$$

$$\xi_4 = i\frac{x_c}{d_{31}}(1 - 2\xi_2) \quad (4.40)$$

where  $d_{31} = \delta_{31} - \Gamma_{31}/2$ ,  $d_{13} = d_{31}^*$ ,  $d_{32} = (\delta_{31} - \delta_{21}) - (\Gamma_{31} + \Gamma_{21})/2$ , and  $d_{21} = \delta_{21} - (\Gamma_{21})/2$ . The parameters  $\delta_{21}$  and  $\delta_{31}$  are called the probe and control field detunings, respectively, and are defined as:  $\delta_{21} = (\varepsilon_{21} - \Delta_{21} - \varepsilon_p)$  and  $\delta_{31} = (\varepsilon_{31} - \Delta_{31} - \varepsilon_p)$ . In the calculation of the susceptibility, the probe and control detunings are used as variables.

Parameters  $\Delta_{j1}$  and  $\Gamma_{j1}$  in the above paragraph are the real and imaginary parts of self energy  $\Xi_{j1}$ . Here  $j = 2$  and  $3$ . The self energy is found to be:

$$\Xi_{j1} = \left(\frac{\varepsilon_{j1}\mu_{j1}^2}{2\hbar\epsilon_0V}\right) \sum_{nm} \int D(\varepsilon_{nmk_z}) d\varepsilon_{nmk_z} \left(\frac{1}{(\varepsilon_{nmk_z} - \varepsilon_{j1}) - i\gamma_{j1}}\right); \quad j = 2, 3 \quad (4.41)$$

where  $\gamma_{21}$  and  $\gamma_{31}$  are decay linewidths for the transitions  $|2\rangle \leftrightarrow |1\rangle$  and  $|3\rangle \leftrightarrow |1\rangle$  in the absence of the EBP interaction, and  $D(\varepsilon_{nmk_z})$  is given in equation (4.13). Using the DOS expressions

to find self-energies yields:

$$\Delta_{j1} = \left( \frac{\varepsilon_{j1}^{3/2} \mu_{j1}^2 n_d}{\sqrt{2} \hbar^2 c \varepsilon_0 d_x d_y} \right) \sum_{nm} \frac{\cos(\phi_{j1}/2)}{\left[ \sqrt{(\varepsilon_{nm} - \varepsilon_{j1})^2 + \gamma_{j1}^2} \right]^{1/4}}; \quad j = 2, 3 \quad (4.42)$$

Note that the real parts of the self energies shift the transition energies of the quantum dots, since  $\delta_{21} = (\varepsilon_{21} - \Delta_{21} - \varepsilon_p)$ , for example. Similarly, the imaginary part  $\Gamma_{j1}$  is obtained as:

$$\Gamma_{j1} = \sum_{nm} \frac{\eta_{j1}}{\left[ (\varepsilon_{nm} - \varepsilon_{j1})^2 + \gamma_{j1}^2 \right]^{1/4}}; \quad j = 2, 3 \quad (4.43)$$

$$\eta_{j1} = \left( \frac{\varepsilon_{j1}^{3/2} \mu_{j1}^2 n_d \sin \phi_{j1}/2}{\sqrt{2} \hbar^2 c \varepsilon_0 d_x d_y} \right); \quad j = 2, 3 \quad (4.44)$$

$$\phi_{j1} = \arctan \left( \frac{\gamma_{j1}}{\varepsilon_{nm} - \varepsilon_{j1}} \right); \quad j = 2, 3 \quad (4.45)$$

The imaginary part of the self energy is also called the linewidth. Note that linewidths have a very large value when the resonance energy  $\varepsilon_{ij}$  lies near a bound state  $\varepsilon_{nm}$ . The expression of the susceptibility can be further simplified if we substitute the expression of  $\xi_1$  and  $\xi_3$  into equation (4.35):

$$\chi_{dd} = \chi_0 \frac{i \left[ |x_c + C_{31} \xi_4|^2 (2\xi_2 - 1) + d_{23} d_{13} (1 - \xi_2) \right]}{d_{13} \left( d_{21} d_{23} + |x_c + C_{31} \xi_4|^2 \right) - C_{21} \left[ |x_c + C_{31} \xi_4|^2 (2\xi_2 - 1) + d_{23} d_{13} (1 - \xi_2) \right]} \quad (4.46)$$

We have also calculated an expression for the susceptibility in the absence of the control field. In this case, the  $C_{31}$  coupling is also absent. We found the following expression:

$$\chi_{dd} = \chi_0 \left( \frac{i}{i(\delta_{21} + C_{21}) + (\Gamma_{21})/2} \right) \quad (4.47)$$

Note that the DDI due to the  $C_{21}$  coupling shifts the probe detuning. This point has been

verified numerically in the next section. A similar expression for the susceptibility to the above equation was calculated in reference [130] for a dense resonance medium. In that paper, the Lorentz local field shift had also been measured for a dense potassium vapor. In the absence of the DDI (i.e.  $H_{dd} = 0$ ) the susceptibility has also been calculated. It has the following form:

$$\chi_{dd} = \chi_0 \left( \frac{i \left[ |x_c|^2 (2\xi_2 - 1) + d_{23}d_{13} (1 - \xi_2) \right]}{d_{13} (d_{21}d_{23} + |x_c|^2)} \right) \quad (4.48)$$

Note that the expression for the susceptibility is nonlinear in the control field.

## 4.9 Simulations of the Absorption Coefficient

We consider a photonic crystal made from the silica spheres which are periodically arranged in air. The embedded dielectric material is also made from silica. Crystal parameters for the nanofiber are taken as  $n_p = n_d = 1.45$ ,  $L = 250$  nm and  $r = 0.23L$ . Other parameters are taken as  $\gamma_{31} = 0.001\gamma_0$  [125], [126],  $\gamma_{21} = \gamma_0$  [125], [126], and  $\eta_{21} = \eta_{31} = 0.1\gamma_0$ . The energy gap for this crystal has been calculated from equation (4.1), and it lies between 1.015 eV and 1.341 eV.

The size of the nanofiber is taken to be  $d_x = d_y = 250$  nm. We have calculated bound photon energies for the nanofiber. One bound state is found within the band gap of the photonic crystal. It is located at  $\varepsilon_{00} = 1.254$  eV, where  $\varepsilon_{00}$  is the ground state of the nanofiber. All the energies in this section are measured in terms of the linewidth  $\gamma_0$ . For simplicity, it is taken as 1.0 meV [14], [49], [50]. In this representation, the bound states energy can be rewritten as  $\varepsilon_{00} = 1254$ .

The normalized absorption coefficient  $Im(\chi_{dd}/\chi_0)$  has been calculated as a function of the probe detuning parameter  $\delta_{21}$ . The control field is taken to be resonant with the transition  $|1\rangle \leftrightarrow |3\rangle$ . This makes the control field detuning equal to zero. The probe detuning parameter



is measured with respect to  $\gamma_0$ . Linewidths are calculated when resonance energies of quantum dots lie away from the bound state (i.e.  $\varepsilon_{21} = \varepsilon_{31} = 1330$ ).

All simulations presented here were performed using the software package, Maple. The density matrix equations (4.32) were used to find equilibrium values for the density matrix elements, assuming initial conditions such that all populations is in the ground state. In other words,  $\rho_{11}^0 = 1$ , and  $\rho_{j\ell}^0 = 0$  for all other values of  $j$  and  $\ell$ . Since analytical expressions using the stated approximations produce qualitatively similar results to those produced numerically, only the analytical results were shown here. The same procedure was used to evaluate the density matrix elements for all subsequent chapters, except that analytical expressions were not obtained in those cases.

Let us first calculate the absorption coefficient when the control field is absent. This makes  $C_{31}$  and  $x_c$  zero. The results are plotted in figure 4.3. The solid and dashed curves correspond to  $C_{21} = 0$  and  $C_{21} = 2$ , respectively. Note that the absorption peak shifts to the right due to the  $C_{21}$  coupling. The shift is approximately proportional to the  $C_{21}$  coupling. This behavior is due to the additional dynamical detuning, and is added to the absorption coefficient due to this interaction. This effect is shown theoretically in equation (4.47). That is why there is a shift in the absorption spectrum. This type of behavior has also been observed in atomic gasses [38], [39], [40], and photonic crystals [46], [47], [48].

Now let us apply a very weak control field in the system. The strength of the control field is taken as  $x_c = 0.1$ . In this case, the DDI due to the transition  $|1\rangle \leftrightarrow |3\rangle$  contributes to the absorption coefficient. The results are plotted in figure 4.4. The solid and dashed curves are plotted for  $C_{31} = 0$  and  $C_{31} = 5$ , respectively. The other coupling term is taken as  $C_{21} = 2$ . Note that the absorption spectrum splits into two peaks in the presence of the  $C_{31}$  coupling, and a minimum appears between the two peaks. This minimum corresponds to a transparent state. This is an interesting result which predicts that the system can be switched from an absorbing state to a transparent state due to the DDI.

We have also calculated the energy separation (i.e. energy splitting) between two peaks in

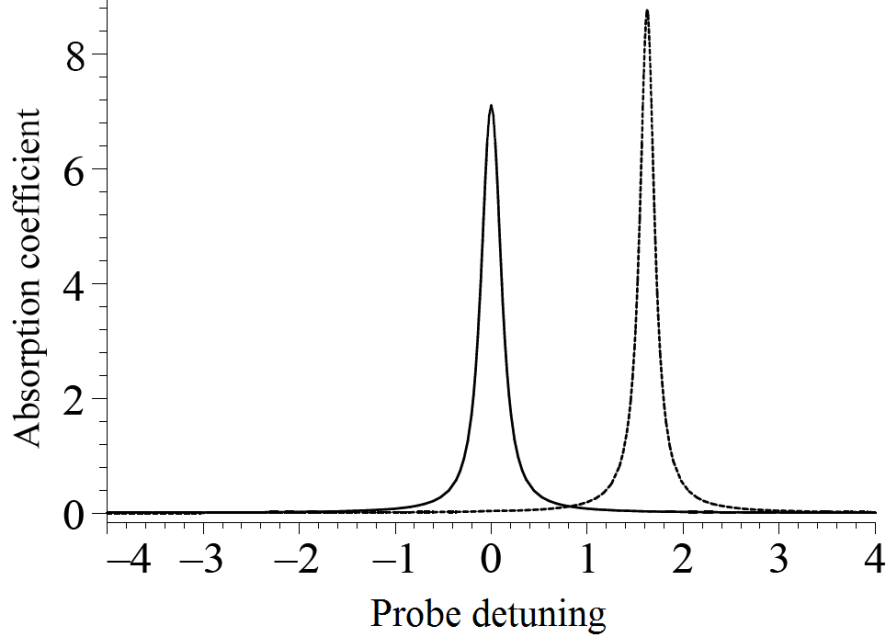


Figure 4.3: The absorption coefficient  $Im(\chi_{dd}/\chi_0)$  is plotted as a function of the normalized probe detuning  $\delta_{21}$  when the control field is absent. The solid and dashed lines correspond to  $C_{21} = 0$  and  $C_{21} = 2$ , respectively. Note that the absorption peak shifts to the right due to the DDI. Linewidths are calculated when both resonance energies  $\varepsilon_{21}$  and  $\varepsilon_{31}$  lie far away from  $\varepsilon_{00}$ .

the absorption spectrum due to the DDI parameter  $C_{13}$ . Let us denote the energy splitting as  $\Delta\varepsilon$ . As the DDI parameter increases, the energy splitting is also found to increase. For example, we found that  $\Delta\varepsilon = 2.3$ ,  $\Delta\varepsilon = 3.6$ , and  $\Delta\varepsilon = 4.9$  for  $C_{31} = 3$ ,  $C_{31} = 5$ , and  $C_{31} = 7$ , respectively.

The phenomenon of transparency can be explained by using physics of dressed states [49], [50], [131]. We have shown in figure 4.3 that the coupling  $C_{21}$  shifts the location of the absorption peak but does not split it. Therefore, it is not responsible for the splitting of the peak. In the absence of the coupling  $C_{31}$ , only one transition route,  $|1\rangle \rightarrow |2\rangle$  is available for absorption. That is why we get one absorption peak represented by the solid line in figure 4.4. However, in the presence of a strong  $C_{31}$  coupling, the level  $|1\rangle$  splits into two dressed states,  $|1_{-}\rangle$  and  $|1_{+}\rangle$ . The energy splitting of these dressed states is proportional to this coupling. Now the system has two routes which are available for the absorption process (i.e.  $|1_{-}\rangle \rightarrow |2\rangle$  and  $|1_{+}\rangle \rightarrow |2\rangle$ ). This is the reason the single absorption peak splits into two absorption peaks,

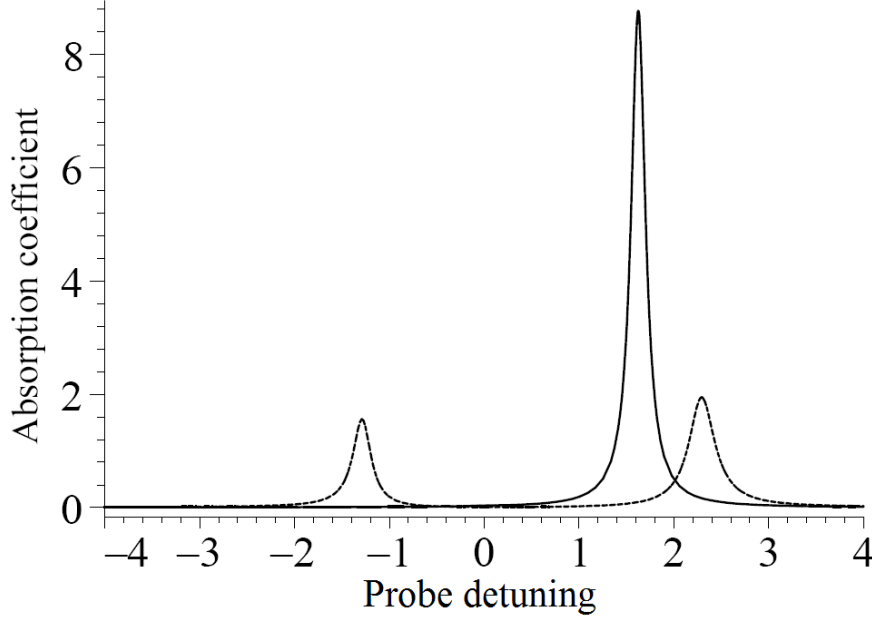


Figure 4.4: The absorption coefficient  $Im(\chi_{dd}/\chi_0)$  is plotted as a function of the normalized probe detuning  $\delta_{21}$  when the control field is present. The solid and dashed lines correspond to  $C_{31} = 0$  and  $C_{31} = 5$ , respectively. Note that the absorption peak splits into two peaks due to the dipole-dipole coupling  $C_{31}$ . The  $C_{21}$  coupling is taken as  $C_{21} = 2$ . Linewidths are calculated when both resonance energies  $\varepsilon_{21}$  and  $\varepsilon_{31}$  lie far away from  $\varepsilon_{00}$ .

and the spectrum contains a transparent state between two peaks.

A similar type of splitting in the absorption peak has been observed in atomic gases due to the EIT phenomenon [129]. When an intense pump laser is applied to a quantum dot, the coupling between the quantum dot and the pump laser field becomes very strong. The transition energy of the quantum dot then splits into two dressed states. For this reason, the absorption peak splits into two peaks, and a transparent state appears between two peaks. This is known as the EIT phenomenon. On the other hand, the splitting of the absorption peak in this chapter is due to the DDI. The EIT phenomenon has been studied in a three-level quantum dot doped in a photonic crystal [132], [133].

Next, we consider the effect of the EBP coupling on the DDI. The EBP coupling is nothing but the interaction between quantum dots and bound photons. We know that the resonance energy  $\varepsilon_{31}$  moves towards the ground photon state  $\varepsilon_{00}$ . On the other hand, the transition energy  $\varepsilon_{21}$  remains in the same place as in figures 4.3 and 4.4. The solid, dashed, and dotted lines in

figure 4.5 are calculated when resonance energy  $\varepsilon_{31}$  lies at 1330, 1260, and 1256, respectively. It is interesting to note that as the resonant energy nears the ground state energy, (i.e. 1254) the two peaks merge into one peak, and the transparent state disappears.

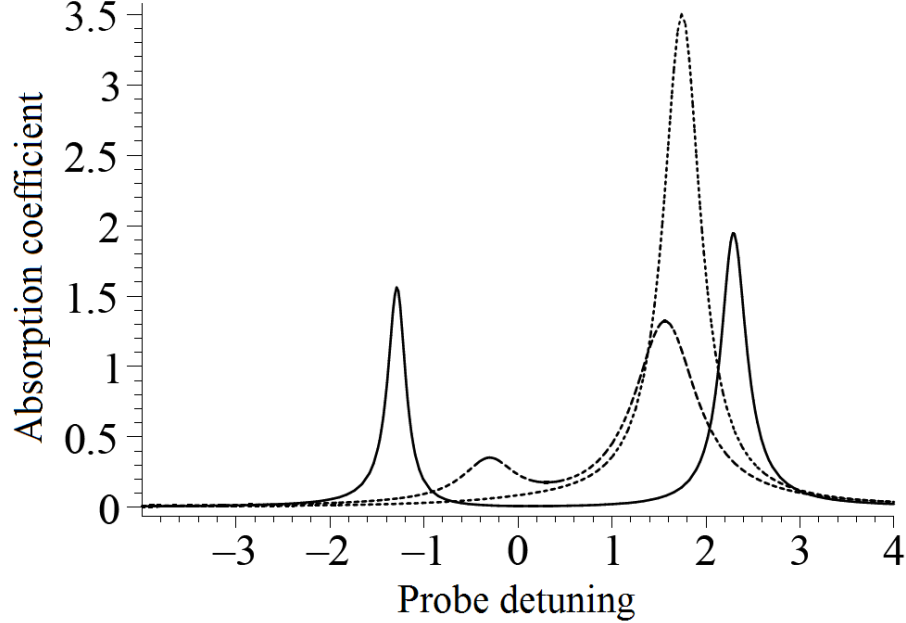


Figure 4.5: In this figure, the effect of the EBP interaction due to the linewidth  $\Gamma_{31}$  is presented. The absorption coefficient  $Im(\chi_{ad}/\chi_0)$  is plotted as a function of the normalized probe detuning  $\delta_{21}$  when the control field is present. Parameters are taken as  $C_{31} = 5$  and  $C_{21} = 2$ . The solid, dashed, and dotted lines are calculated when resonance energy  $\varepsilon_{31}$  lies at 1330, 1260 and 1256, respectively.

The results found in figure 4.5 can be explained as follows. The broadening of the two peaks depends on  $\Gamma_{31}$ . When the transition energy  $\varepsilon_{31}$  lies near the bound photon state  $\varepsilon_{00}$ , this linewidth has a very large value (see equation (4.28)). The large value is due to the DOS of the nanofiber. The DOS is plotted in figure 4.6 near the bound photon energy  $\varepsilon_{00}$ . One can see that the DOS has a singularity near the bound photon state. In this situation, the linewidths of the two peaks become larger than the energy splitting due to the  $C_{31}$  coupling, which means that two peaks merge into one peak. The height of the absorption peaks also depends on linewidths. Therefore, the linewidth  $\Gamma_{31}$  also affects the height of these peaks.

We have shown in figures 4.4 and 4.5 that the absorption peak splits from one peak to two peaks by the DDI between the quantum dots. The splitting of the peak can be controlled by

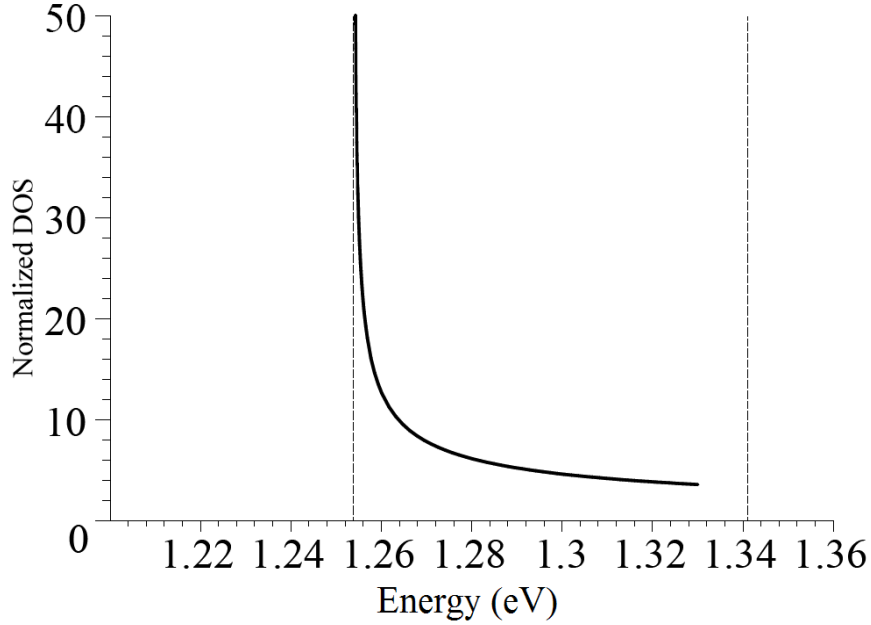


Figure 4.6: The normalized DOS is plotted as a function of energy near the photon bound state  $\epsilon_{00}$ .

changing the location of the resonant energy of the quantum dots. In figure 4.5 it is shown that as the resonance energy changes with respect to the bound photon energy, the system switches from a transparent state to an absorbing state (i.e. two peaks to one peak). This can be achieved by applying a pulse electric field or a pulse magnetic field to the quantum dots.

The splitting of the peak can also be controlled by the control field. Note that in figure 4.4, the absorption peak splits into two peaks due to the  $C_{31}$  coupling which is induced by the control field. Finally, the splitting can also be controlled by changing the concentration of quantum dots. This can be done by applying a temperature pulse to the nanowire.

Recently, Yoshie et al. [134] and Hennessy et al. [135] have studied experimentally the crossover between strong and weak coupling regimes when quantum dots are doped in photonic crystal cavities. They found that the absorption spectrum splits into two peaks when the coupling between the electromagnetic field and a quantum dot exceeds the decay rates of the cavity and the quantum dot. This is known as Rabi splitting. The Rabi splitting in three-level atoms in the V-level scheme in the presence of a control field has also been investigated by Sautenkov et al. [136]. They have experimentally studied the reflection of a weak probe

beam from a dense atomic potassium vapor in the presence of a strong laser field tuned to the atomic resonance transition. They have observed an Autler-Townes doublet when the Rabi frequency induced by the strong laser field is much smaller than the self-broadened width of the resonance transition of the unexcited vapor. They attributed their observation to a reduction of the atomic decoherence by the strong drive field. However, in this chapter, the absorption peak splits into two peaks when the dipole-dipole coupling is larger than the decay rate of the quantum dot.

## 4.10 Conclusion

The effect of the DDI has been investigated in quantum dots which are doped in photonic nanofibers prepared by embedding a dielectric material into a photonic crystal. These nanofibers have bound photon energy states. The embedded material is doped with an ensemble of three-level quantum dots. Then, probe and control fields are applied to monitor the absorption coefficient. Due to these fields, dipoles are induced in quantum dots which are interacting with each other via the DDI. Quantum dots are also interacting with the quantum nanofiber through the EBP interaction. The absorption coefficient has been calculated using the density matrix method, and the DDI has been evaluated in the mean field approximation. It was found that the system can be changed from a transparent state to an absorbing state by the DDI. It has also been predicted that by changing either the locations of resonant transitions in the quantum dots or the location of the bound photon state in the nanofiber, the absorption peak can be split into a transparent peak and two absorbing peaks. While this behaviour has been seen in other systems, this is the first prediction we are aware of where these DDI effects have produced this level of splitting for V-type quantum dots in a photonic fiber.

# Chapter 5

## Controlling the photoluminescence of acceptor and donor quantum dots embedded in a nonlinear photonic crystal<sup>1</sup>

In the previous chapter, optoelectronic properties and dipole-dipole interactions has been discussed for quantum dots doped into a photonic nanowire. In this chapter, we will develop a theory for photoluminescence between two quantum dots deposited on a photonic crystal. The theoretical results are compared with experiments.

### 5.1 Introduction

Semiconductor quantum dots (QDs) have been intensively used to study the optical properties of biological, chemical, and metallic hybrid nanosystems because their excitation energy is tunable to optical properties by simply changing their size [51], [52], [53]. Recently, there

---

<sup>1</sup>Reprinted with permission from M. R. Singh, C. Racknor, and D. Schindel, Applied Physics Letters, vol. 101, p. 051115, (2012). Copyright 2012, American Institute of Physics.

has been considerable interest in studying energy transfer in QD-metallic nanostructure hybrid systems [51], [52]. Metallic nanostructures greatly enhance a variety of optical processes which are due to the interaction between an exciton in the QD and the enhanced local electromagnetic field of a metal-surface plasmon. Light-harvesting, photovoltaics [137], and surface plasmon-enhanced fluorescence [55] have also been studied in these hybrid systems.

The photoluminescence (PL) spectrum of QDs, in contrast to conventional organic dyes, possess high quantum yield, narrow and stable fluorescence, and size-dependent absorption and emission [56]. They have been used as excellent fluorescent labels for biological imaging and sensing [57]. QDs have broad absorption and narrow emission spectra, and hence they are used as donors of fluorescence resonance energy transfer. QD based hybrid systems have also been used for bio-sensing, [59] solar cells, [58] and light harvesting. These hybrid systems employ resonant energy transfer to generate energy flow from a donor QD to an acceptor QD. The energy transport occurs in the nanoscale range via dipole-dipole interactions (DDIs), which depend on spectral overlap in the emission spectrum of the donor with the absorption spectrum of the acceptor, and the distance between the donor and acceptor. Based on energy transfer mechanisms, a series of QD-based biosensors have been developed [59].

## 5.2 Quantum Dot Energy Transfer

In this chapter we study the energy transfer rate and PL quantum efficiency between donor and acceptor QDs embedded in a nonlinear photonic crystal. The photonic crystal structure consists of a periodic arrangement of nonlinear dielectric spheres (polystyrene) in a dielectric background material (air). These photonic crystals have been fabricated recently [138]. The refractive index of the dielectric spheres and the background dielectric material are denoted as  $n_a$  and  $n_b$ , respectively. Let  $a$  be the radius of the dielectric spheres and let  $b$  be half the distance between two spheres. The dispersion relation of the Bloch photons for this photonic crystal has already been calculated by John's group [122] and is written as:



$$\cos(kL) = F(\omega_k) \quad (5.1)$$

$$F(\omega_k) = \sum_{\pm} \left[ \pm \frac{(n_a \pm n_b)^2}{4n_a n_b} \cos\left(\frac{4\omega_k \beta_{\pm}}{c}\right) \right] \quad (5.2)$$

$$\beta_{\pm} = (n_a a \pm n_b b) \quad (5.3)$$

where  $L = 2a + 2b$  is the lattice constant. We consider that acceptor and donor QDs have three excitonic states which are denoted as  $|1\rangle$ ,  $|2\rangle$ , and  $|3\rangle$ , where  $|1\rangle$  is the ground state and  $|2\rangle$  and  $|3\rangle$  are excited states. This is known as the ladder-type QD configuration in the literature, and has been used in the study of a QD-metallic nanoparticle hybrid system [84]. A V-type configuration QD interacting with a metallic nanoparticle has also been studied in the presence of two external laser fields [139]. A schematic diagram for the hybrid system is shown in figure 5.1. In chapter 4, quantum dots were considered within a photonic nanofiber, in this chapter, they rest on a photonic substrate. Also, chapter 4 used a V-type quantum dot, whereas here we have used a ladder-type quantum dot. Finally, if one compares the DDI treatment presented in this chapter to that of chapter 4, they would not be an equivalent treatment unless  $\mu_{12}\mu_{23} = 0$ .

A probe field  $E_2$  is applied to excite the first exciton between  $|1\rangle$  and  $|2\rangle$  with an energy difference of  $\hbar\omega_{12}$ , where:

$$E_2 = E_2^0 \cos(\omega_2 t) \quad (5.4)$$

Similarly, a second exciton is created by applying a control laser field,  $E_3$  between states  $|2\rangle$  and  $|3\rangle$ , with an energy difference of  $\hbar\omega_{23}$ , where:

$$E_3 = E_3^0 \cos(\omega_3 t) \quad (5.5)$$

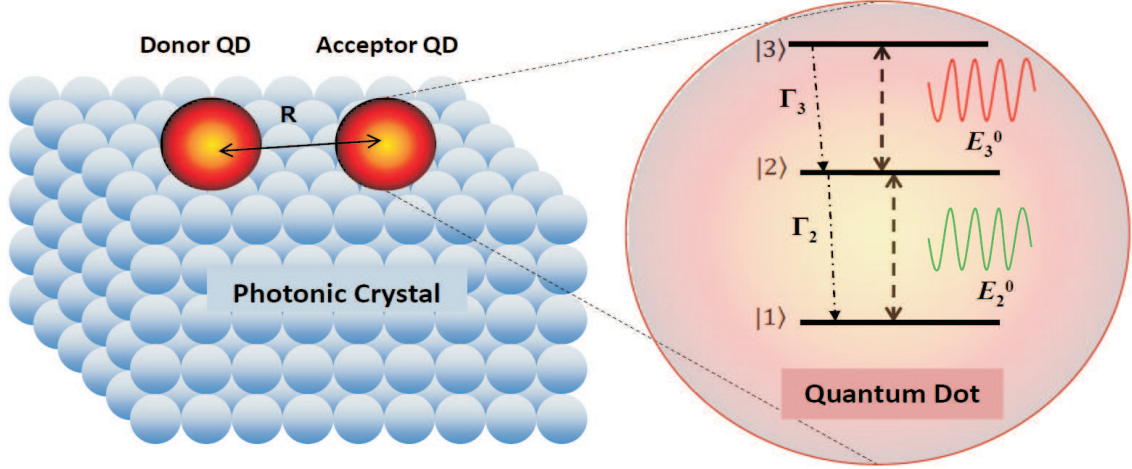


Figure 5.1: Schematic diagram of a three level atom embedded in the photonic crystal. The parameters used in the present calculation are taken as  $n_a = 1.59$ ,  $n_b = 1$ ,  $a = 100$  nm, and  $L = 400$  nm. The band gap of this photonic crystal has been calculated to lie between energies  $\varepsilon_v = 1.031$  eV and  $\varepsilon_c = 1.358$  eV. The induced dipole moment of the QD is taken as  $\mu_{12} = \mu_{23} = 0.4$  e nm and its dielectric constant is  $\varepsilon_d = 6$ . The vacuum decay rates for the QD are taken as  $\Gamma_2^0 = \Gamma_3^0 = 1$   $\mu$ eV.

The probe and control electric fields induce dipole moments in the donor and acceptor QDs. The donor and acceptor therefore interact with each other via the dipole-dipole interaction. The polarization produced due to the induced dipole in the acceptor is denoted as  $P_a$ , and is expressed as [129]:

$$P_a = \mu_{12}\rho_{12} + \mu_{23}\rho_{23} \quad (5.6)$$

where  $\mu_{j\ell}$  and  $\rho_{j\ell}$  are the dipole and density matrix elements between states  $|j\rangle$  and  $|\ell\rangle$ , respectively. The polarization in the acceptor creates a dipole electric field  $E_{ddi}^a$  at the donor:

$$E_{ddi}^a = \frac{S_r P_a}{(4\pi\epsilon_0) \epsilon_{eff} R^3} \quad (5.7)$$

where  $R$  is the distance between the acceptor and donor and  $S_r$  is called the polarization parameter which has the value  $S_r = 2$ . Here,

$$\epsilon_{eff} = \frac{3\epsilon_{pc}}{(2\epsilon_{pc} + \epsilon_d)} \quad (5.8)$$

where  $\epsilon_d$  is the dielectric constant of the QDs and  $\epsilon_{pc}$  is the dielectric constant of the photonic crystal, which can be calculated from the dispersion relation of the photonic crystal as follows.

The speed of Bloch photons  $v_{ph}$  is defined as:

$$v_{ph} = \frac{d\omega_k}{dk} \quad (5.9)$$

The phase velocity and the dielectric constant of the photonic crystal are related by the identity:

$$v_{ph} = \frac{c}{\sqrt{\epsilon_{pc}}} \quad (5.10)$$

where  $c$  is the speed of light in a vacuum. With the help of the dispersion relation, the dielectric constant of the photonic crystal is obtained as:

$$\epsilon_{pc}(\omega_k) = \frac{c^2 \zeta(\omega_k)}{L^2 [1 - F^2(\omega_k)]} \quad (5.11)$$

$$\zeta(\omega_k) = \frac{(n_a - n_b)^2 \beta_-}{2n_a n_b c} \sin\left(\frac{4\omega_k \beta_-}{c}\right) - \frac{(n_a + n_b)^2 \beta_+}{2n_a n_b c} \sin\left(\frac{4\omega_k \beta_+}{c}\right) \quad (5.12)$$

Note that  $\epsilon_{pc}$  is frequency dependent. As with all previous cases, the photonic crystal is treated in bulk, with a dielectric function that varies in frequency space, but not in real space. The expression for the acceptor electric field  $E_{ddi}^a$  after putting the expression for the polarization in becomes:

$$E_{ddi}^a = \left(\frac{\hbar}{\mu_{12}}\right) \Lambda_{12} \rho_{12} + \left(\frac{\hbar}{\mu_{23}}\right) \Lambda_{23} \rho_{23} \quad (5.13)$$

$$\Lambda_{j\ell} = \frac{3\epsilon_{pc}(\omega_{j\ell}) \mu_{j\ell}^2 S_r}{\hbar (4\pi\epsilon_0) [2\epsilon_{pc}(\omega_{j\ell}) + \epsilon_d] R^3} \quad (5.14)$$

where  $j\ell = 12, 23$ . Note that the dipole electric field depends on the density matrix elements  $\rho_{12}, \rho_{23}$ , and the distance between the acceptor and the donor.

The importance of equation (5.7) is worth describing in more detail here. There are two main effects which will be investigated in this chapter. The first is energy transfer from one quantum dot to another. This energy transfer occurs in the following way: the acceptor quantum dot acquires a dipole moment from interactions with the external fields. This dipole moment produces its own electric field. That dipole field interacts with the donor quantum dot, which we are interested in. However, that dipole field had to propagate through the photonic crystal in order to reach the donor quantum dot. Thus, the dielectric function for the photonic crystal controls interactions between the quantum dot. Nonlinearities in the photonic crystal enable us to change that dielectric function, so that these interactions may be controlled. This control is the second major effect investigated in this chapter.

### 5.3 Interaction Hamiltonian

Let us now calculate the DDI between the acceptor and donor. The dipole electric field  $E_{ddi}^a$  produced by the acceptor interacts with the dipole of the donor QD. Therefore, the DDI Hamiltonian between the donor and acceptor in the dipole and rotating wave approximations is:

$$H_{ddi} = -\hbar\Lambda_{12}\rho_{12}\sigma_{21}^+ - \hbar\Lambda_{23}\rho_{23}\sigma_{32}^+ + hc \quad (5.15)$$

where  $\sigma_{j\ell}^+ = |j\rangle\langle\ell|$  is called the exciton creation operator for the donor QD and  $hc$  stands for the Hermitian conjugate. Here,  $\Lambda_{12}$  and  $\Lambda_{23}$  are called the DDI coupling parameters. Note that this differs from the DDI Hamiltonian presented in chapter 4 in that there are no cross-terms, and the quantum dot has a different level structure. Also, the DDI coupling parameters are different. The photonic crystal acts as a reservoir for the donor and acceptor QDs, leading excitons to interact with Bloch photons and decay spontaneously from state  $|2\rangle$  to  $|1\rangle$  and from

state  $|3\rangle$  to  $|2\rangle$ . The interaction Hamiltonian is written as:

$$H_{int} = - \sum_k (g_{21} p_k \sigma_{21}^+ + g_{32} p_k \sigma_{32}^+) + hc \quad (5.16)$$

$$g_{j\ell} = \mu_{j\ell} \sqrt{\frac{\hbar \omega_k}{2\epsilon_0 V_{pc}}} \quad (5.17)$$

where  $V_{pc}$  is the volume of the photonic crystal. Here  $p_k$  is the lowering Bloch photon operator.

## 5.4 Density Matrix Method

Using equations (5.15) and (5.16) and the master equation [129], we obtained the following expressions for density matrix elements:

$$\begin{aligned} \dot{\rho}_{11} &= \Gamma_2 \rho_{22} + i(\bar{\Lambda}_{12}) \rho_{12} - i(\bar{\Lambda}_{12})^* \rho_{21} \\ \dot{\rho}_{33} &= -\Gamma_3 \rho_{33} + i(\bar{\Lambda}_{23})^* \rho_{32} - i(\bar{\Lambda}_{23}) \rho_{23} \\ \dot{\rho}_{32} &= (i\delta_{32} + i\Delta_{32} - \Gamma_{32}) \rho_{32} + i\bar{\Lambda}_{12}^* \rho_{31} + i\Omega_{23} (\rho_{33} - \rho_{22}) \\ \dot{\rho}_{21} &= (i\delta_{21} + i\Delta_{21} - \Gamma_{21}) \rho_{21} + i\Omega_{12} (\rho_{22} - \rho_{11}) - i\bar{\Lambda}_{23}^* \rho_{31} \\ \dot{\rho}_{31} &= (i\delta_{32} + i\delta_{21} - \Gamma_{31}) \rho_{31} - i\bar{\Lambda}_{23} \rho_{21} + i\bar{\Lambda}_{12} \rho_{32} \end{aligned} \quad (5.18)$$

where:

$$\bar{\Lambda}_{12} = \Omega_{12} + \Lambda_{12} \rho_{12} \quad (5.19)$$

$$\bar{\Lambda}_{23} = \Omega_{23} + \Lambda_{23} \rho_{23} \quad (5.20)$$

$$\Delta_{21} = \Lambda_{21} (\rho_{22} - \rho_{11}) \quad (5.21)$$

$$\Delta_{32} = \Lambda_{32} (\rho_{33} - \rho_{22}) \quad (5.22)$$

$$\Gamma_{j\ell} = \frac{(\Gamma_j + \Gamma_\ell)}{2} \quad (5.23)$$

$$\Gamma_2 = \Gamma_0 Z^2(\omega_{21}) \quad (5.24)$$

$$\Gamma_3 = \Gamma_0 Z^2(\omega_{32}) \quad (5.25)$$

$$\Omega_{12} = \frac{\mu_{12} E_2^0}{2\hbar} \quad (5.26)$$

$$\Omega_{23} = \frac{\mu_{23} E_3^0}{2\hbar} \quad (5.27)$$

Here,  $\Gamma_2$  and  $\Gamma_3$  are the spontaneous decay rates for the excited states  $|2\rangle$  and  $|3\rangle$ , respectively, and  $\Gamma_0$  is the decay rate for the excitons in the absence of the photonic crystal. The function  $Z(\omega_k)$  is called the form factor of the photonic crystal and is given in reference [140]. Constants  $\Omega_{12}$  and  $\Omega_{23}$  are the Rabi frequencies for the probe and control fields.

## 5.5 Energy Transfer Mechanism

Now we calculate the energy transfer rate (ETR) from the donor to the acceptor QD due to the DDI. The ETR is calculated using the method of reference [140]. First, the rate of energy lost to the external field due to the donor quantum dot is:

$$W_{QD} = \sum_{j\ell=12,23} \frac{\hbar^2 \omega_{j\ell}}{2\mu_{j\ell}^2} \text{Im}(\alpha_{j\ell}) |\Omega_{j\ell} + \Lambda_{j\ell} \rho_{j\ell}|^2 \quad (5.28)$$

$$\alpha_{12} = \frac{\mu_{12}\rho_{12}(\omega_{12})}{E_2^0} \quad (5.29)$$

$$\alpha_{23} = \frac{\mu_{23}\rho_{23}(\omega_{23})}{E_3^0} \quad (5.30)$$

where  $\alpha_{12}$  and  $\alpha_{23}$  are the polarizabilities for transitions  $|1\rangle \leftrightarrow |2\rangle$  and  $|2\rangle \leftrightarrow |3\rangle$ , respectively. Note that the energy loss depends on the density matrix elements  $\rho_{12}$  and  $\rho_{23}$ , along with the DDI parameters. The  $\Omega_{j\ell}$  term in equation (5.28) denotes energy loss from the donor QD due to stimulated emission from the two external fields. The  $\Lambda_{j\ell}\rho_{j\ell}$  term denotes energy loss due to DDI with an acceptor QD. These DDIs between QDs are the mechanism for energy transfer from a donor to an acceptor QD. The ETR from the donor to the acceptor is measured via the PL of the donor. The energy transfer is observed as a decrease of the donor's PL efficiency and an increase of the acceptor's PL efficiency. Generally, the energy transfer efficiency is defined as the relative change in the donor's PL emission [141]:

$$P_E = \frac{W_{QD}^0}{W_{QD}} \quad (5.31)$$

where  $W_{QD}^0$  is the power loss from the donor in the absence of the DDI. With the help of equation (5.28), the efficiency factor is found as:

$$P_E = \frac{\sum_{j\ell=12,23} \omega_{j\ell} \text{Im}(\alpha_{j\ell}) |\Omega_{j\ell}|^2}{\sum_{j\ell=12,23} \omega_{j\ell} \text{Im}(\alpha_{j\ell}) |\Omega_{j\ell} + \Lambda_{j\ell}\rho_{j\ell}|^2} \quad (5.32)$$

where we used  $\mu_{12} = \mu_{23}$ . Note that in the absence of the acceptor (i.e.  $\Lambda_{12} = \Lambda_{23} = 0$ ) the efficiency for the donor becomes  $P_E = 1$ .

The above theoretical formulation can be easily used for two-level acceptor and donor QDs by neglecting the effect of transition  $|2\rangle \leftrightarrow |3\rangle$ . In this case, expressions for the energy loss and the PL efficiency are obtained as:

$$W_{QD} = \left( \frac{\hbar^2 \omega_{12}}{2\mu_{12}^2} \right) \text{Im}(\alpha_{12}) |\Omega_{12} + \Lambda_{12}\rho_{12}|^2 \quad (5.33)$$

$$P_E = \frac{|\Omega_{12}|^2}{|\Omega_{12} + \Lambda_{12}\rho_{12}|^2} \quad (5.34)$$

If we neglect the cross terms between  $\Omega_{12}$  and  $\Lambda_{12}$ , then in this approximation the PL efficiency reduces to

$$P_E = \left[ 1 + \left( \frac{R_{ddi}}{R} \right)^6 |\rho_{12}|^2 \right]^{-1} \quad (5.35)$$

$$R_{ddi}^3 = \frac{\mu_{12}^2 S_r}{\hbar (4\pi\epsilon_0) \epsilon_{eff} \Omega_{12}} \quad (5.36)$$

Note that  $R_{ddi}$  comes out as a length. Sometimes  $R_{ddi}$  is called the Förster radius. Also note that  $P_E$  depends on  $R^6$  and density matrix element  $\rho_{12}$ .

## 5.6 Results and Discussion

We consider a photonic crystal that is made of polystyrene spheres embedded in air, and note that polystyrene is a nonlinear Kerr material. This type of photonic crystal has been fabricated by Liu et al. [138]. They have shown experimentally that the band gap of the photonic crystal in the presence of a pump field can be modified due to the Kerr effect. Decay rates  $\Gamma_2$  and  $\Gamma_3$  are both calculated to be  $3.5155 \mu\text{eV}$  in the absence of the Kerr effect, and  $5.4484 \mu\text{eV}$  in its presence. We consider probe and control fields that are parallel and perpendicular to the axis of the two quantum dots, respectively. The density matrix elements  $\rho_{j\ell}$  are obtained via solving equations (5.18) numerically using a seventh-eighth order continuous Runge–Kutta method provided by the software package Maple. Our results show that this method has a



rather higher precision in comparison to other available methods.

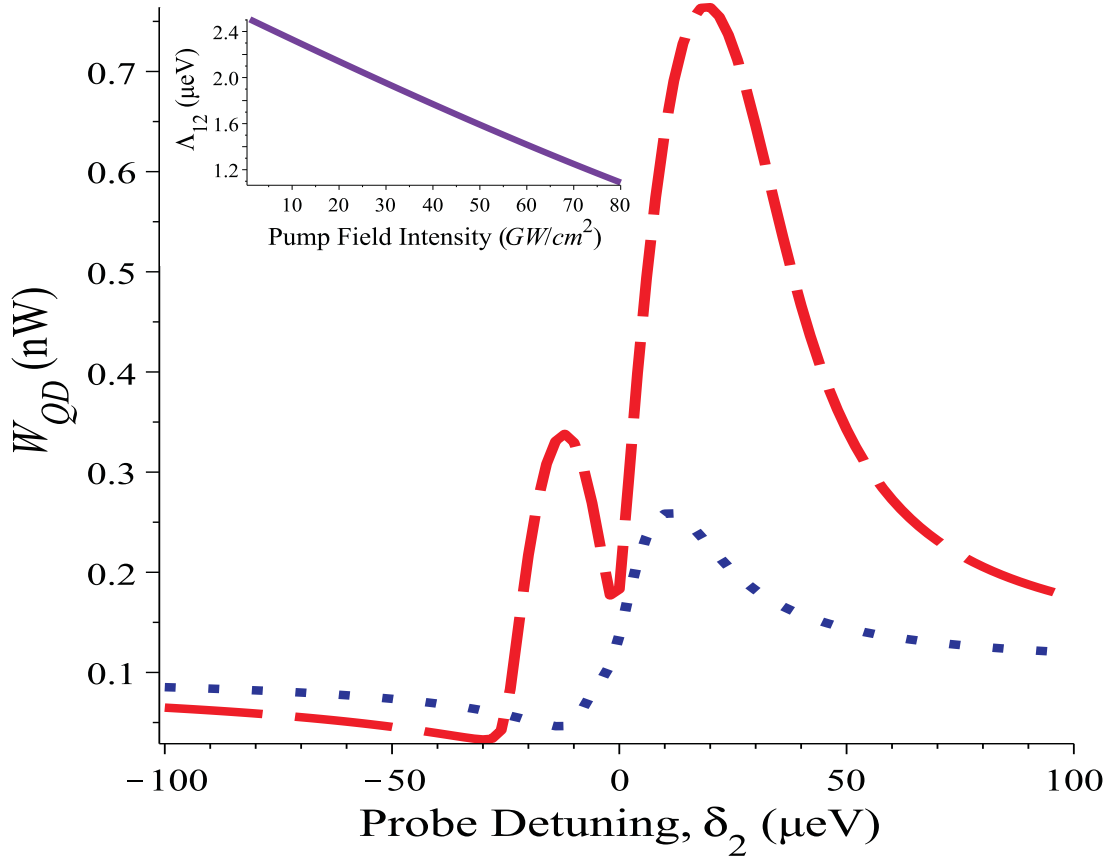


Figure 5.2: Power loss from the donor QD as a function of probe field detuning,  $\delta_2$ , for  $I_p = 0 \text{ GW/cm}^2$  (dashed curve) and  $I_p = 60 \text{ GW/cm}^2$  (dotted curve). Inset: DDI parameter is plotted as a function of  $I_p$ .

The power loss for the donor is plotted in figure 5.2 as a function of the probe detuning. The intensity of the probe field is  $I_2 = 80 \text{ W/cm}^2$  while the intensity of the control field is  $I_3 = 0.01 \text{ W/cm}^2$ . The control laser field is resonant with the excitonic transition  $|2\rangle \leftrightarrow |3\rangle$  (i.e.  $\delta_3 = 0 \mu\text{eV}$ ). The dashed and dotted curves are plotted for  $I_p = 0$  and  $I_p = 60 \text{ GW/cm}^2$ , respectively, where the distance between the acceptor and donor is  $R = 11 \text{ nm}$ . Note that the power loss has two peaks and a clear minimum near  $\delta_2 = 0 \mu\text{eV}$ . The observed splitting is due to the interference between the probe field  $E_2$  (i.e.  $\Omega_{12}$ ) and dipole field  $E_{ddi}^d$  (i.e.  $\Lambda_{12}\rho_{12}$ ). See equations (5.28) or (5.33). Note that in the presence of the pump field, the two peaks merge into one and the height and location of that peak changes (see dotted curve). This means the

power loss can be controlled by the pump field, due to the nonlinear photonic crystal. This is an interesting result and can be used to fabricate new types of all-optical switching devices and optical sensors.

The control of the power loss due to the nonlinear photonic crystal can be explained as follows. The pump field causes the refractive index of polystyrene to change due to the Kerr effect, i.e.  $n'_a = n_a + n_3 I_p$ , where  $I_p$  is the intensity of the pump field and the Kerr constant is  $n_3 = 1.15 \times 10^{-12} \text{ cm}^2/\text{W}$  for polystyrene. The change in the refractive index of polystyrene modifies  $\epsilon_{pc}$ , which in turn changes the DDI coupling  $\Lambda_{ij}$  (see equation (5.14)). We have plotted  $\Lambda_{12}$  as a function of  $I_p$  in the inset to figure 5.2. Note that as intensity increases, the DDI parameter decreases, and this in turn destroys the interference between the probe and dipole fields. This is why we get one peak, and a change in the height of that peak.

The PL efficiency is calculated as a function of  $R$  in figure 5.3. We have chosen the value of the probe detuning to be  $\delta = -10 \mu\text{eV}$  (see figure 5.2), where the interference plays an important role. Note that the efficiency spectrum has a peak at about  $R = 16 \text{ nm}$ . This peak is due to the interference between the probe and DDI fields. The peak appears, since the denominator of  $P_E$  in equation (5.32) has a smaller value, due to the interference past about  $R = 13 \text{ nm}$ , compared to the numerator. When we apply the pump field to the photonic crystal, the peak at  $R = 16 \text{ nm}$  disappears, and a new peak appears at a lower value of  $R = 11 \text{ nm}$  (see dotted curve). The height of the peak is also reduced. This is because the DDI parameter,  $\Lambda_{j\ell}$ , is decreased by the pump field, as we discussed before. This in turn decreases the DDI field and the interference between it and the probe field does not occur. When the distance between the acceptor and donor QDs is decreased, the DDI parameter increases. This increases the DDI field and the interference condition is again satisfied at a lower value, approximately  $R = 9 \text{ nm}$ . That is why we get a peak near  $R = 11 \text{ nm}$  in the presence of the pump field. We have also plotted  $P_E$  in the absence of the interference term, and in the absence and presence of the pump field inset in figure 5.3. It is found that the interference peak disappears and the efficiency increases with increasing  $R$ .

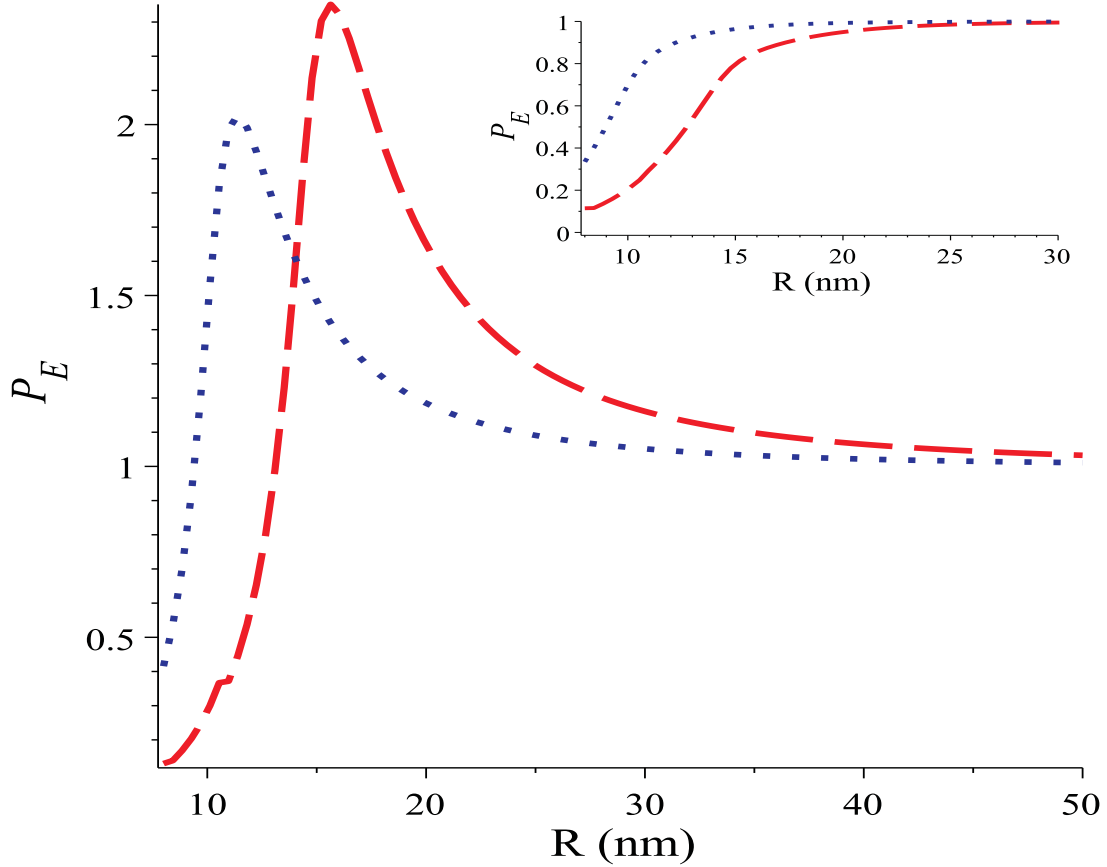


Figure 5.3: PL efficiency as a function of donor to acceptor QD separation,  $R$ , for  $I_p = 0$   $\text{GW}/\text{cm}^2$  (dashed curve) and  $I_p = 60$   $\text{GW}/\text{cm}^2$  (dotted curve). Inset: PL efficiency is plotted as a function of  $R$  in the absence of interference. Dashed and dotted curves represent  $I_p = 0$   $\text{GW}/\text{cm}^2$  and  $I_p = 60$   $\text{GW}/\text{cm}^2$ , respectively.

Our theory can also be applied to hybrid systems consisting of acceptor and donor QDs embedded in a dielectric medium such as aqua or quartz. This can be done by replacing the dielectric constant of the photonic crystal  $\epsilon_{pc}$  by the dielectric constant of that dielectric medium. We found a similar looking curve to the inset figure in figure 5.3, which shows the PL efficiency decreasing as  $R$  decreases. This means that the energy transported from the donor to the acceptor QD increases due to the DDI. This type of behavior has been observed by recent experiments [90], [91], [92]. Khatei et al. [90] have demonstrated electronic energy transfer between donor and acceptor CdTe QDs embedded in an aqueous media using steady-state PL spectroscopy, without using any external linker molecule. They found that

with an increasing concentration of larger QDs (donors), there is subsequent quenching of luminescence in smaller dots (acceptors) accompanied by the enhancement of luminescence in the larger dots.

Another group who considered a similar system was Higgins et al. [91]. They fabricated CdTe QDs embedded in an aqueous media. Their PL spectra and time-resolved PL decays show that there is a resonant energy transfer from the donor QD to the acceptor QD. They have also studied the concentration dependence of the donor QD on the energy transfer. They found that as the concentration increases, the PL efficiency decreases. Similar donor concentration dependence on the energy transfer between the donor and the acceptor QDs has also been investigated by Linz and Bradley [92]. The findings of this chapter are consistent with the above experiments. As the concentration of donors increases, the average distance  $R$  between the acceptor and donor will decrease. This, we show, decreases the PL efficiency.

## 5.7 Conclusion

In conclusion, we have calculated the ETR between donor and acceptor QDs embedded in a nonlinear photonic crystal. It is found that the energy can be transferred from the donor to the acceptor due to the DDI, and can be controlled by a pump field. This behaviour has been observed, and this mechanism suspected in the related publications, but this is the first time the effect was simulated with this level of detail, to the best of our knowledge. This present system can be used to fabricate nano-sensors, all optical nano-switches, energy transfer devices, and energy storage devices. The present formulation can also be used to study the energy transfer between the donor and acceptor chemical and biological molecules.

# Chapter 6

## The study of fluorescence in a quantum dot and metallic nanosphere hybrid system

In the previous chapter, energy transfer mechanisms between pairs of quantum dots were investigated. In this chapter, the fluorescence in quantum dots and a metallic nanosphere is considered, and power absorption is also calculated.

### 6.1 Introduction

In this chapter, we investigate energy absorption in quantum dots (QDs) which have been deposited on a dielectric medium. We also study the energy absorption when quantum dots and a metallic nanoparticle (MNP) are deposited on a substrate. These nanostructures are called a QD-MNP hybrid system. Recently, there has been considerable interest in the study of plasmonics in hybrid systems. Since plasmons tend to be far more localized than photons of the same energy, they can often mediate photon-excited information better than the photons

themselves. Experimental studies have shown efficient exciton-plasmon-photon conversion, so structures involving QDs and MNPs are rife with possibilities [54], [60], [61], [62].

Several hybrid systems have been considered for quantum information processing, and it has been demonstrated that entanglement survives the photon-plasmon-exciton conversion process [63], [64], [65]. Metal nanostructures have also been considered in constructing a two q-bit gate [65], [66]. The coupling between MNPs and QDs is sometimes enhanced through the use of a linker molecule, [67], [68], but efficient coupling can also occur without any interstitial matter [69], [70], [71]. MNPs have been used in conjunction with QDs in a variety of contexts [83], [142], [143], to enhance fluorescence in the QD [72], [73], [74], [75], to adjust the decay rates for the QD [76], to enhance the Fano effect [77], [78], as a pulse controller for a QD [74], or even to produce an electromagnetically induced transparency [51], [52], [79]. Nanorods, nanospheres, and even nanodiscs have been considered, [69], [73], [80], as well as multiple nanospheres [81].

The metallic nanoparticles considered in this chapter have a spherical shape. An ensemble of quantum dots are sitting near the metallic nanoparticle, on the same substrate. The concentration of quantum dots is taken to be small so that they do not interact with one another. The QDs used here have three excitonic states, namely the ground state and two successive excited states;  $|1\rangle$ ,  $|2\rangle$ , and  $|3\rangle$ . A probe laser is applied between the ground state and first excited state, to monitor the coupling between the QD and the metallic nanosphere (MNS). We have also applied a control laser between the two excited states. Induced dipoles are produced in the QD due to both the probe and control lasers, with dipole moments induced in the MNS as well. Given these dipole moments, the MNS and QD interact with each other via the dipole-dipole interaction (DDI). Surface plasmon-polaritons (SPPs) are also created in the MNS due to a coupling of charge fluctuations with the two laser fields. The polaritons have quantized states in the metallic sphere, since only certain modes of polaritons will propagate within the surface of the MNS. The quantized polaritons interact with excitons from the quantum dots.

This geometry is obviously similar to that presented in chapter 5. We have an MNS playing

the role of the acceptor QD, and there is a dielectric substrate rather than a photonic crystal, but the photonic crystal was modelled such that the dielectric function varied in frequency space, but not in real space, so those differences are less than one might think. The energy level structure for the QD is the same, but the interaction Hamiltonian is different.

The density matrix method has been used to evaluate power absorption from the laser fields in the hybrid system. Numerical simulations have been carried out, to derive power loss in the presence of the DDI and the exciton-SPP interaction. The power absorption spectrum of the QD was found to split from one peak into two peaks. This splitting can be accomplished either through increasing the intensity of the control field, or the DDI.

The fluorescence efficiency for quantum dots in this system has also been investigated. The fluorescence efficiency is defined as the ratio of the power absorbed by the QD in the absence of the MNS to the power absorbed in the presence of the MNS. The fluorescence efficiency was found to increase as the distance between the QD and the MNS increases. In summary, we found that the energy transfer between the QD and the MNS can be controlled by the control laser by changing the shape of the energy absorption spectrum. Therefore, the present system is one that could be used to fabricate new types of nanoscopic devices, such as ultrafast switching devices and sensing devices.

## 6.2 Quantum Dot embedded on a Dielectric Medium

The quantum system under investigation here is that of a QD lying on a dielectric medium, where the radius of the QD is  $r_d$ . When the QD is excited, it will produce an exciton, and we assume that the QD in question will efficiently transform energy between photons and excitons. We take a ladder-type three-level QD, meaning that, first of all, there are 3 states,  $|1\rangle$ ,  $|2\rangle$ , and  $|3\rangle$ ; where  $|1\rangle$  is the ground state, and  $|2\rangle$  and  $|3\rangle$  are excited states. The allowed transitions for a ladder-type QD are  $|1\rangle \leftrightarrow |2\rangle$  and  $|2\rangle \leftrightarrow |3\rangle$ , and their transition frequencies are  $\omega_{21}$  and  $\omega_{31}$ , respectively. A schematic diagram for QDs in this environment is shown in figure 6.1.

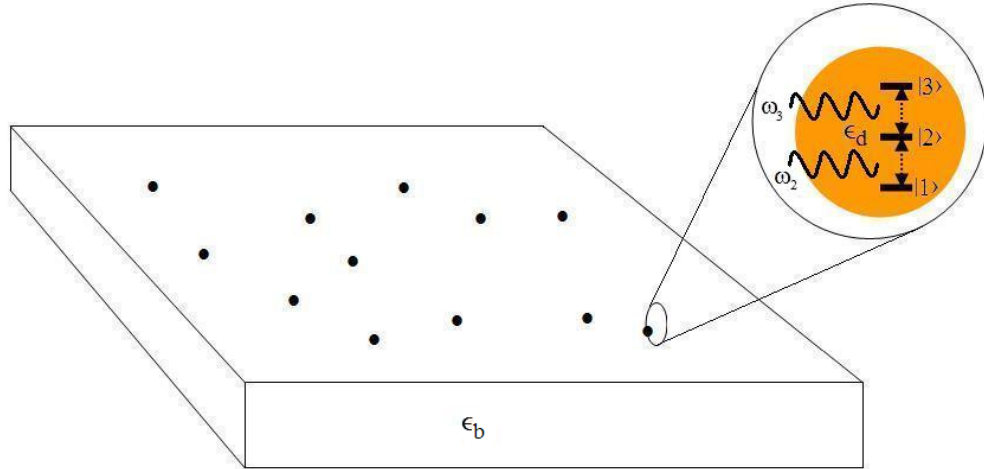


Figure 6.1: An ensemble of 3-level quantum dots deposited on a substrate. The black dots are QDs. The QD has three states,  $|1\rangle$ ,  $|2\rangle$ , and  $|3\rangle$ .

We refer to the applied external electric fields as the probe and control fields, with the probe field being,  $E_2 = E_2^0 \cos(\omega_2 t)$  with frequency  $\omega_2$  and amplitude  $E_2^0$ , which is applied between states  $|1\rangle$  and  $|2\rangle$ , and thereby an exciton is excited to state  $|2\rangle$ . Similarly, a control laser field, defined by  $E_3 = E_3^0 \cos(\omega_3 t)$ , with frequency  $\omega_3$  and amplitude  $E_3^0$ , is applied between states  $|2\rangle$  and  $|3\rangle$  and it will promote this exciton to state  $|3\rangle$ . The first exciton (from state  $|2\rangle$ ) must decay spontaneously to the ground state, since excitons will couple with the background radiation field. The other exciton can only decay to state  $|2\rangle$ , and one way to do that is through the background field. This is known as the radiative decay. Without the MNS in our formulation yet, this is almost exactly the setup of chapter 5, with a much smaller density of quantum dots.



### 6.3 External Electric Fields

The electric field felt by the QD is then:

$$E_d = \frac{E_2}{\epsilon_{dr}} e^{-i\omega_2 t} + \frac{E_3}{\epsilon_{dr}} e^{-i\omega_3 t} + cc \quad (6.1)$$

where:

$$\epsilon_{dr} = \frac{(2\epsilon_b + \epsilon_d)}{3\epsilon_b} \quad (6.2)$$

and  $cc$  stands for the complex conjugate. Also,  $\epsilon_b$  is the dielectric constant of the substrate dielectric, and  $\epsilon_d$  the dielectric constant of the QD. Next, we need to define Rabi frequencies for the probe and control fields, which are:

$$\Omega_2 = \frac{\mu_{12} E_2^0}{2\hbar \epsilon_{dr}} \quad (6.3a)$$

$$\Omega_3 = \frac{\mu_{23} E_3^0}{2\hbar \epsilon_{dr}} \quad (6.3b)$$

where  $\Omega_2$  and  $\Omega_3$  are the Rabi frequencies for the probe and the control laser fields, respectively. The Rabi frequencies relate to the intensities of the laser fields, since they contain the amplitudes of those fields. The  $\mu_{j\ell}$  term represents the transition dipole moment for the  $|j\rangle \leftrightarrow |\ell\rangle$  transition.

Finally, the electric field felt by the QD can be obtained by substituting equations (6.3a) and (6.3b) into equation (6.1) to yield:

$$E_d = \frac{\hbar}{\mu_{12}} (\Omega_{12}) e^{-i\omega_2 t} + \frac{\hbar}{\mu_{23}} (\Omega_{23}) e^{-i\omega_3 t} + cc \quad (6.4)$$

Note that the electric field in the vicinity of the QD has two sources. The first term comes from the probe field, and the other from the control field.

## 6.4 Interaction Hamiltonian

The power loss that occurs within the quantum dot requires that we know some of the density matrix elements, and they are found using the density matrix method [52]. The first thing we need for this treatment is the Hamiltonian. The Hamiltonian for an electron-hole pair in the quantum dot is then:

$$H_e = \hbar\omega_{21} (|2\rangle\langle 2| - |1\rangle\langle 1|) + \hbar\omega_{32} (|3\rangle\langle 3| - |2\rangle\langle 2|) \quad (6.5)$$

This is not the whole story. Two laser fields are applied to monitor absorption, so we need interaction terms between these fields and the QD, and we choose to add a term without considering multiple-photon processes. Therefore, when we apply the dipole approximation, and find the laser-quantum dot portion of the Hamiltonian in the interaction representation, we have:

$$H_{QD-L} = -\Omega_{12}e^{-i(\omega_2-\omega_{21})t}\sigma_{21}^+ - \Omega_{23}e^{-i(\omega_3-\omega_{32})t}\sigma_{32}^+ + hc \quad (6.6)$$

where  $hc$  stands for the Hermitian conjugate. This Hamiltonian so far does not allow for spontaneous emission yet, and we wish to allow decay into the background field of the substrate from state  $|3\rangle$  to  $|2\rangle$  to  $|1\rangle$ , successively. In other words, the dielectric material acts as a reservoir for the QD.

$$H_{QD-R} = -\sum_k g_{21}^0(\omega_k) p_k \sigma_{21}^+ e^{i(\omega_{21}-\omega_k)t} - \sum_k g_{32}^0(\omega_k) p_k \sigma_{32}^+ e^{i(\omega_{32}-\omega_k)t} + hc \quad (6.7)$$

where  $\sigma_{j\ell}^+ = |j\rangle\langle\ell|$  is called the creation operator for an exciton. Here,  $p_k$  is the lowering operator for photons in the substrate. Also,

$$g_{j,(j-1)}^0(\omega_k) = (\mathbf{e}_k \cdot \boldsymbol{\mu}_{j,(j-1)}) \sqrt{\frac{\hbar\omega_k}{2\epsilon_b V}} \quad (6.8)$$

where  $V$  is the quantization volume for the substrate. This means that the total Hamiltonian

of the system becomes:

$$H_{QD} = H_{QD} + H_{QD-L} + H_{QD-R} \quad (6.9)$$

## 6.5 Quantum Dot-Metallic Nanosphere Hybrid System

The system we now consider consists of a QD and an MNS sitting on a dielectric substrate, where the radius of a QD is  $r_d$  and the MNS has a radius of  $r_m$ . The center-to-center distance between the QD and the MNS is given as  $R$ . In the QD, optical excitations create excitons, with a sharp and discrete response. As before, the three excitonic states are denoted as  $|1\rangle$ ,  $|2\rangle$ , and  $|3\rangle$ ; where  $|1\rangle$  is the ground state and  $|2\rangle$  and  $|3\rangle$  are excited states. Excitons in the QD act as quantum emitters. That is, energy does not leave a QD except to create a photon or SPP, and the photons created must be from an exciton transition. The exciton transition frequencies between  $|1\rangle \leftrightarrow |2\rangle$  and  $|2\rangle \leftrightarrow |3\rangle$  are denoted as  $\omega_{12}$  and  $\omega_{23}$ , respectively. The localized surface plasmon frequency of the MNS is denoted as  $\omega_{sp}$ . A schematic diagram for this hybrid system is shown in figure 6.2.

For this model, the control field frequency,  $\omega_3$  lies near the localized surface plasmon frequency  $\omega_{sp}$ . In the presence of the probe and control laser fields, the induced dipoles are created in the QD and MNS, and they interact with each other via the dipole-dipole interaction (DDI). This interaction is very strong due to enhanced local fields in the vicinity of the MNS. The DDI also refers to Coulomb interactions over the length scales involved. This interaction leads to excitation transfer between the QD and the MNS. Again, the environment for the 2 nanoparticles here is a dielectric substrate.

The electric field felt by the QD is now written:

$$E_d = \frac{E_2}{\epsilon_{dr}} + \frac{E_3}{\epsilon_{dr}} + \frac{S_r P_m}{(4\pi\epsilon_b)\epsilon_{dr}R^3} \quad (6.10)$$

where  $\epsilon_{dr} = (2\epsilon_b + \epsilon_d)/3\epsilon_b$ , as before. Here,  $S_r$  is called the polarization parameter with  $S_r = 2$  [79]. The first and second terms in the above expression are electric fields which

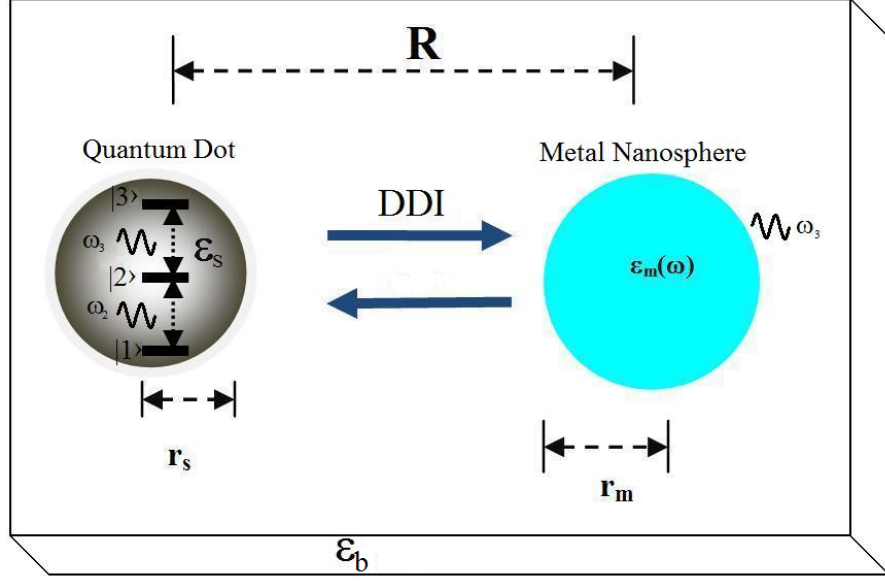


Figure 6.2: A 3-level quantum dot with a nearby metallic sphere and two external fields applied to this system. The probe field,  $\omega_2$  excites the ground state of the quantum dot and the control field,  $\omega_3$  drives the metal sphere at its resonance frequency while exciting the quantum dot to the uppermost level. The dipole-dipole interaction (DDI) couples the metal nanosphere to the quantum dot. The complete system would consist of an ensemble of quantum dots interacting with a metal nanosphere atop a dielectric substrate.

represent the probe and control laser fields, respectively. The last term is the dipole electric field created by the total induced polarization,  $P_m$  in MNS from the probe and control fields.

Similarly, the total electric field  $E_m$  felt by the MNS would be:

$$E_m = \frac{E_2}{\epsilon_{mr}} + \frac{E_3}{\epsilon_{mr}} + \frac{S_r [\mu_{23}\rho_{23} + \mu_{23}^*\rho_{32}]}{(4\pi\epsilon_b)\epsilon_{mr}R^3} \quad (6.11)$$

$$\epsilon_{mr} = \frac{2\epsilon_b + \epsilon_m(\omega)}{3\epsilon_b} \quad (6.12)$$

where  $\mu_{j\ell}$  and  $\rho_{j\ell}$  are the dipole moment and density matrix elements for the transition  $|j\rangle \leftrightarrow |\ell\rangle$ . The third term in the above equation is the dipole electric field arising from the QD and

owing to the control field. Note that equation (6.10) and equation (6.11) are self-consistent and inter-related. The electric field  $E_m$  creates a polarization  $P_m$  in the MNS and it is obtained by:  $P_m = \alpha_m E_m$ , where  $\alpha_m$  is called polarizability, and is written [83]:

$$\alpha_m = \frac{4\epsilon_0\pi r_m^3 (\epsilon_m(\omega) - \epsilon_b)}{\epsilon_m(\omega) + 2\epsilon_b} \quad (6.13)$$

where  $\epsilon_m(\omega)$  is the dielectric constant of the MNS and is written as:

$$\epsilon_m(\omega) = \epsilon_\infty - \frac{\omega_p^2}{\omega^2 - i\kappa\omega} \quad (6.14)$$

where  $\omega_p$  is the plasma frequency and  $\kappa$  is the relaxation rate for electrons. Substituting equation (6.13) and equation (6.11) into  $P_m = \alpha_m E_m$  and defining:

$$\rho_{12} = \rho'_{12} e^{-i\omega_2 t} \quad (6.15)$$

$$\rho_{23} = \rho'_{23} e^{-i\omega_3 t} \quad (6.16)$$

we can obtain an expression for the polarization,  $P_m$  where:

$$P_m = 4\pi\epsilon_b r_m^3 \left[ \frac{\gamma}{\epsilon_{mr}} \left( \frac{E_3^0}{2} + \frac{1}{(4\pi\epsilon_b)} \frac{S_r \mu_{23} \rho'_{23}}{R^3} \right) e^{-i\omega_3 t} \right] + cc \quad (6.17)$$

where  $cc$  stands for the complex conjugate and  $\gamma$  is expressed as:

$$\gamma = \frac{\epsilon_m(\omega) - \epsilon_b}{\epsilon_m(\omega) + 2\epsilon_b} \quad (6.18)$$

Note that we have assumed that  $\omega_2$  is too low energy to polarize the MNS effectively, whereas  $\omega_3$  drives the MNS at resonance.

Finally, the electric field felt by the QD is obtained by substituting equation (6.17) into equation (6.10) yielding:

$$E_d = \frac{\hbar}{\mu_{12}} \Omega_{12} e^{-i\omega_2 t} + \frac{\hbar}{\mu_{23}} (\Omega_{23} + \Pi_3 + \Lambda_3) e^{-i\omega_3 t} \quad (6.19)$$

where:

$$\Omega_{12} = \frac{\mu_{12}E_2^0}{2\hbar\epsilon_{dr}} \quad (6.20)$$

$$\Omega_{23} = \frac{\mu_{23}E_3^0}{2\hbar\epsilon_{dr}} \quad (6.21)$$

$$\Pi_3 = \left( \frac{r_m^3 \gamma S_r}{\epsilon_{dr} R^3} \right) \Omega_{23} \quad (6.22)$$

$$\Lambda_3 = \frac{\gamma r_m^3 S_r^2 \mu_{23}^2 \rho'_{32}}{(4\pi\epsilon_b) \hbar\epsilon_{dr} R^6} \quad (6.23)$$

Note that the electric field felt by the quantum dot contains three contributions. The first term is the direct contribution from the control field. The second term is the dipole field from the MNS which the control field induces. The third term arises when the control field polarizes the QD, which then polarizes the MNS. The MNS, in turn, produces the third term to interact with the QD. Therefore, this term represents the self-interaction of the QD, because this term originates from the polarization of the QD. We call this term the dipole-dipole interaction (DDI) term which depends on both QD and MNS parameters.

In the previous section, the Hamiltonian was derived without a metal sphere. The Hamiltonian for excitons in the QD must have a DDI term added in. That term is:

$$H_{DDI} = (\Omega_{23} + \Pi_3 + \Lambda_3) e^{-i(\omega_3 - \omega_{32})t} \sigma_{32}^+ \quad (6.24)$$

We require that the excited states  $|2\rangle$  and  $|3\rangle$  decay spontaneously to the state directly below them due to coupling with the background radiation field, and state  $|3\rangle$  can also decay through interaction with an SPP. In other words, the MNS acts as a reservoir for the QD. The QD also interacts with the probe field, the control laser field, and the fields from induced dipoles in the MNS. Therefore, the total Hamiltonian of the QD is expressed as above in the dipole approximation and in the interaction representation. In the previous Hamiltonian, equation

(6.9) only allows for photons to decay into the substrate. To allow for the creation of plasmon-polaritons, through the decay of excitons as well as through the DDI, terms would need to be added to the Hamiltonian. For the new terms  $p_k^d$  would be the lowering operator for plasmon-polaritons. We introduce  $g_{32}^d(\omega_k)$  as the coupling constant for SPPs, given by:

$$g_{32}^d(\omega_k) = \sqrt{\left(\frac{\hbar\omega_k}{2\epsilon_b(\pi r_m^3)}\right)} \left(1 + \frac{\gamma S_r(\pi r_m^3)}{\epsilon_{dr} R^3}\right) (\mathbf{e}_k \cdot \boldsymbol{\mu}_{32}) \quad (6.25)$$

where  $\mathbf{e}_k$  is the polarization of the plasmon-polaritons. The terms  $\omega_k$  and  $k$  are the frequency and the wave vector for plasmon-polaritons, respectively. The first term in equation (6.24) corresponds to the coupling of excitons to the control field, the second term is the coupling Hamiltonian between the QD and the MNS, and the last term refers to self-interaction for the QD. In chapter 5, we had DDI terms for both QD transitions, but there was only a term like  $\Lambda_3$ , which means the Hamiltonian contains  $\rho_{32}\sigma_{32}^+$ . Here we also have the Rabi intensity dependent on MNS parameters, something that did not appear in chapter 5.

We wish to couple the  $|2\rangle \leftrightarrow |3\rangle$  transition with the MNS, which means we need to know what energy the MNS will resonate with, and the QD will then have that energy for its  $|2\rangle \leftrightarrow |3\rangle$  transition. We evaluate this relation by using the following model. The polarizability  $\alpha_m$  of the MNS has been obtained in equation (6.13). Plasmon-polariton resonances occur at frequencies when  $\alpha_m$  has a singularity. This means that for resonance,  $\epsilon_m(\omega) + 2\epsilon_b = 0$ , so an analytical expression for the localized surface plasmon resonance can be obtained if we use the Drude model for  $\epsilon_m$ . We found the following expression of the plasmon-polariton resonance:

$$\omega_{sp} = \sqrt{\frac{\omega_p^2}{\epsilon_\infty + 2\epsilon_b}} \quad (6.26)$$

where  $\omega_p$  is the plasmon frequency. This will be the frequency for the  $|2\rangle \leftrightarrow |3\rangle$  transition.

## 6.6 Density Matrix Formulation

We use the density matrix method to evaluate the power loss in the QD and the MNS. Using

equations (6.10-6.25), we obtained the following expression for density matrix elements:

$$\begin{aligned}
\frac{d\rho_{11}}{d\tau} &= 2\Gamma_{21}\rho_{22} + i\Omega_{12}\rho_{12} - i\Omega_{12}^*\rho_{21} & (6.27) \\
\frac{d\rho_{33}}{d\tau} &= -2(\Gamma_{32} + \Gamma_3)\rho_{33} - i(\Omega_{23} + \Pi_3 + \Lambda_3\rho_{32})\rho_{23} + i(\Omega_{23}^* + \Pi_3^* + \Lambda_3^*\rho_{23})\rho_{32} \\
\frac{d\rho_{32}}{d\tau} &= -(\Gamma_{32} + \Gamma_{21} - i(\delta_{23} + \Delta_3))\rho_{32} + i\Omega_{12}^*\rho_{31} + i(\Omega_{23} + \Pi_3 + \Lambda_3\rho_{32})(\rho_{33} - \rho_{22}) \\
\frac{d\rho_{21}}{d\tau} &= -[\Gamma_{21} - i\delta_{12}]\rho_{21} + i\Omega_{12}(\rho_{22} - \rho_{11}) - i(\Omega_{23}^* + \Pi_3^* + \Lambda_3^*\rho_{23})\rho_{31} \\
\frac{d\rho_{31}}{d\tau} &= -[(\Gamma_{32} + \Gamma_3) + \Gamma_{21} - i\delta_{12} - i\delta_{23}]\rho_{31} + i\Omega_{12}\rho_{32} - i(\Omega_{23} + \Pi_3 + \Lambda_3\rho_{32})\rho_{21}
\end{aligned}$$

In the above expression  $\Delta_3$  and  $\Gamma_3$  are the nonradiative energy shift and decay rate due to the dipole-dipole interaction term  $\Lambda_3$ .

$$\Delta_3 = \text{Re} [\Lambda_3 (\rho_{22} - \rho_{33})] \quad (6.28)$$

$$\Gamma_3 = \text{Im} [\Lambda_3 (\rho_{22} - \rho_{33})] \quad (6.29)$$

Also,  $\Gamma_{21}$  and  $\Gamma_{32}$  are the spontaneous decay rates for the excited states  $|2\rangle$  and  $|3\rangle$ , respectively, due to the background radiation field and the plasmon-polaritons.

## 6.7 Power Absorption and Fluorescence efficiency

Energy loss from the quantum dots in this system arises because excitons decay in the quantum dot, which transfers the energy of those excitons to the MNS. Power loss which occurs in the QD is denoted as  $W_d$  and is found to be:

$$W_d = \hbar\omega_{21}\rho_{22}\Gamma_{21} + \hbar\omega_{32}\rho_{33}\Gamma_{32} \quad (6.30)$$

where  $\Gamma_{21}$  and  $\Gamma_{32}$  are decay rates for the excited states  $|2\rangle$  and  $|3\rangle$  to their respective unexcited states. Note that the power loss we are interested in (for the QD) depends on the decay rates



and the populations of excitons in  $|2\rangle$  and  $|3\rangle$ . We model these populations through the density matrix elements,  $\rho_{22}$  and  $\rho_{33}$  for the QD.

The energy transfer from the QD to the MNS is generally measured experimentally from a fluorescence emission measurement of the QD. When energy transfer occurs, the QD's fluorescence intensity will decrease. The energy transfer efficiency  $W_E^d$  is defined as the relative change in the QD's fluorescence emission:

$$W_E^d = \frac{W_d^0}{W_d^0 + W_d^{ddi}} \quad (6.31)$$

## 6.8 Results and Discussion

We wish to investigate power loss from the external fields due to a quantum dot with a metallic nanosphere nearby. In order to investigate this, we take a CdSe quantum dot with parameters  $\epsilon_d = 10$ ,  $\hbar\omega_{12} = 0.5$  eV,  $\mu_{12} = 0.7$  e nm,  $\mu_{23} = 0.8$  e nm, [144]  $\hbar\omega_{23} = 2.36$  eV,  $\Gamma_{21} = 0.6$  ns<sup>-1</sup>,  $\Gamma_{32} = 2$  ns<sup>-1</sup> [145]. For the metal nanoparticle, we take a gold sphere with parameters  $r_m = 9$  nm and  $\omega_p = 9$  eV, and we assume it is resonant with the  $|2\rangle \leftrightarrow |3\rangle$  transition in the quantum dot (QD). The background material on which we place this system is taken to be silica with  $\epsilon_b = 2.25$ . For this gold MNS, we take  $\epsilon_\infty = 10$ , which means  $\hbar\omega_{sp} = 2.36$  eV, [83] so our resonance condition is satisfied. We set the probe field to an intensity of  $I_p = 50$  W/m<sup>2</sup>, and the control field detuning was set to zero. All other parameters were allowed to vary according to what was being plotted.

The first effect we wish to investigate is the effect of the intensity of the control field. Figure 6.3 shows the power loss which occurs in the QD,  $W_d$ , being plotted against the probe field detuning,  $\delta_{12} = \omega_2 - \omega_{12}$ , from the density matrix equations (6.27). In the first (solid and orange) curve, the control field intensity was set to  $I_c = 0$  W/cm<sup>2</sup>. In the absence of the control field, the spectrum has one peak. This is due to the absorption of an exciton from state  $|1\rangle$  to  $|2\rangle$ , which the probe field is responsible for. There is no absorption due to the control field

when the control field is turned off. The control field is added for the gray dotted curve, and we chose an intensity of  $I_c = 40 \text{ W/cm}^2$ . In this case there is absorption due to the control field, as can be seen from the fact that the peak height increases. Another feature of this curve is that the single peak has split into two peaks. One could understand this in terms of dressed states, where the intensity from the control field at the QD causes the  $|2\rangle$  energy level to split into two states,  $|2_+\rangle$  and  $|2_-\rangle$ . Therefore, the spectrum has two peaks due to the transitions  $|1\rangle \rightarrow |2_+\rangle$  and  $|1\rangle \rightarrow |2_-\rangle$ . For the third curve (dashed and blue) the intensity was set to  $I_c = 800 \text{ W/cm}^2$ , and here we notice that there is virtually no power loss in the QD at zero detuning. Thus, the intensity of the control field has removed any absorption in the QD at the point in frequency where a less intense beam absorbs most strongly. This effect is known as electromagnetically induced transparency (EIT) and it is the basis for all-optical switching techniques.

In figure 6.4, we investigated DDI effects. For a weak control field, we took an intensity of  $I_c = 2 \text{ W/cm}^2$ , and we set the distance between the QD and the MNS to be  $R = 11 \text{ nm}$ . In figure 6.4,  $W_d$  is plotted against the probe field detuning. In the absence of the metal sphere, and hence the absence of DDI, these external fields lead to a single peak in the absorption spectrum for the quantum dot, at zero probe detuning. This is seen in the solid, orange curve, showing no DDI effects.

First we consider the DDI with only the  $\Pi_3$  term, and we find the gray dotted curve. In this curve, the peak has split into two peaks, which can be understood in terms of dressed states. In this case, the DDI term increases the intensity from the control field felt by the QD. For the  $\Pi_3$  term, this arises from the polarization of the MNS, polarized directly by the control field. This net intensity causes the  $|2\rangle$  energy level to split into two states,  $|2_+\rangle$  and  $|2_-\rangle$ . While this splitting as shown does not open up a transparent state in the middle, the peaks have split. Additional splitting from another source could open up a completely transparent state.

The blue dashed curve in figure 6.4 is plotted when both the  $\Pi_3$  and  $\Lambda_3$  terms are included. The  $\Lambda_3$  term adds asymmetry to the peaks, so that the peak locations are shifted, and no longer have the same height. These terms represent self-interaction in the QD, since they arise from

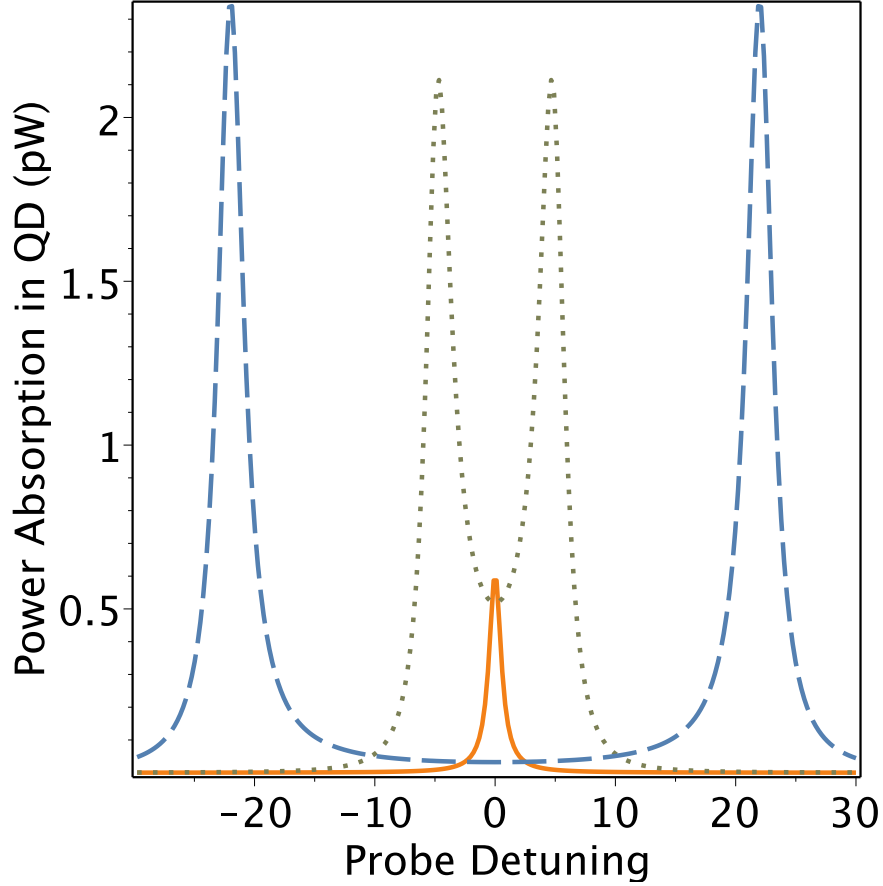


Figure 6.3: Power Absorption due to the quantum dot as a function of probe detuning, plotted in  $\text{ns}^{-1}$ . The solid curve has no MNS, and  $I_c = 0 \text{ W/m}^2$ , the dotted curve has no MNS, and  $I_c = 40 \text{ W/cm}^2$ , the dashed curve also has no MNS, and  $I_c = 800 \text{ W/cm}^2$ .

a dipole field induced by the control field in the QD, which couples to the MNS, which in turn produces a field that can be felt in the QD. This results in additional dynamical detuning, whereby the field returning to the QD has a slightly different frequency than the control field itself.

The next effect under consideration is the distance between the MNS and the QD. For figure 6.5, we again show  $W_d$  vs.  $\delta_p$ , with  $I_c = 2 \text{ W/cm}^2$ . The solid, dotted, and dashed curves are plotted for  $R = 11 \text{ nm}$ ,  $14 \text{ nm}$ , and  $50 \text{ nm}$ , respectively. In the dashed and blue curve, we take  $R = 50 \text{ nm}$ , and we recover the single peak in figure 6.4. At this distance, DDI effects are so weak that they can no longer overcome the broadening effects inherent in this QD. The splitting here is for the same reasons as splitting showed up in figures 6.3 and 6.4, where state

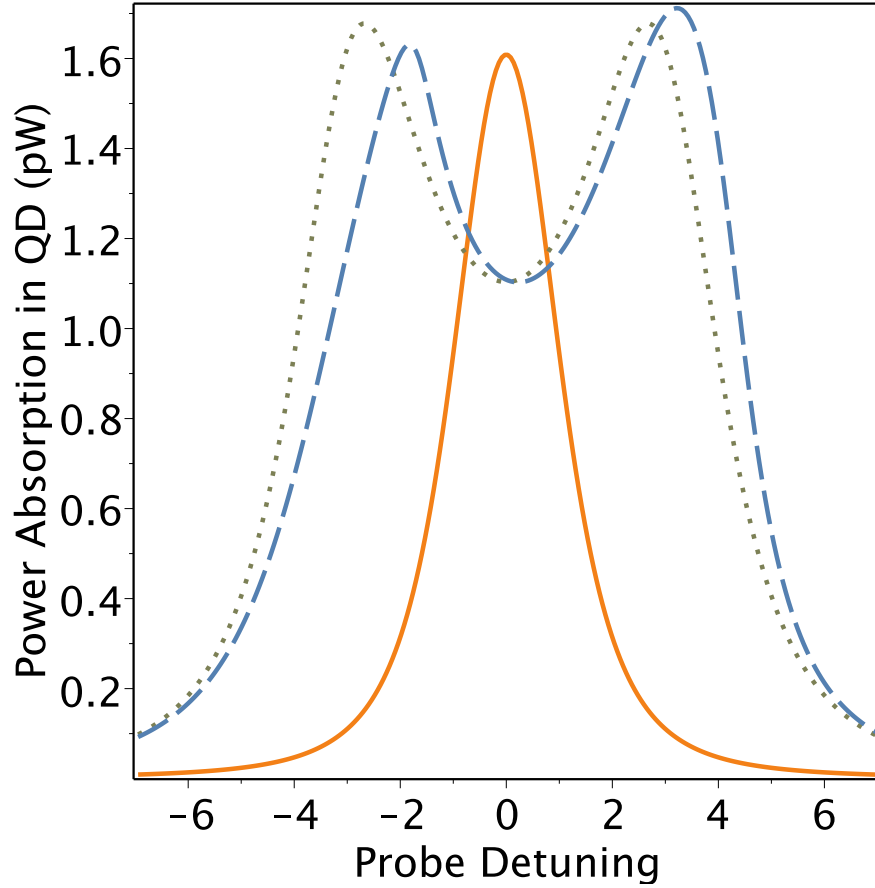


Figure 6.4: Power Absorption due to the quantum dot as a function of probe detuning, plotted in  $\text{ns}^{-1}$ . The solid curve has no MNS, the dotted curve has an MNS, but only with the  $\Pi_3$  component of the dipole-dipole interaction. The dashed curve has the full dipole-dipole interaction, including the  $\Lambda_3$  term.

$|2\rangle$  has split.

Lastly, we wish to look more in-depth at the distance between the QD and the MNS, so in figure 6.6, we plotted power absorption vs.  $R$  directly. In doing this, we set  $I_c = 10 \text{ W/cm}^2$ , and  $\delta_p = 8 \text{ ns}^{-1}$ , and the control field detuning was still zero. Power absorption in the QD was plotted with, and without DDI effects. Note that without the DDI (the orange and solid curve), power loss does not depend on distance. We expect this, on the basis that the DDI effects are the only things coupling the MNS to the QD. Note that as  $R$  increases, power absorption decreases. This is consistent with the findings of figure 6.5. Also note that with the DDI (gray and dotted curve) the power loss drops more dramatically than we saw in figure

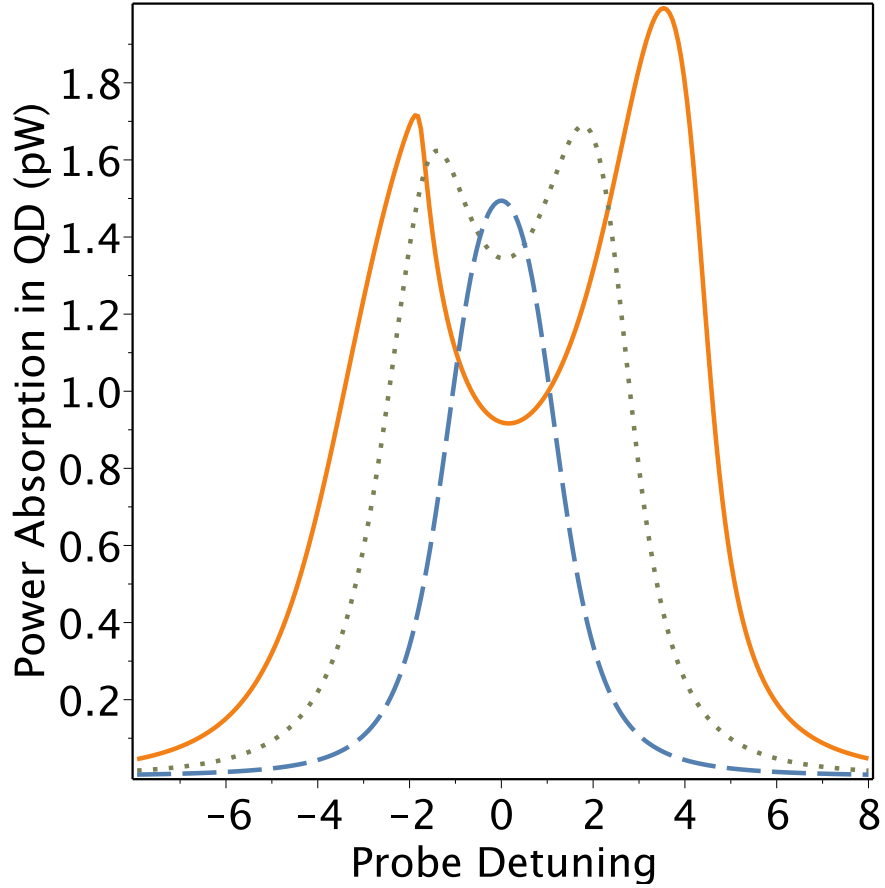


Figure 6.5: Power Absorption due to the quantum dot as a function of probe detuning, plotted in  $\text{ns}^{-1}$ . The solid, dotted and dashed curves are plotted for  $R = 11$  nm, 14 nm, and 50 nm, respectively.

6.5. This can be accounted for in 2 ways. First, the intensity is greater here, so the  $\Pi_3$  term, which drops off as  $1/R^3$ , will drop away faster, and the  $\Lambda_3$  term, which drops off as  $1/R^6$ , plays a more significant role at the shorter distances, where they also drop away more quickly.

In figure 6.7, the fluorescence efficiency for the quantum dot, as defined above, is plotted against the QD-MNS distance. Here we included a larger range of distances, so as to show the long-distance limit clearly. When  $R$  is large, the fluorescence efficiency becomes one. This shows the effect of the MNS. As  $R$  decreases, the efficiency decreases. This effect is called fluorescence quenching. This means that the fluorescence decreases in the QD due to

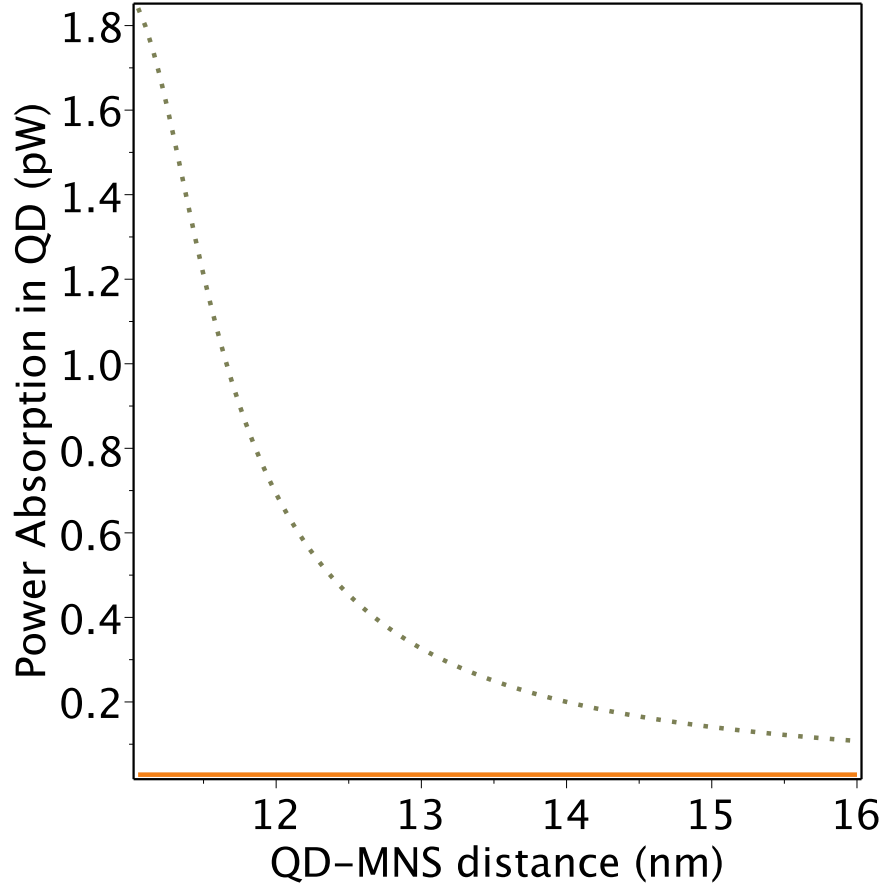


Figure 6.6: Power Absorption due to the quantum dot as a function of the distance between the quantum dot and metal sphere. The solid curve shows power loss without DDI effects, and the dotted curve shows the power loss with DDI effects. Note that the solid curve has a constant value of 0.028 pW.

the presence of the MNS. This has been measured experimentally [146].

## 6.9 Conclusion

In summary, power absorption from a laser field in quantum dots has been investigated, in particular when there is a metal sphere nearby. When there is no metal sphere present, or when it is very far from the quantum dot, there is a single absorption peak. As these two move closer together, this single peak is split into two peaks. This splitting results from the DDI between the QD and the MNS. This splitting can also be accomplished by increasing the intensity of the control field,  $I_c$ . The difference between these two types of splitting being

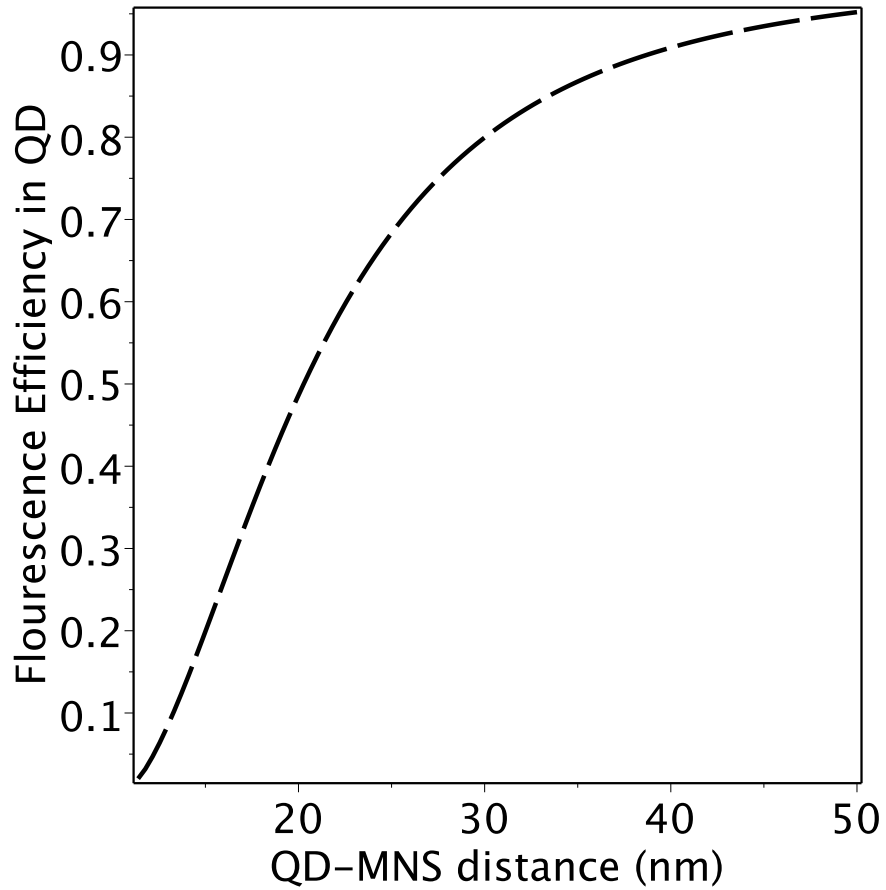


Figure 6.7: Fluorescence Efficiency in the quantum dot as a function of the distance between the quantum dot and the metal sphere.

that a metal sphere also shifts the locations of the peaks, introducing an asymmetry. Finally, the fluorescence efficiency for the quantum dot has also been investigated. The fluorescence efficiency can be quenched almost completely when the MNS is in close proximity to the QD. Either of these effects could be used as a photonic switch in photonic applications.

# Chapter 7

## Dipole-dipole interaction in a quantum dot and metallic nanorod hybrid system<sup>1</sup>

In the previous chapter, interactions between a quantum dot and a metallic sphere were discussed. In this chapter, a metallic nanorod is investigated, interacting with quantum dots. Energy transfer rates are calculated.

### 7.1 Introduction

Systems of nanoparticles have garnered much attention for their ability to tailor interactions between photons and electrons. Recently, considerable interest in coupled quantum dot (QD)-metal nanoparticle hybrid systems has arisen [51], [76], [78], [82], [83], [84], [85], [86], [87], [88]. For example, in references [51] and [78], the authors have studied the effects of weak and strong exciton-plasmon coupling regimes on the power absorption in a QD-metallic nanoparticle system. A three-level QD in the ladder-type [83] and V-type configurations [84], [85], [86], and [87] interacting with a metallic nanoparticle has also been studied in the presence of

---

<sup>1</sup>Reprinted with permission from M. R. Singh, D. Schindel, and A. Hatef, Applied Physics Letters, vol. 99, p. 181106, (2011). Copyright 2011, American Institute of Physics.



two external laser fields. Other hybrid systems such as a QD coupled with a metallic nanorod (MNR) [76] and a metal-dielectric nanoshell [88] have also been investigated.

One area of ongoing interest is the need for fast optical switching mechanisms. We study the interactions between optical excitations in a quantum dot (QD) and in a metallic nanorod, (MNR) and look for transparent states which can be switched on or off. Optical excitations in quantum dots are excitons, and in the MNR are called localized surface plasmons. The surface plasmon-polaritons (SPPs) arise from coupling of light with localized surface plasmons in the MNR. Interactions between excitons and SPPs occur when a MNR and a QD are in close proximity. In this hybrid system, the optical excitation frequencies of the two constituents are resonant with one another.

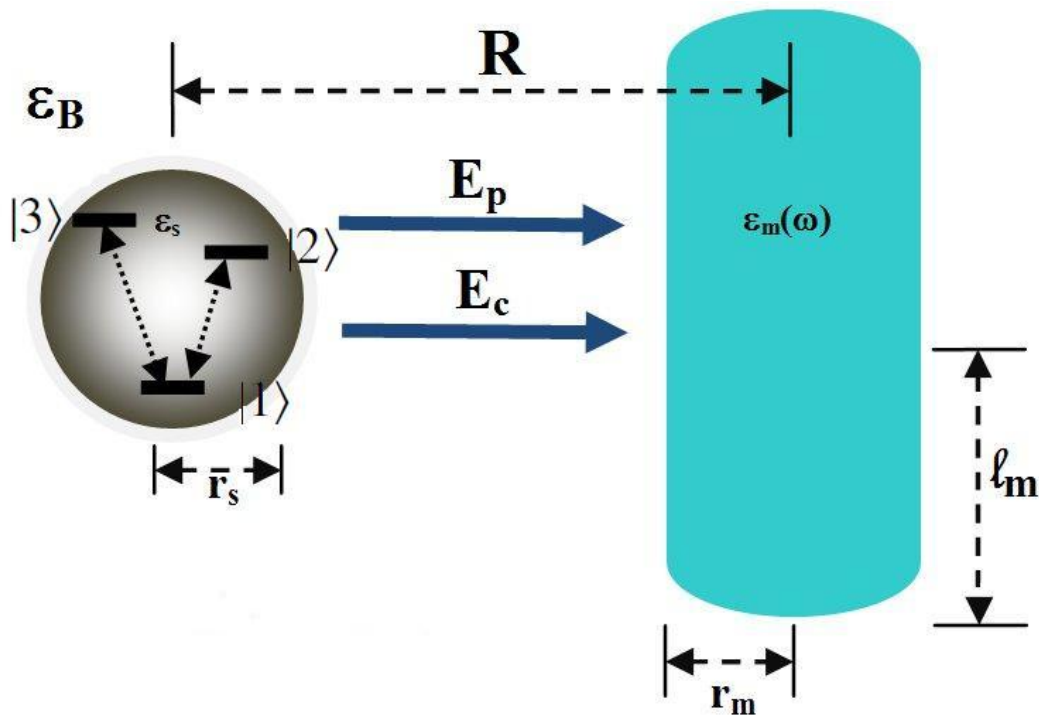


Figure 7.1: A schematic diagram of the quantum dot and metallic nanorod.

## 7.2 Exciton-plasmon coupling

In this chapter we investigate quantum coherence and interference phenomena in a QD-MNR hybrid system. The MNR has a cylindrical shape and has a radius  $r_m$  and length  $2l_m$  (figure 7.1). The center-to-center distance between the QD and the MNR is denoted as  $R$ . The three excitonic states are denoted as  $|1\rangle$ ,  $|2\rangle$ , and  $|3\rangle$ , where  $|1\rangle$  is the ground state, and  $|2\rangle$  and  $|3\rangle$  are the excited states. The exciton frequency of transition between  $|1\rangle \leftrightarrow |2\rangle$  and  $|1\rangle \leftrightarrow |3\rangle$  are denoted as  $\omega_{21}$  and  $\omega_{31}$ , respectively.

The two single-exciton states  $|1\rangle \leftrightarrow |2\rangle$  and  $|1\rangle \leftrightarrow |3\rangle$  are orthogonal linearly-polarized states, and are usually denoted as  $|x\rangle$  and  $|y\rangle$  states [147], or left and right circularly polarized exciton states [148]. Therefore, the probe and control laser fields have orthogonal polarizations. The present work uses left- and right-polarized states. A probe field  $E_2 = E_2^0 \cos(\omega_2 t)$  with frequency  $\omega_2$  and amplitude  $E_2^0$  is applied between  $|1\rangle$  and  $|2\rangle$  so that an exciton is excited to state  $|2\rangle$ . Similarly, a control laser field  $E_3 = E_3^0 \cos(\omega_3 t)$  with frequency  $\omega_3$  and amplitude  $E_3^0$  is applied between  $|1\rangle$  and  $|3\rangle$ , and a second exciton is excited to state  $|3\rangle$ . The probe and control fields lie perpendicular to, and along the direction of the MNR, respectively.

Induced dipole moments are created in the QD and the metallic nanorod, (MNR) and they interact with each other via the dipole-dipole interaction (DDI). Excited excitons will decay spontaneously to the ground state due to excitons coupling with the background radiation field and exciton-SPP coupling. In other words, the MNR acts as a reservoir for the QD. The wave vector for SPPs has two components;  $\mathbf{k}_n$  and  $\mathbf{k}$ , where  $\mathbf{k}_n$  is the chiral wave vector (circumference wave vector) and  $\mathbf{k}$  is the wave vector along the length of the MNR. The chiral wave vector is quantized so that  $2\pi r_m k_n = 2\pi n$ , where  $n$  is a quantum number with  $n = 1, 2, 3$ , etc. This system is very similar to that presented in chapter 6, the quantum dot structure is different, and the rod was a sphere, but the only other difference is that the MNP interacts with both transitions here, rather than just the  $|2\rangle \leftrightarrow |3\rangle$  transition in chapter 6.

The total Hamiltonian for the QD is given here. We use the dipole approximation and the

interaction representation to derive this Hamiltonian:

$$H_{QD} = \sum_{j=2,3} [H_e + H_E + H_{QR}] + hc \quad (7.1a)$$

where:

$$H_e = \hbar\omega_{j1}\sigma_{j1}^z \quad (7.1b)$$

$$H_E = -(\Omega_{1j} + \Lambda_j\rho_{j1})e^{-i(\omega_j-\omega_{j1})t}\sigma_{j1}^+ \quad (7.1c)$$

$$H_{QR} = -\sum_{nk} (g_{j1}^0 + g_{j1}^d) p_{nk}\sigma_{j1}^+ e^{i(\omega_{j1}-\omega_{nk})t} \quad (7.1d)$$

where:

$$g_{j1}^0(\omega_k) = (\mathbf{e}_k \cdot \boldsymbol{\mu}_{j1}) \sqrt{\frac{\hbar\omega_k}{2\epsilon_b(r_m^2 l_m)}} \quad (7.2a)$$

$$g_{j1}^d(\omega_k) = \frac{\gamma_{r,l} S_{r,l} r_m^2 l_m g_{j1}^0(\omega_k)}{\epsilon_{dr} R^3} \quad (7.2b)$$

$$\Omega_{1j}^0 = \frac{\mu_{1j} E_j^0}{2\hbar\epsilon_{dr}} \quad (7.3a)$$

$$\Omega_{1j} = \Omega_{1j}^0 + \frac{l_m r_m^2 \gamma_{r,l} S_{r,l} \Omega_{1j}^0}{R^3} \quad (7.3b)$$

$$\Lambda_j = \frac{\gamma_{r,l} l_m r_m^2 S_{r,l} \mu_{1j}^2}{(4\pi\epsilon_b) \hbar\epsilon_{dr}^2 R^6} \quad (7.4)$$

$$\epsilon_{dr} = \frac{(2\epsilon_b + \epsilon_d)}{3\epsilon_b} \quad (7.5)$$

$$\gamma_{r,l} = \frac{[\epsilon_m(\omega) - \epsilon_b]}{[3\epsilon_b + 3\zeta_{r,l}(\epsilon_m(\omega) - \epsilon_b)]} \quad (7.6)$$

$$\zeta_l = \frac{1 - e_m^2}{e_m^2} \left[ \frac{1}{2e_m} \ln\left(\frac{1 + e_m}{1 - e_m}\right) - 1 \right] \quad (7.7a)$$

$$\zeta_r = \frac{(1 - \zeta_l)}{2} \quad (7.7b)$$

$$e_m = \sqrt{1 - \left(\frac{r_m}{l_m}\right)^2} \quad (7.8)$$

Also,  $hc$  stands for the Hermitian conjugate,  $\sigma_{j1}^+ = |j\rangle\langle 1|$  is the creation operator responsible for excitons, and  $\sigma_{j1}^- = |j\rangle\langle j| - |1\rangle\langle 1|$  denotes the current state of the excitons. Here,  $p_{nk}$  is the lowering operator for plasmon-polaritons. The subscripts  $l$  and  $r$  stand for an electric field applied along the length or radial directions of the MNR, respectively. Here,  $\epsilon_b$  is the dielectric constant of the host dielectric material,  $\epsilon_d$  the dielectric constant of the QD,  $\mathbf{e}_k$  is the polarization vector,  $S_{r,l}$  is called the polarization parameter with  $S_r = 2$  and  $S_l = -1$ , [83],  $G_{r,l}$  is called the depolarization factor, [148], and  $\mu_{j1}$  and  $\rho_{j1}$  are the dipole moment and density matrix element for the transition  $|j\rangle \leftrightarrow |1\rangle$ , respectively. The terms  $\omega_{nk}$  are the quantized frequencies of plasmon-polaritons. The first and second terms in equation (7.1a) correspond to the Hamiltonian of the QD and electric fields, (both internal and external) respectively.

The last term of the Hamiltonian, i.e. equation (7.1d), refers to the decay interaction for states  $|2\rangle$  and  $|3\rangle$  due to the background radiation field and the exciton-SPPs. The two terms that make up  $\Omega_i$ , equation (7.3b), are due to the direct contributions from the external fields and the dipole fields from the MNR that are induced by the external fields, respectively. The term  $\Lambda_i$ , equation (7.4), is the DDI term which arises when the probe and control fields polarize the QD, which in turn polarizes the MNR.

### 7.3 Density Matrix Method

We use the density matrix method to evaluate the power loss in our MNR. Using equation (7.1a) we obtained the following expressions for density matrix elements,

$$\begin{aligned}
\dot{\rho}_{22} &= -2\Gamma_2\rho_{22} + i(\Omega_{12} + \Lambda_2\rho_{21})\rho_{12} - i(\Omega_{12}^* + \Lambda_2^*\rho_{12})\rho_{21} \\
\dot{\rho}_{33} &= -2\Gamma_3\rho_{33} + i(\Omega_{13} + \Lambda_3\rho_{31})\rho_{13} - i(\Omega_{13}^* + \Lambda_3^*\rho_{13})\rho_{31} \\
\dot{\rho}_{32} &= -(\Gamma_{32} - i\delta_{12} + i\delta_{13})\rho_{32} - i(\Omega_{12}^* + \Lambda_2^*\rho_{12})\rho_{31} \\
&\quad + i(\Omega_{13} + \Lambda_3\rho_{31})\rho_{12} \\
\dot{\rho}_{21} &= -[(\Gamma_{21} + \Gamma_2) - i(\delta_{12} + \Delta_2)]\rho_{21} + i\Omega_{12}(\rho_{11} - \rho_{22}) \\
&\quad - i(\Omega_{13} + \Lambda_3\rho_{31})\rho_{23} \\
\dot{\rho}_{31} &= -[(\Gamma_{31} + \Gamma_3) - i(\delta_{13} + \Delta_3)]\rho_{31} - i(\Omega_{12} + \Lambda_2\rho_{21})\rho_{32} \\
&\quad - i\Omega_{13}(\rho_{33} - \rho_{11})
\end{aligned} \tag{7.9}$$

where:

$$\Gamma_{32} = (\Gamma_2 + \Gamma_3) \tag{7.10}$$

$$\delta_{12} = \omega_2 - \omega_{21} \tag{7.11}$$

$$\delta_{13} = \omega_3 - \omega_{31} \tag{7.12}$$

$$\Gamma_{j1} = \text{Im} \left[ \Lambda_j (\rho_{11} - \rho_{jj}) \right] \tag{7.13}$$

$$\Delta_j = \text{Re} \left[ \Lambda_j (\rho_{11} - \rho_{jj}) \right] \tag{7.14}$$

Here,  $\Delta_j$  and  $\Gamma_{j1}$  with  $j = 2, 3$  are the nonradiative energy shift and decay rate due to dipole-dipole interaction term  $\Lambda_j$ . The  $\Gamma_j$  terms are the spontaneous decay rates for the excited state  $|j\rangle$  due to the background radiation field and the SPPs. They are found to be:

$$\Gamma_j = \Gamma_0 \left[ \frac{c^2 D_j}{2r_m l_m \omega_{j1}} \right] \left[ 1 + \frac{\gamma_{r,l} S_{r,l} (r_m^2 l_m)}{\epsilon_{dr} R^3} \right]^2 \tag{7.15}$$

where:

$$D_j = \sum_n \frac{l_m F(\omega_{j1}) \xi(\omega_{j1}) \Theta(\omega_{j1} - \omega_n)}{\pi \sqrt{F^2(\omega_{j1}) - F^2(\omega_n)}} \tag{7.16}$$

$$F^2(\omega_{j1}) = \frac{\omega_{j1}^2 (\omega_{j1}^2 - \omega_p^2) / 3c^2}{S_{r,l} (\omega_{j1}^2 - \omega_p^2) + (1 - S_{r,l}) \epsilon_b \omega_{j1}^2} \tag{7.17}$$

where:

$$\xi(\omega_k) = \frac{dF(\omega_k)}{d\omega_k} \tag{7.18}$$

In the above,  $c$  is the speed of light,  $\Theta(\omega_{j1} - \omega_n)$  is the Theta function, or the unit step function, and  $\Gamma_0$  is the decay rate from excitons due to the background radiation field. These decay rates are another difference between this setup and that of chapter 6. The decay here is highly dependent on the arrangement of the axis of the MNR with respect to the QD, but that consideration does not exist when the MNP is a sphere.

## 7.4 The Energy Exchange

The rate of energy loss in the hybrid system is due to the decay of excitons in the QD and thermal energy loss in the MNR. The power loss in the MNR is denoted as  $W_m$  and is written as,

$$W_m = 2\pi l_m r_m^2 \text{Im}(\gamma_{r,l}) \sum_{j=2,3} \omega_j [u_E^2 + u_p^2] \quad (7.19)$$

where:

$$u_E = \frac{E_j^0}{2} + \frac{S_{r,l}\mu_{1j} \text{Re} \rho_{1j}}{2\pi\epsilon_{dr}R^3} \quad (7.20a)$$

$$u_p = \frac{S_{r,l}\mu_{1j} \text{Im} \rho_{1j}}{2\pi\epsilon_{dr}R^3} \quad (7.20b)$$

The power loss in the MNR depends on the  $\rho_{12}$  and  $\rho_{13}$  density matrix elements for the QD.

## 7.5 Results and Discussion

We consider a CdSe quantum dot with parameters  $\epsilon_d = 10$ ,  $\hbar\omega_{12} = 2$  eV [149],  $\Gamma_0 = 0.08$  ns<sup>-1</sup> [150], and a gold MNR with parameters  $r_m = 3$  nm and  $\omega_p = 9$  eV. The energy splitting  $\hbar\omega_{32} = \hbar\omega_{13} - \hbar\omega_{12}$  is taken as 41  $\mu$ eV [149]. The dielectric constant of the host material, silica is taken as  $\epsilon_b = 2.25$ . The probe and control fields have nearly the same frequency (i.e.  $\delta_c = \delta_p + \omega_{32}$ ) and they can have different intensities. The power loss spectrum in the MNR is plotted in figure 7.2 as a function of the probe detuning  $\delta_{12}$  for ellipticity ratio,  $l_m/r_m = 1.2$ . For that configuration,  $\Gamma_2 = \Gamma_3 = 0.04$  ns<sup>-1</sup> was calculated. The intensity of the probe field

is taken as  $I_p = 10 \text{ W/cm}^2$ . When the probe field is applied, the spectrum has two peaks and minima at  $\delta_{12} = 0$  (see solid line). However, when the control field with  $I_c = 10 \text{ W/cm}^2$  is applied, the spectrum has four peaks and two minima.

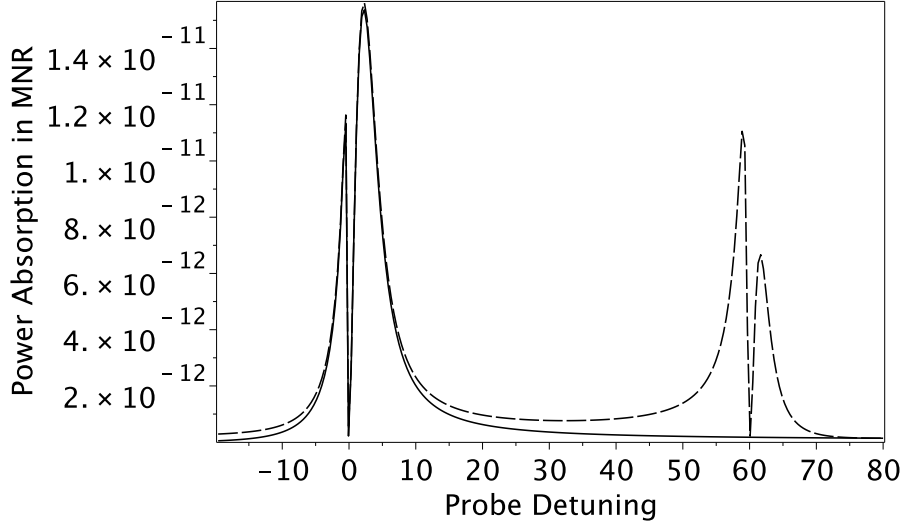


Figure 7.2:  $W_m$  (W) is plotted as a function of  $\delta_{12}$  ( $\text{ns}^{-1}$ ) where the solid curve and dashed curve correspond to when only the probe field or both the probe and control fields are applied, respectively. The control field has an intensity of  $I_c = 10 \text{ W/cm}^2$ .

The origin of the two minima is the interference between external and induced dipole fields. The probe field and its induced dipole field interfere in the MNR at  $\delta_{12} = 0$  whereas the control field and its induced dipole field interfere at  $\delta_{12} = \omega_{32}$ . Note that equation (7.19) contains two terms, where the second term, equation (7.20b), is negligible compared to the first term, equation (7.20a). The interference occurs due to the first term which contains two terms, namely the (probe/control) external field, and its induced dipole internal field. Note that the minimum at  $\delta_{12} = \omega_{32}$  is due to the control field. Therefore, we can say that the system can be switched from a two-peak state to a four-peak state by applying the control field to the QD.

The speed of switching can be regulated by the control field. When the exciton states are degenerate, (i.e.  $\omega_{32} = 0$ ) the two minima merge into one minimum and it is located at  $\delta_{12} = 0$ . It is important to note that it is difficult to find degenerate states in QDs since the single-exciton states split due to the so-called fine-structure-splitting [151]. However, as a

special case, degenerate states in QDs can exist when the line width of excitons is larger than the fine-structure-splitting.

The effect of the depolarization parameter  $\zeta_{r,l}$  and the ellipticity ratio has also been investigated. The results are plotted in figure 7.3 for  $\omega_{32} = 60 \text{ ns}^{-1}$ . The dashed and solid curves are plotted for ellipticity ratios 1.2 and 4, respectively. It was found that as the ellipticity ratio increases from 1.2 to 4, the transparent state at  $\delta_{12} = \omega_{32}$  in the spectrum disappears. This phenomenon occurs because the line width  $\Gamma_3 = 1.4 \text{ ns}^{-1}$  becomes larger than the line width of the minimum at  $\delta_{12} = \omega_{32}$ , and the line width  $\Gamma_2 = 0.04 \text{ ns}^{-1}$  is smaller than the line width of the minimum at  $\delta_{12} = 0$ .

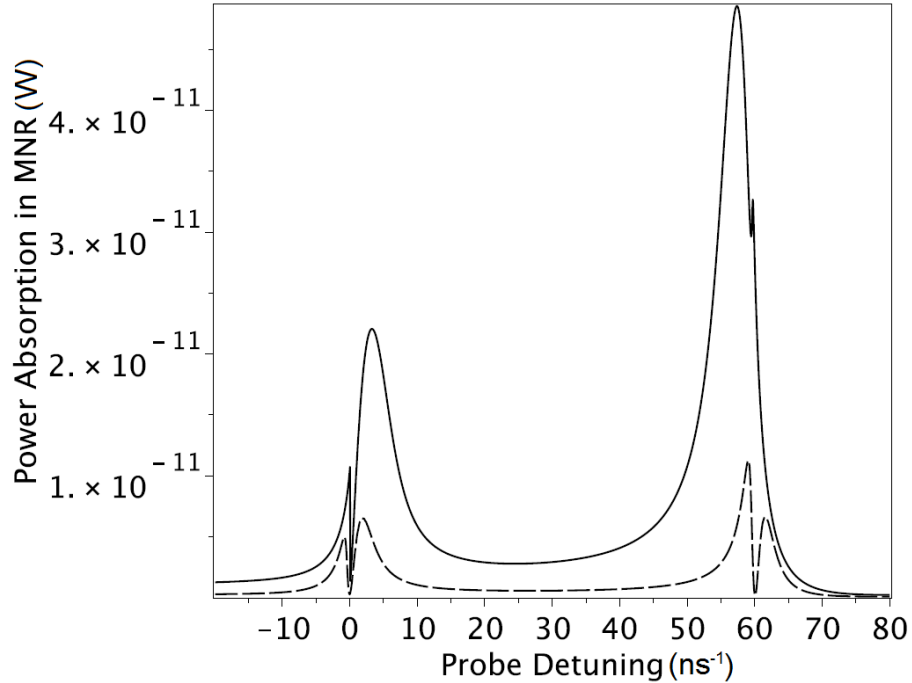


Figure 7.3:  $W_m$  (W) is plotted as a function of  $\delta_{12}$  ( $\text{ns}^{-1}$ ) where the solid and dashed curves are plotted for ellipticity ratios of  $l_m/r_m = 4$  and  $l_m/r_m = 1.2$ , respectively. The control field has an intensity of  $I_c = 10 \text{ W/cm}^2$ .

We have also investigated the effect of the control field intensity in figure 7.4. The solid and dashed curves correspond to  $I_c = 0.4 \text{ W/cm}^2$  and  $I_c = 10 \text{ W/cm}^2$ , respectively. When we change the intensity of the control field to  $I_c = 0.1 \text{ W/cm}^2$ , the transparent state at  $\delta_p = \omega_{32}$  disappears because there is no interference between the external and the induced dipole field.



Therefore, we can say that the system can be switched from a four-peak state to a three-peak state by applying the control field to the QD. One can say that the minimum at  $\delta_p = \omega_{32}$  can also be switched on and off by changing the intensity of the control field, or the ellipticity ratio of the QD. The speed of switching can be regulated by the control field.

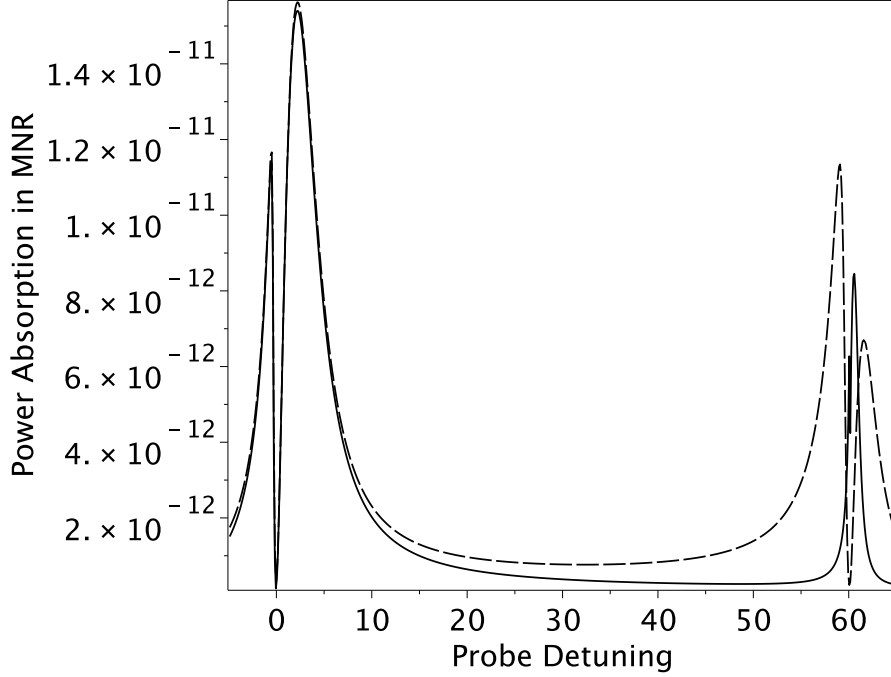


Figure 7.4:  $W_m$  (W) is plotted as a function of  $\delta_{12}$  ( $\text{ns}^{-1}$ ). The solid and dashed curves correspond to  $I_c = 0.4 \text{ W/cm}^2$  and  $I_c = 10 \text{ W/cm}^2$ , respectively.

The effect of the DDI (i.e.  $\Lambda_3$ ) due to the control field has also been investigated in figure 7.5. We have chosen the strength of both laser fields in such a way so that we do not see the interference effect in the power spectrum of the QD ( $I_p = 0.1 \text{ W/cm}^2$ ,  $I_c = 0.5 \text{ W/cm}^2$ ). The results are shown for  $R = 13 \text{ nm}$  (solid line) and  $R = 15 \text{ nm}$  (dashed line). Figure 7.5 is also plotted for an ellipticity ratio of  $l_m/r_m = 1.2$ . Also note that to accentuate the effects of the DDI, a different quantum dot was chosen for figure 7.5. In the previous figures, the transition dipole moments were taken to be  $\mu_{12} = \mu_{13} = 0.3 \text{ e nm}$ , but for figure 7.5, they were  $\mu_{12} = \mu_{13} = 1 \text{ e nm}$ .

Note that there are two peaks in the spectrum and these peaks correspond to the two dressed exciton states present in the QD. For  $R = 15 \text{ nm}$ , the locations of both peaks have shifted to

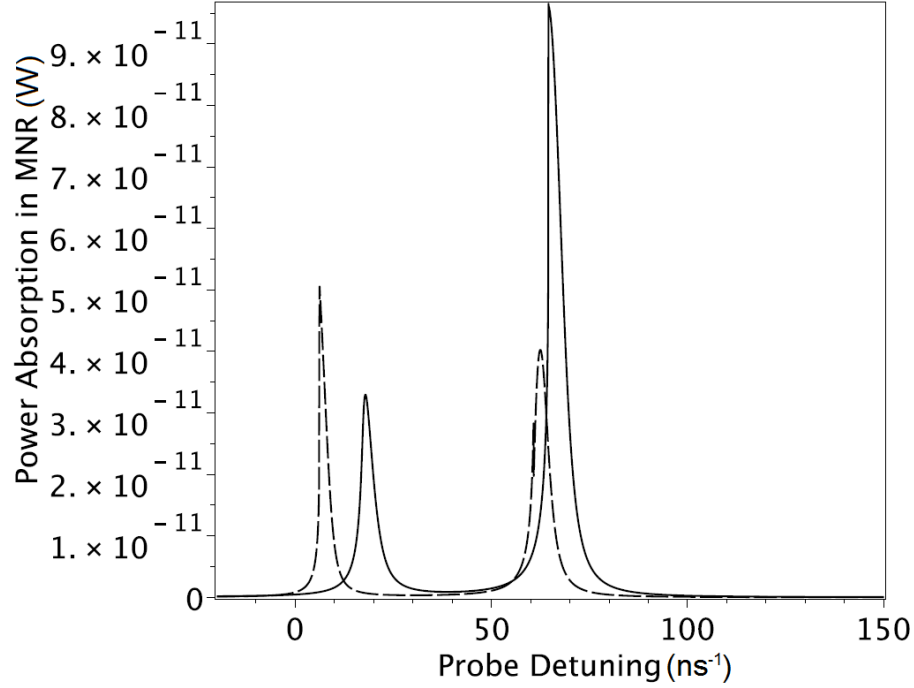


Figure 7.5:  $W_m$  (W) is plotted as a function of  $\delta_{12}$  ( $\text{ns}^{-1}$ ) with  $I_p = 0.1 \text{ W/cm}^2$  and  $I_c = 0.5 \text{ W/cm}^2$ . The solid curve and dashed curve correspond to  $R = 13 \text{ nm}$  and  $R = 15 \text{ nm}$ , respectively.

the left, and the widths of the peaks have decreased. This is because the strength of the DDI has decreased for  $R = 15 \text{ nm}$  and in turn, the values of  $\Delta_3$  and  $\Gamma_{31}$  have also been decreased as we expect from equations (7.13) and (7.14). Here,  $\Delta_3$  is responsible for the shift in the peak and  $\Gamma_{31}$  increases the width of the maximum. That is why the peaks have shifted to different positions and are arranged asymmetrically.

The shift in a peak means that a dressed exciton with  $\omega_{31} + \Delta_3$  is created due to the DDI. The dressed exciton has a shorter life time since its decay rate changes from  $\Gamma_3$  to  $(\Gamma_{31} + \Gamma_3)$ . Similarly, a second dressed exciton is created due to the DDI term  $\Lambda_2$ . This means that the hybrid system has two dressed exciton states for which the life time can be controlled by the dipole-dipole interaction.

## 7.6 Conclusion

In conclusion, we have investigated quantum coherence and interference phenomena in a QD-MNR hybrid system. It was found that the power spectrum of a MNR has three transparent states, and they can be switched to one transparent state by the control field. We have also found two dressed excitons with a short life time.

# Chapter 8

## Concluding Remarks

In this thesis, several optoelectronic properties of various nanostructures have been investigated. Light can be directed and confined by photonic crystals, in order that electron-photon interactions may be controlled. Within four geometries of photonic crystals, the allowed photon modes for a photonic nanowire have been studied. The transfer matrix method was used to model the photonic crystals, [18], and parameters were taken from an existing three dimensional photonic crystal [89].

For those setups in which two differing photonic crystals appeared in the nanowire, several photon modes were found. If fewer modes are desired, that number can be reduced as much as needed by adjusting the proportions of  $\text{Al}_x\text{Ga}_{1-x}\text{As}$  which is used in the fabrication of either photonic crystal. The wire, as discussed, had square and circular cross-sections, and the shift in shape altered the energy levels of the photon modes. There is a greater freedom in parameter choice in producing a wire that only has a single allowed photon mode for the photonic crystal core case, when there is a circular cross section and we are limited to transverse electric modes, rather than having a square cross-section. When we consider a photonic crystal with a dielectric core, more options arise for designing nanowires with only a single mode. The wire may be made smaller, and a wide variety of materials may form the said core. To compare the circular and square cross-sections with a dielectric core, the circular cross-

section must be thicker, for the same material, though not as thick as the nanowires which had photonic crystal cores. These structures form the backdrop for interactions between photons and electrons, where some control over these interactions has been exerted through the geometry of the system.

The effect of the dipole-dipole interaction (DDI) has been studied in photonic nanofibers in which a dielectric material forms a column within a photonic crystal. Bound photon energy states appear in this system. The core material is doped with an ensemble of three-level quantum dots (QDs). To this system, probe and control fields are applied so that the absorption coefficient may be studied. Dipoles are induced in QDs by these fields, and those dipoles interact with one another via the DDI. The electron-bound photon interaction allows the QDs to interact with the quantum nanofiber. The absorption coefficient has been evaluated with the density matrix method and the mean field approximation was used to calculate the DDI. The DDI was found to enable the system to be switched from a transparent state to an absorbing state. Another prediction was that by changing either the location of a bound state in the nanofiber or a resonant transition energy for the QDs, the absorption peak can be split into a transparent state and two absorbing peaks.

The energy transfer rate between donor and acceptor QDs was calculated when they are embedded in a nonlinear photonic crystal. It is found that the DDI facilitates energy transfer from the donor to the acceptor. This energy transfer can be controlled by a pump field.

The third QD system involved a metal nanosphere (MNS), but again, two lasers were used to help describe power absorption due to the nanoscopic hybrid systems. There was only a single absorption peak when no metal sphere was present, and the laser intensities were low enough. Similarly, when the MNS was very far from the quantum dot, there was a single absorption peak. As these two were moved closer together, this single peak was made to split into two peaks. This same splitting could also be observed if one increased the intensity of the control field. The former results from the DDI between the QD and the MNS, but the latter is present even without the MNS. The difference between these two mechanisms

is that a MNS also shifts the locations of the peaks, meaning that the peaks were no longer placed symmetrically about the former location of the single absorption peak. Therefore, the control field could act as a switch to turn off absorption in the quantum dot, and in the right circumstances, so could the presence of the MNS.

The last property of the QD-MNS system to be investigated was the fluorescence efficiency for the QD. The quantum dot fluorescence was quenched by the presence of a MNS when it was close enough to the QD. Furthermore, a metal nanosphere can switch off absorption at a particular frequency, but only if the field being absorbed is intense enough.

The final system to be investigated was a quantum dot-metal nanorod (QD-MNR) wherein quantum coherence and interference phenomena were studied. The power spectrum of the MNR was found to have three transparent states, and this spectrum can be switched to one transparent state by a control field. Two dressed excitons were found with a short life time.

There are many questions still to be addressed in the field of nanoscopic heterostructures. These structures include photonic fibers, cavities, or slabs, also quantum dots, metal nanospheres, nanorods, combinations of any of these, and there are a myriad of structures not discussed in this document. The sheer number of studies done in only the past few years speaks to how active and emerging this research area has become. As was mentioned in the beginning of this thesis, a great many devices employing photonic switches similar to the ones described here have been produced, and a great many more have been proposed. Given the wide variety of potential applications, a wide array of mechanisms with which to realize these photonic controllers will be needed.

# Bibliography

- [1] M. Notomi, A. Shinya, S. Mitsugi, G. Kira, E. Kuramochi, and T. Tanabe, “Optical bistable switching action of Si high-Q photonic-crystal nanocavities,” *Opt. Express*, vol. 13, p. 2678, 2005.
- [2] T. Tanabe, M. Notomi, S. Mitsugi, A. Shinya, and E. Kuramochi, “All-optical switches on a silicon chip realized using photonic crystal nanocavities,” *Appl. Phys. Lett.*, vol. 87, p. 151112, 2005.
- [3] V. R. Almeida, C. A. Barrios, R. R. Panepucci, and M. Lipson, “All-optical control of light on a silicon chip,” *Nature*, vol. 431, p. 1081, 2004.
- [4] M. F. Yanik, S. Fan, M. Soljačić, and J. D. Joannopoulos, “All-optical transistor action with bistable switching in a photonic crystal cross-waveguide geometry,” *Opt. Lett.*, vol. 28, p. 2506, 2003.
- [5] A. Haché and M. Bourgeois, “Ultrafast all-optical switching in a silicon-based photonic crystal,” *Appl. Phys. Lett.*, vol. 77, p. 4089, 2000.
- [6] J. W. S. Rayleigh, “On the remarkable phenomenon of crystalline reflexion described by Prof. Stokes,” *Philos. Mag.*, vol. 26, p. 256, 1888.
- [7] S. John, “Strong localization of photons in certain disordered dielectric superlattices,” *Phys. Rev. Lett.*, vol. 58, p. 2486, 1987.
- [8] E. Yablonovitch, “Inhibited spontaneous emission in solid-state physics and electronics,” *Phys. Rev. Lett.*, vol. 58, p. 2059, 1987.
- [9] T. Krauss, R. M. de la Rue, and S. Brand, “Two-dimensional photonic-bandgap structures operating at near-infrared wavelengths,” *Nature*, vol. 383, p. 699, 1996.
- [10] J. D. Joannopoulos and J. N. Winn, *Photonic Crystals: Molding the Flow of Light*. Princeton University Press, 1995.
- [11] V. I. Rupasov and M. R. Singh, “Quantum gap solitons and many-polariton—atom bound states in dispersive medium and photonic band gap,” *Phys. Rev. Lett.*, vol. 77, p. 338, 1996.
- [12] P. Lambropoulos, G. M. Nikolopoulos, T. R. Nielsen, and S. Bay, “Fundamental quantum optics in structured reservoirs,” *Rep. Prog. Phys.*, vol. 63, p. 455, 2000.

- [13] P. N. Prasad, *Nanophotonics*. Willey Interscience, 2004.
- [14] M. R. Singh, "Transparency in nanophotonic quantum wires," *J. Phys. B: At. Mol. Opt. Phys.*, vol. 42, p. 065503, 2009.
- [15] E. Istrate and E. H. Sargent, "Photonic crystal heterostructures and interfaces," *Rev. Mod. Phys.*, vol. 78, p. 455, 2006.
- [16] J. D. Joannopoulos, S. G. Johnson, J. N. Winn, and R. D. Meade, *Photonic Crystals*. Princeton U. Press, 2008.
- [17] V. I. Rupasov and M. R. Singh, "Quantum gap solitons and soliton pinning in dispersive medium and photonic-band-gap materials: Bethe-ansatz solution," *Phys. Rev. A*, vol. 54, p. 3614, 1996.
- [18] M. R. Singh, "A study of optoelectronics in photonic nanowires made from photonic crystals," *Appl. Phys. B*, vol. 93, p. 91, 2008.
- [19] K. Asakawa, Y. Sugimoto, Y. Watanabe, N. Ozaki, A. Mizutani, Y. Takata, Y. Kitagawa, H. Ishikawa, N. Ikeda, K. Awazu, X. Wang, A. Watanabe, S. Nakamura, S. Ohkouchi, K. Inoue, M. Kristensen, O. Sigmund, P. I. Borel, and R. Baets, "Photonic crystal and quantum dot technologies for all-optical switch and logic device," *New J. Phys.*, vol. 8, p. 208, 2006.
- [20] W. Wang and S. A. Asher, "Photochemical incorporation of silver quantum dots in monodisperse silica colloids for photonic crystal applications," *J. Am. Chem. Soc.*, vol. 123, p. 12528, 2001.
- [21] P. Alivisatos, "The use of nanocrystals in biological detection," *Nat. Biotechnol.*, vol. 22, p. 47, 2004.
- [22] M. Nomura, S. Iwamoto, K. Watanabe, N. Kumagai, Y. Nakata, S. Ishida, and Y. Arakawa, "Room temperature continuous-wave lasing in photonic crystal nanocavity," *Opt. Express*, vol. 14, no. 13, p. 6308, 2006.
- [23] H. Altug, D. Englund, and J. Vučković, "Ultrafast photonic crystal nanocavity laser," *Nat. Phys.*, vol. 2, p. 484, 2006.
- [24] A. I. Ekimov and A. A. Onushchenko, "Quantum size effect in three-dimensional microscopic semiconductor crystals," *JETP Lett.*, vol. 34, p. 345, 1981.
- [25] R. Rossetti and L. Brus, "Electron-hole recombination emission as a probe of surface chemistry in aqueous cadmium sulfide colloids," *J. Phys. Chem.*, vol. 86, p. 4470, 1982.
- [26] M. A. Reed, J. N. Randall, R. J. Aggarwal, R. J. Matyi, T. M. Moore, and A. E. Wetsel, "Observation of discrete electronic states in a zero-dimensional semiconductor nanostructure," *Phys. Rev. Lett.*, vol. 60, p. 535, 1988.



- [27] W. Lai, S. Chakravarty, X. Wang, C. Lin, and R. T. Chen, "On-chip methane sensing by near-IR absorption signatures in a photonic crystal slot waveguide," *Opt. Lett.*, vol. 36, no. 6, p. 984, 2011.
- [28] D. Englund, A. Faraon, B. Zhang, Y. Yamamoto, and J. Vučković, "Generation and transfer of single photons on a photonic crystal chip," *Opt. Express*, vol. 15, p. 5550, 2007.
- [29] W. Chang, W. Chen, H. Chang, T. Hsieh, J. Chyi, and T. Hsu, "Efficient single-photon sources based on low-density quantum dots in photonic-crystal nanocavities," *Phys. Rev. Lett.*, vol. 96, p. 117401, 2006.
- [30] X. Hu, Y. Liu, J. Tian, B. Cheng, and D. Zhang, "Ultrafast all-optical switching in two-dimensional organic photonic crystal," *Appl. Phys. Lett.*, vol. 86, p. 121102, 2005.
- [31] M. R. Lee and P. M. Fauchet, "Two-dimensional silicon photonic crystal based biosensing platform for protein detection," *Opt. Express*, vol. 15, p. 4530, 2007.
- [32] D. Lauvernier, S. Garidel, M. Zegaoui, J. P. Vilcot, and D. Decoster, "GaAs/polymer optical nanowires: Fabrication and characterisation," *Electron. Lett.*, vol. 42, p. 217, 2006.
- [33] B. G. Lee, X. Chen, A. Biberman, X. Liu, I. Hsieh, C. Chou, J. I. Dadap, F. Xia, W. M. J. Green, L. Sekaric, Y. A. Vlasov, R. M. Osgood Jr., and K. Bergman, "Ultrahigh-bandwidth silicon photonic nanowire waveguides for on-chip networks," *IEEE Photonics Technol. Lett.*, vol. 20, p. 398, 2008.
- [34] M. A. Schmidt, L. N. P. Sempere, H. K. Tyagi, C. G. Poulton, and P. S. J. Russell, "Waveguiding and plasmon resonances in two-dimensional photonic lattices of gold and silver nanowires," *Phys. Rev. B*, vol. 77, p. 033417, 2008.
- [35] N. Gisin, G. Ribordy, W. Tittel, and H. Zbinden, "Quantum cryptography," *Rev. Mod. Phys.*, vol. 74, p. 145, 2002.
- [36] M. R. Singh and D. Schindel, "Photon absorption in interacting quantum dots doped in nanofibers," *J. Opt. Soc. Am. B*, vol. 27, p. 2759, 2010.
- [37] Y. Nakayama, P. J. Pauzauskie, A. Radenovic, R. M. Onorato, R. J. Saykally, J. Liphardt, and P. Yang, "Tunable nanowire nonlinear optical probe," *Nature*, vol. 447, p. 1098, 2007.
- [38] V. A. Sautenkov, H. van Kampen, E. R. Eliel, and J. P. Woerdman, "Dipole-dipole broadened line shape in a partially excited dense atomic gas," *Phys. Rev. Lett.*, vol. 77, p. 3327, 1996.
- [39] O. Calderón, M. Antón, and F. Carreño, "Near dipole-dipole effects in a V-type medium with vacuum induced coherence," *Eur. Phys. J. D*, vol. 25, p. 77, 2003.

- [40] T. Pohl and P. R. Berman, “Breaking the dipole blockade: Nearly resonant dipole interactions in few-atom systems,” *Phys. Rev. Lett.*, vol. 102, p. 013004, 2009.
- [41] E. Paspalakis, A. Kalini, and A. F. Terzis, “Local field effects in excitonic population transfer in a driven quantum dot system,” *Phys. Rev. B*, vol. 73, p. 073305, 2006.
- [42] Ö. Çakir, A. A. Klyachko, and A. S. Shumovsky, “Steady-state entanglement of two atoms created by classical driving field,” *Phys. Rev. A*, vol. 71, p. 034303, 2005.
- [43] C. Skornia, J. von Zanthier, G. S. Agarwal, E. Werner, and H. Walther, “Monitoring the dipole-dipole interaction via quantum jumps of individual atoms,” *Phys. Rev. A*, vol. 64, p. 053803, 2001.
- [44] J. Evers, M. Kiffner, M. Macovei, and C. H. Keitel, “Geometry-dependent dynamics of two  $\Lambda$ -type atoms via vacuum-induced coherences,” *Phys. Rev. A*, vol. 73, p. 023804, 2006.
- [45] S. Xie, Y. Yang, H. Chen, and S. Zhu, “Atom-atom interaction in an anisotropic photonic crystal,” *J. Mod. Opt.*, vol. 50, p. 83, 2003.
- [46] M. R. Singh, “Transparency and spontaneous emission in a densely doped photonic band gap material,” *J. Phys. B: At. Mol. Opt. Phys.*, vol. 39, p. 5131, 2006.
- [47] M. R. Singh, “Switching mechanism due to the spontaneous emission cancellation in photonic bandgap materials doped with nano-particles,” *Phys. Lett. A*, vol. 363, p. 177, 2007.
- [48] M. R. Singh, “Dipole-dipole interaction in photonic-band-gap materials doped with nanoparticles,” *Phys. Rev. A*, vol. 75, p. 043809, 2007.
- [49] M. R. Singh, “Inhibition of two-photon absorption due to dipole-dipole interaction in nanoparticles,” *Phys. Lett. A*, vol. 372, p. 5083, 2008.
- [50] M. R. Singh, “Controlling photon absorption in photonic nanowires via dipole-dipole interaction,” *Opt. Lett.*, vol. 34, p. 2909, 2009.
- [51] R. D. Artuso and G. W. Bryant, “Strongly coupled quantum dot-metal nanoparticle systems: Exciton-induced transparency, discontinuous response, and suppression as driven quantum oscillator effects,” *Phys. Rev. B*, vol. 82, p. 195419, 2010.
- [52] M. R. Singh, D. Schindel, and A. Hatef, “Dipole-dipole interaction in a quantum dot and metallic nanorod hybrid system,” *Appl. Phys. Lett.*, vol. 99, p. 181106, 2011.
- [53] A. L. Rogach, *Semiconductor Nanocrystal Quantum Dots*. Springer, 2008.
- [54] A. G. Curto, G. Volpe, T. H. Taminiau, M. P. Kreuzer, R. Quidant, and N. F. van Hulst, “Unidirectional emission of a quantum dot coupled to a nanoantenna,” *Science*, vol. 329, p. 930, 2010.

- [55] K. T. Shimizu, W. K. Woo, B. R. Fisher, H. J. Eisler, and M. G. Bawendi, “Surface-enhanced emission from single semiconductor nanocrystals,” *Phys. Rev. Lett.*, vol. 89, p. 117401, 2002.
- [56] X. Wu, H. Liu, J. Liu, K. N. Haley, J. A. Treadway, J. P. Larson, N. Ge, F. Peale, and M. P. Bruchez, “Immunofluorescent labeling of cancer marker Her2 and other cellular targets with semiconductor quantum dots,” *Nat. Biotechnol.*, vol. 21, p. 41, 2003.
- [57] X. Michalet, F. F. Pinaud, L. A. Bentolila, J. M. Tsay, S. Doose, J. J. Li, G. Sundaresan, A. M. Wu, S. S. Gambhir, and S. Weiss, “Quantum dots for live cells, in vivo imaging, and diagnostics,” *Science*, vol. 307, p. 538, 2005.
- [58] T. Franzl, T. A. Klar, S. Schietinger, A. L. Rogach, and J. Feldmann, “Exciton recycling in graded gap nanocrystal structures,” *Nano Lett.*, vol. 4, p. 1599, 2004.
- [59] I. L. Medintz, A. R. Clapp, H. Mattoussi, E. R. Goldman, B. Fisher, and J. M. Mauro, “Self-assembled nanoscale biosensors based on quantum dot FRET donors,” *Nature Mater.*, vol. 2, p. 630, 2003.
- [60] A. V. Akimov, A. Mukherjee, C. L. Yu, D. E. Chang, A. S. Zibrov, P. R. Hemmer, H. Park, and M. D. Lukin, “Generation of single optical plasmons in metallic nanowires coupled to quantum dots,” *Nature*, vol. 450, p. 402, 2007.
- [61] Y. Fedutik, V. V. Temnov, O. Schöps, U. Woggon, and M. V. Artemyev, “Exciton-plasmon-photon conversion in plasmonic nanostructures,” *Phys. Rev. Lett.*, vol. 99, p. 136802, 2007.
- [62] J. Lindberg, K. Lindfors, T. Setälä, and M. Kaivola, “Dipole-dipole interaction between molecules mediated by a chain of silver nanoparticles,” *J. Opt. Soc. Am. A*, vol. 24, p. 3427, 2007.
- [63] E. Altewisher, M. P. van Exter, and J. P. Woerdman, “Plasmon-assisted transmission of entangled photons,” *Nature*, vol. 418, p. 304, 2002.
- [64] S. Fasel, F. Robin, E. Moreno, D. Erni, N. Gisin, and H. Zbinden, “Energy-time entanglement preservation in plasmon-assisted light transmission,” *Phys. Rev. Lett.*, vol. 94, p. 110501, 2005.
- [65] A. Gonzalez-Tudela, D. Martin-Cano, E. Moreno, L. Martin-Moreno, C. Tejedor, and F. J. Garcia-Vidal, “Entanglement of two qubits mediated by one-dimensional plasmonic waveguides,” *Phys. Rev. Lett.*, vol. 106, p. 020501, 2011.
- [66] D. Dzotjan, A. S. Sørensen, and M. Fleischhauer, “Quantum emitters coupled to surface plasmons of a nanowire: A Green’s function approach,” *Phys. Rev. B*, vol. 82, p. 075427, 2010.
- [67] T. Pons, I. L. Medintz, K. E. Sapsford, S. Higashiya, A. F. Grimes, D. S. English, and H. Mattoussi, “On the quenching of semiconductor quantum dot photoluminescence by proximal gold nanoparticles,” *Nano Lett.*, vol. 7, p. 3157, 2007.

- [68] S. M. Sadeghi, “Tunable nanoswitches based on nanoparticle meta-molecules,” *Nanotechnology*, vol. 21, p. 355501, 2010.
- [69] R. Esteban, T. V. Teperik, and J. J. Greffet, “Optical patch antennas for single photon emission using surface plasmon resonances,” *Phys. Rev. Lett.*, vol. 104, p. 026802, 2010.
- [70] M. Liu, T. Lee, S. K. Gray, P. Guyot-Sionnest, and M. Pelton, “Excitation of dark plasmons in metal nanoparticles by a localized emitter,” *Phys. Rev. Lett.*, vol. 102, p. 107401, 2009.
- [71] D. Martín-Cano, L. Martín-Moreno, F. J. García-Vidal, and E. Moreno, “Resonance energy transfer and superradiance mediated by plasmonic nanowaveguides,” *Nano Lett.*, vol. 10, p. 3129, 2010.
- [72] A. A. Toropov, T. V. Shubina, K. G. Belyaev, S. V. Ivanov, P. S. Kop’ev, Y. Ogawa, and F. Minami, “Enhancement of excitonic emission in semiconductor heterostructures due to resonant coupling to multipole plasmon modes in a gold particle,” *Phys. Rev. B*, vol. 84, p. 085323, 2011.
- [73] R. D. Artuso, G. W. Bryant, A. Garcia-Etxarri, and J. Aizpurua, “Using local fields to tailor hybrid quantum-dot/metal nanoparticle systems,” *Phys. Rev. B*, vol. 83, p. 235406, 2011.
- [74] S. M. Sadeghi, “Coherent control of metallic nanoparticles near fields: Nanopulse controllers and functional nanoamplifiers,” *Phys. Rev. B*, vol. 82, p. 035413, 2010.
- [75] H. Mertens, J. S. Biteen, H. A. Atwater, and A. Polman, “Polarization-selective plasmon-enhanced silicon quantum-dot luminescence,” *Nano Lett.*, vol. 6, p. 2622, 2006.
- [76] M. Cheng, S. Liu, H. Zhou, Z. Hao, and Q. Wang, “Coherent exciton-plasmon interaction in the hybrid semiconductor quantum dot and metal nanoparticle complex,” *Opt. Lett.*, vol. 32, p. 2125, 2007.
- [77] A. Ridolfo, O. D. Stefano, N. Fina, R. Saija, and S. Savasta, “Quantum plasmonics with quantum dot-metal nanoparticle molecules: Influence of the Fano effect on photon statistics,” *Phys. Rev. Lett.*, vol. 105, p. 263601, 2010.
- [78] W. Zhang, A. O. Govorov, and G. W. Bryant, “Semiconductor-metal nanoparticle molecules: Hybrid excitons and the nonlinear Fano effect,” *Phys. Rev. Lett.*, vol. 97, p. 146804, 2006.
- [79] R. D. Artuso and G. W. Bryant, “Optical response of strongly coupled quantum dot-metal nanoparticle systems: Double peaked Fano structure and bistability,” *Nano Lett.*, vol. 8, p. 2106, 2008.
- [80] A. O. Govorov, “Semiconductor-metal nanoparticle molecules in a magnetic field: Spin-plasmon and exciton-plasmon interactions,” *Phys. Rev. B*, vol. 82, p. 155322, 2010.

- [81] A. O. Govorov, G. W. Bryant, W. Zhang, T. Skeini, J. Lee, N. A. Kotov, J. M. Slocik, and R. R. Naik, “Exciton-plasmon interaction and hybrid excitons in semiconductor-metal nanoparticle assemblies,” *Nano Lett.*, vol. 6, p. 984, 2006.
- [82] M. Achermann, “Exciton–plasmon interactions in metal–semiconductor nanostructures,” *J. Phys. Chem. Lett.*, vol. 1, p. 2837, 2010.
- [83] S. M. Sadeghi, L. Deng, X. Li, and W. Huang, “Plasmonic (thermal) electromagnetically induced transparency in metallic nanoparticle–quantum dot hybrid systems,” *Nanotechnology*, vol. 20, p. 365401, 2009.
- [84] V. Yannopapas, E. Paspalakis, and N. V. Vitanov, “Plasmon-induced enhancement of quantum interference near metallic nanostructures,” *Phys. Rev. Lett.*, vol. 103, p. 063602, 2009.
- [85] A. Hatef and M. R. Singh, “Plasmonic effect on quantum coherence and interference in metallic photonic crystals doped with quantum dots,” *Phys. Rev. A*, vol. 81, p. 063816, 2010.
- [86] S. Evangelou, V. Yannopapas, and E. Paspalakis, “Modifying free-space spontaneous emission near a plasmonic nanostructure,” *Phys. Rev. A*, vol. 83, p. 023819, 2011.
- [87] S. Evangelou, V. Yannopapas, and E. Paspalakis, “Simulating quantum interference in spontaneous decay near plasmonic nanostructures: Population dynamics,” *Phys. Rev. A*, vol. 83, p. 055805, 2011.
- [88] M. Durach, A. Rusina, V. I. Klimov, and M. I. Stockman, “Nanoplasmonic renormalization and enhancement of Coulomb interactions,” *New J. Phys.*, vol. 10, p. 105011, 2008.
- [89] S. Noda, N. Yamamoto, H. Kobayashi, M. Okano, and K. Tomoda, “Optical properties of three-dimensional photonic crystals based on III-V semiconductors at infrared to near-infrared wavelengths,” *Appl. Phys. Lett.*, vol. 75, p. 905, 1999.
- [90] J. Khatei, S. K. Sahoo, and K. S. R. K. Rao, “Electronic energy transfer between long-range resonance states of 3-mercaptopropionic acid capped CdTe quantum dots in aqueous media,” *J. Exp. Nanosci.*, 2012.
- [91] C. Higgins, M. Lunz, A. L. Bradley, V. A. Gerard, S. Byrne, Y. K. Gun’ko, V. Lesnyak, and N. Gaponik, “Energy transfer in colloidal CdTe quantum dot nanoclusters,” *Opt. Express*, vol. 18, p. 24486, 2010.
- [92] M. Lunz, A. L. Bradley, W. Chen, V. A. Gerard, S. J. Byrne, Y. K. Gun’ko, V. Lesnyak, and N. Gaponik, “Influence of quantum dot concentration on Förster resonant energy transfer in monodispersed nanocrystal quantum dot monolayers,” *Phys. Rev. B*, vol. 81, p. 205316, 2010.
- [93] B. Gralak, S. Enoch, and G. Tayeb, “Anomalous refractive properties of photonic crystals,” *J. Opt. Soc. Am. A*, vol. 17, p. 1012, 2000.

- [94] E. Yablonovitch and T. J. Gmitter, "Photonic band structure: The face-centered-cubic case," *Phys. Rev. Lett.*, vol. 63, p. 1950, 1989.
- [95] S. Imagawa, K. Edagawa, K. Morita, T. Niino, Y. Kagawa, and M. Notomi, "Photonic band-gap formation, light diffusion, and localization in photonic amorphous diamond structures," *Phys. Rev. B*, vol. 82, p. 115116, 2010.
- [96] P. N. Dyachenko, N. D. Kundikova, and Y. V. Miklyaev, "Band structure of a photonic crystal with the clathrate Si-34 lattice," *Phys. Rev. B*, vol. 79, p. 233102, 2009.
- [97] A. Hatef and M. R. Singh, "The study of quantum interference in metallic photonic crystals doped with four-level quantum dots," *Nanoscale Res. Lett.*, vol. 5, p. 464, 2010.
- [98] J. E. G. J. Wijnhoven, L. Bechger, and W. L. Vos, "Fabrication and characterization of large macroporous photonic crystals in titania," *Chem. Mater.*, vol. 13, p. 4486, 2001.
- [99] A. Blanco, E. Chomski, S. Grabtchak, M. Ibisate, S. John, S. W. Leonard, C. Lopez, F. Meseguer, H. Miguez, J. P. Mondia, G. A. Ozin, O. Toader, and H. M. van Driel, "Large-scale synthesis of a silicon photonic crystal with a complete three-dimensional bandgap near 1.5 micrometres," *Nature*, vol. 405, p. 437, 2000.
- [100] J. E. G. J. Wijnhoven and W. L. Vos, "Preparation of photonic crystals made of air spheres in titania," *Science*, vol. 281, p. 802, 1998.
- [101] R. E. Galian, M. Laferrière, and J. C. Scaiano, "Doping of photonic crystal fibers with fluorescent probes: possible functional materials for optrode sensors," *J. Mater. Chem.*, vol. 16, p. 1697, 2006.
- [102] M. J. Ventura and M. Gu, "Engineering spontaneous emission in a quantum-dot-doped polymer nanocomposite with three-dimensional photonic crystals," *Adv. Mater.*, vol. 20, p. 1329, 2008.
- [103] H. Park, S. Kim, S. Kwon, Y. Ju, J. Yang, J. Baek, S. Kim, and Y. Lee, "Electrically driven single-cell photonic crystal laser," *Science*, vol. 305, p. 1444, 2004.
- [104] D. Leonard, M. Krishnamurthy, S. Fafard, J. L. Merz, and P. M. Petroff, "Molecular-beam epitaxy growth of quantum dots from strained coherent uniform islands of InGaAs on GaAs," *J. Vac. Sci. Technol. B*, vol. 12, p. 1063, 1994.
- [105] M. Illing, G. Bacher, T. Kummell, A. Forchel, T. G. Andersson, D. Hommel, B. Jobst, and G. Landwehr, "Lateral quantization effects in lithographically defined CdZnSe/ZnSe quantum dots and quantum wires," *Appl. Phys. Lett.*, vol. 67, p. 124, 1995.
- [106] H. Cao, J. Y. Xu, W. H. Xiang, Y. Ma, S.-H. Chang, S. T. Ho, and G. S. Solomon, "Optically pumped InAs quantum dot microdisk lasers," *Appl. Phys. Lett.*, vol. 76, p. 3519, 2000.
- [107] S. Lee, C. Mao, C. Flynn, and A. Belcher, "Ordering of quantum dots using genetically engineered viruses," *Science*, vol. 296, p. 892, 2002.

- [108] C. Murray, C. Kagan, and M. Bawendi, “Self-organization of CdSe nanocrystallites into three-dimensional quantum dot superlattices,” *Science*, vol. 270, p. 1335, 1995.
- [109] M. Nirmal, D. J. Norris, M. Kuno, M. G. Bawendi, A. L. Efros, and M. Rosen, “Observation of the ”dark exciton” in cdse quantum dots,” *Phys. Rev. Lett.*, vol. 75, p. 3728, Nov 1995.
- [110] B. D. Gerardot, D. Brunner, P. A. Dalgarno, K. Karrai, A. Badolato, P. M. Petroff, and R. J. Warburton, “Dressed excitonic states and quantum interference in a three-level quantum dot ladder system,” *New J. Phys.*, vol. 11, p. 013028, 2009.
- [111] X. Xu, B. Sun, P. R. Berman, D. G. Steel, A. S. Bracker, D. Gammon, and L. J. Sham, “Coherent population trapping of an electron spin in a single negatively charged quantum dot,” *Nat. Phys.*, vol. 4, p. 692, 2008.
- [112] R. Johnston and J. Wilcoxon, *Metal Nanoparticles and Nanoalloys*. Elsevier, 2012.
- [113] S. Eustis and M. Al-Sayed, “Why gold nanoparticles are more precious than pretty gold: Noble metal surface plasmon resonance and its enhancement of the radiative and nonradiative properties of nanocrystals of different shapes,” *Chem. Soc. Rev.*, vol. 35, p. 209, 2006.
- [114] D. Kang, J. Maclennan, N. Clark, A. Zakhidov, and R. Baughman, “Electro-optic behavior of liquid-crystal-filled silica opal photonic crystals: Effect of liquid-crystal alignment,” *Phys. Rev. Lett.*, vol. 86, p. 4052, 2001.
- [115] Y. A. Vlastov, V. N. Astratov, A. V. Baryshev, A. A. Kaplyanskii, O. Z. Karimov, and M. F. Limonov, “Manifestation of intrinsic defects in optical properties of self-organized opal photonic crystals,” *Phys. Rev. E*, vol. 61, p. 5784, 2000.
- [116] S. John and J. Wang, “Quantum electrodynamics near a photonic band gap: Photon bound states and dressed atoms,” *Phys. Rev. Lett.*, vol. 64, p. 2418, 1990.
- [117] K. Okamoto, *Fundamentals of Optical Waveguides*. Elsevier, 2006.
- [118] J. F. Bertone, P. Jiang, K. Hwang, D. Mittleman, and V. Colvin, “Thickness dependence of the optical properties of ordered silica-air and air-polymer photonic crystals,” *Phys. Rev. Lett.*, vol. 83, p. 300, 1999.
- [119] P. Lodahl, A. F. van Driel, I. S. Nikolaev, A. Irman, K. Overgaag, D. Vanmaekelbergh, and W. L. Vos, “Controlling the dynamics of spontaneous emission from quantum dots by photonic crystals,” *Nature*, vol. 430, p. 654, 2004.
- [120] J. F. Dynes, M. D. Frogley, M. Beck, J. Faist, and C. C. Phillips, “ac Stark splitting and quantum interference with intersubband transitions in quantum wells,” *Phys. Rev. Lett.*, vol. 94, p. 157403, 2005.
- [121] E. Hendry, M. Koeberg, F. Wang, H. Zhang, C. de M. Donegá, D. Vanmaekelbergh, and M. Bonn, “Direct observation of electron-to-hole energy transfer in CdSe quantum dots,” *Phys. Rev. Lett.*, vol. 96, p. 057408, 2006.

- [122] S. John and J. Wang, “Quantum optics of localized light in a photonic band gap,” *Phys. Rev. B*, vol. 43, p. 12772, 1991.
- [123] K. B. Chung and S. H. Kim, “Defect modes in a two-dimensional square-lattice photonic crystal,” *Opt. Commun.*, vol. 209, p. 229, 2002.
- [124] S. John and M. Florescu, “Photonic bandgap materials: Towards an all-optical micro-transistor,” *J. Opt. A: Pure Appl. Opt.*, vol. 3, p. S103, 2001.
- [125] M. R. Singh and R. Lipson, “Optical switching in nonlinear photonic crystals lightly doped with nanostructures,” *J. Phys. B: At. Mol. Opt. Phys.*, vol. 41, p. 015401, 2008.
- [126] D. Petrosyan and G. Kurizki, “Photon-photon correlations and entanglement in doped photonic crystals,” *Phys. Rev. A*, vol. 64, p. 023810, 2001.
- [127] A. Ariv and P. Yeh, *Photonics*. Oxford U. Press, 2007.
- [128] M. J. Adams, *An Introduction to Optical Waveguides*. Wiley, 1981.
- [129] M. O. Scully and M. S. Zubairy, *Quantum Optics*. Cambridge U. Press, 1997.
- [130] J. J. Maki, M. S. Malcuit, J. E. Sipe, and R. W. Boyd, “Linear and nonlinear optical measurements of the Lorentz local field,” *Phys. Rev. Lett.*, vol. 67, p. 972, 1991.
- [131] M. R. Singh, *Recent Research Activities in Chemical Physics: From Atomic Scale to Macroscale*. Transworld Research Network, 2008.
- [132] D. G. Angelakis, E. Paspalakis, and P. L. Knight, “Transient properties of modified reservoir-induced transparency,” *Phys. Rev. A*, vol. 61, p. 055802, 2000.
- [133] M. R. Singh, “Anomalous electromagnetically induced transparency in photonic-band-gap materials,” *Phys. Rev. A*, vol. 70, p. 033813, 2004.
- [134] T. Yoshie, A. Scherer, J. Hendrickson, G. Khitrova, H. M. Gibbs, G. Rupper, C. Ell, O. B. Shchekin, and D. G. Deppe, “Vacuum Rabi splitting with a single quantum dot in a photonic crystal nanocavity,” *Nature*, vol. 432, p. 200, 2004.
- [135] K. Hennessy, A. Badolato, M. Winger, D. Gerace, M. Atatüre, S. Gulde, S. Fält, E. L. Hu, and A. Imamoglu, “Quantum nature of a strongly coupled single quantum dot-cavity system,” *Nature*, vol. 445, p. 896, 2007.
- [136] V. A. Sautenkov, Y. V. Rostovtsev, and E. R. Eliel, “Observation of narrow Autler-Townes components in the resonant response of a dense atomic gas,” *Phys. Rev. A*, vol. 78, p. 013802, 2008.
- [137] I. Diukman, L. Tzabari, N. Berkovitch, N. Tessler, and M. Orenstein, “Controlling absorption enhancement in organic photovoltaic cells by patterning Au nano disks within the active layer,” *Opt. Express*, vol. 19, p. A64, 2011.



- [138] Y. Liu, F. Qin, Z. Wei, Q. Meng, D. Zhang, and Z. Li, "10 fs ultrafast all-optical switching in polystyrene nonlinear photonic crystals," *Appl. Phys. Lett.*, vol. 95, p. 131116, 2009.
- [139] A. Hatef, S. M. Sadeghi, and M. R. Singh, "Plasmonic electromagnetically induced transparency in metallic nanoparticle-quantum dot hybrid systems," *Nanotechnology*, vol. 23, p. 065701, 2012.
- [140] I. Haque and M. R. Singh, "A study of the ac Stark effect in doped photonic crystals," *J. Phys. Condens. Matter*, vol. 19, p. 156229, 2007.
- [141] L. Novotny and B. Hecht, *Principles of Nano-optics*. Cambridge U. Press, 2006.
- [142] C. V. Vlack, P. T. Kristensen, and S. Hughes, "Spontaneous emission spectra and quantum light-matter interactions from a strongly coupled quantum dot metal-nanoparticle system," *Phys. Rev. B*, vol. 85, p. 075303, 2012.
- [143] J. Yan, W. Zhang, S. Duan, X. Zhao, and A. O. Govorov, "Optical properties of coupled metal-semiconductor and metal-molecule nanocrystal complexes: Role of multipole effects," *Phys. Rev. B*, vol. 77, p. 165301, 2008.
- [144] P. Guyot-Sionnest, "Intraband spectroscopy and semiconductor nanocrystals," *Struct. Bond.*, vol. 118, p. 59, 2005.
- [145] A. Pandey and P. Guyot-Sionnest, "Slow electron cooling in colloidal quantum dots," *Science*, vol. 322, p. 929, 2005.
- [146] G. P. Acuna, M. Bucher, I. H. Stein, C. Steinhauer, A. Kuzyk, P. Holzmeister, R. Schreiber, A. Moroz, F. D. Stefani, T. Liedl, F. C. Simmel, and P. Tinnefeld, "Distance dependence of single-fluorophore quenching by gold nanoparticles studied on DNA origami," *ACS Nano*, vol. 6, p. 3189, 2012.
- [147] A. O. Govorov, "Semiconductor-metal nanoparticle molecules in a magnetic field: Spin-plasmon and exciton-plasmon interactions," *Phys. Rev. B*, vol. 82, p. 155322, 2010.
- [148] M. Kerker, *The Scattering of Light and Other Electromagnetic Radiation*. Academic Press, New York, 1969.
- [149] D. J. Norris, A. Sacra, C. B. Murray, and M. G. Bawendi, "Measurement of the size dependent hole spectrum in CdSe quantum dots," *Phys. Rev. Lett.*, vol. 72, p. 2612, 1994.
- [150] M. Cheng, S. Liu, and Q. Wang, "Modulating emission polarization of semiconductor quantum dots through surface plasmon of metal nanorod," *Appl. Phys. Lett.*, vol. 92, p. 162107, 2008.
- [151] A. Mohan, M. Felici, P. Gallo, B. Dwir, A. Rudra, J. Faist, and E. Kapon, "Polarization-entangled photons produced with high-symmetry site-controlled quantum dots," *Nat. Photonics*, vol. 4, p. 302, 2010.

# Copyright and Reprint Permissions

## Solid State Communications (chapter 3)

### ELSEVIER LICENSE TERMS AND CONDITIONS

This is a License Agreement between Daniel G Schindel (“You”) and Elsevier (“Elsevier”) provided by Copyright Clearance Center (“CCC”). The license consists of your order details, the terms and conditions provided by Elsevier, and the payment terms and conditions.

All payments must be made in full to CCC. For payment instructions, please see information listed at the bottom of this form.

Supplier	Elsevier Limited The Boulevard,Langford Lane Kidlington,Oxford,OX5 1GB,UK
Registered Company	1982084
Customer name	Daniel G Schindel
Customer address	291 Windermere Rd. Apt. 113
License Number	3024230721549
License date	Nov 08, 2012
Licensed content publisher	Elsevier
Licensed content publication	Solid State Communications
Licensed content title	The theory of cylindrical photonic wires
Licensed content author	Mahi R. Singh,Daniel Schindel
Licensed content date	April 2011
Licensed content volume number	151
Licensed content issue number	7
Number of pages	5
Start Page	582
End Page	586
Type of Use	reuse in a thesis/dissertation
Intended publisher of new work	other
Portion	full article

Format	electronic
Are you the author of this Elsevier article?	Student Research Award University of Manitoba
Will you be translating?	2002
Order reference number	
Title of your thesis/dissertation	The Study of Optoelectronics in Semiconductor and Metallic Nanoparticle Hybrid Systems
Expected completion date	Dec 2012
Estimated size (number of pages)	138

## Journal of the Optical Society of America B (chapter 4)

Dear Daniel,

Thank you for contacting The Optical Society

Because you are the author of the source paper which you wish to reproduce, OSA considers your requested use of its copyrighted materials to be permissible within the author rights granted in the Copyright Transfer Agreement submitted by the requester on acceptance for publication of his/her manuscript.

It is requested that a complete citation of the original material be included in any publication.

Please let me know if you have any questions.

Best,

Hannah

Hannah Bembia

June 27, 2012

Authorized Agent, The Optical Society

From: Daniel Grant Schindel

Sent: Wednesday, June 27, 2012 12:19 PM

To: pubscopyright

Subject: Permission to use article in thesis

Date: June 27, 2012

Re: Permission to Use Copyrighted Material in a Doctoral Thesis

To whom it may concern,

I am a University of Western Ontario graduate student completing my Doctoral thesis entitled "Quantum Coherence and Interference in Photonic Heterostructures and Hybrid Systems". My thesis will be available in full-text on the internet for reference, study and / or copy. Except in situations where a thesis is under embargo or restriction, the electronic version will be accessible through the Western Libraries web pages, the Library's web catalogue, and also through web search engines. I will also be granting Library and Archives Canada and ProQuest/UMI a non-exclusive license to reproduce, loan, distribute, or sell single copies of my thesis by any means and in any form or format. These rights will in no way restrict republication of the material in any other form by you or by others authorized by you.

I would like permission to allow inclusion of the following material in my thesis: "Photon absorption in interacting quantum dots doped in nanofibers" in the Journal of the Optical Society of America B, Volume 27, Number 12, page 2759 (2010)

The material will be attributed through a citation.

Please confirm in writing or by email that these arrangements meet with your approval.

Sincerely,

Daniel

Schindel

## Applied Physics Letters (chapter 5)

Dear Dr. Schindel

Thank you for requesting permission to reproduce material from American Institute of Physics publications.

Permission is granted – subject to the conditions outlined below – for the following:

“Controlling the photoluminescence of acceptor and donor quantum dots embedded in a nonlinear photonic crystal” in Applied Physics Letters, Volume 101, page 051115 (2012)

To be used in the following manner:

Reproduced in your thesis for submission to the University of Western Ontario. It is understood that your thesis will be available in full-text on the internet for reference, study and/or copy, the electronic version will be accessible through the Western Libraries web pages, the Library’s web catalogue, and also through web search engines, and you will also be granting Library and Archives Canada and ProQuest/UMI a non-exclusive license to reproduce, loan, distribute, or sell single copies by any means and in any form or format.

1. The American Institute of Physics grants you non-exclusive world rights in all languages and media.

2. This permission extends to all subsequent and future editions of the new work.

3. The following copyright notice must appear with the material (please fill in the information indicated by capital letters): “Reprinted with permission from [FULL CITATION]. Copyright [PUBLICATION YEAR], American Institute of Physics.” Full citation format is as follows: Author names, journal title, Vol. #, Page #, (Year of publication). For an article, the copyright notice must be printed on the first page of the article or book chapter. For figures, photographs, covers, or tables, the notice may appear with the material, in a footnote, or in the reference list.

4. This permission does not apply to any materials credited to sources other than the copyright holder.

Please let us know if you have any questions.

Sincerely,

Susann

Brailey

Manager, Rights and Permissions

American Institute of Physics

Suite 1NO1

2 Huntington Quadrangle

Melville, NY 11747-4502

Phone: 1-516-576-2268

Fax: 1-516-576-2450

Email: (withheld)

From: Daniel Grant Schindel

Sent: Thursday, November 08, 2012 8:11 AM

To: AIPRights Permissions Subject:

RE: Permission to use article in my thesis

Dear Susann,

I am a University of Western Ontario graduate student completing my Doctoral thesis entitled “Quantum Coherence and Interference in Photonic Heterostructures and Hybrid Systems”. My thesis will be available in full-text on the internet for reference, study and / or copy. Except in situations where a thesis is under embargo or restriction, the electronic version will be accessible through the Western Libraries web pages, the Library’s web catalogue, and also through web search engines. I will also be granting Library and Archives Canada and ProQuest/UMI a non-exclusive license to reproduce, loan, distribute, or sell single copies of my thesis by any means and in any form or format. These rights will in no way restrict republication of the material in any other form by you or by others authorized by you.

I would like permission to allow inclusion of the following material in my thesis: “Controlling the photoluminescence of acceptor and donor quantum dots embedded in a nonlinear photonic crystal” in Applied Physics Letters, Volume 101, page 051115 (2012)

The material will be attributed through a citation.

Please confirm in writing or by email that these arrangements meet with your approval.

Sincerely,

Daniel

Schindel

## Applied Physics Letters (chapter 7)

Dear Dr. Schindel:

Thank you for requesting permission to reproduce material from American Institute of Physics publications.

Permission is granted – subject to the conditions outlined below – for the following:

“Dipole-dipole interaction in a quantum dot and metallic nanorod hybrid system” Applied Physics Letters, Volume 99, page 181106 (2011)

To be used in the following manner:

Reproduced in your thesis for submission to the University of Western Ontario. It is understood that your thesis will be available in full-text on the internet for reference, study and/or copy, the electronic version will be accessible through the Western Libraries web pages, the Library’s web catalogue, and also through web search engines, and you will also be granting Library and Archives Canada and ProQuest/UMI a non-exclusive license to reproduce, loan, distribute, or sell single copies by any means and in any form or format.

1. The American Institute of Physics grants you non-exclusive world rights in all languages and media.

2. This permission extends to all subsequent and future editions of the new work.

3. The following copyright notice must appear with the material (please fill in the information indicated by capital letters): “Reprinted with permission from [FULL CITATION]. Copyright [PUBLICATION YEAR], American Institute of Physics.”

Full citation format is as follows: Author names, journal title, Vol. #, Page #, (Year of publication).

For an article, the copyright notice must be printed on the first page of the article or book chapter. For figures, photographs, covers, or tables, the notice may appear with the material, in a footnote, or in the reference list.

4. This permission does not apply to any materials credited to sources other than the copyright holder.

Please let us know if you have any questions.

Sincerely,

Susann Brailey

Manager,

Rights and Permissions

American Institute of Physics

Suite 1NO1

2 Huntington Quadrangle Melville, NY 11747-4502

Phone: 1-516-576-2268

Fax: 1-516-576-2450

Email: (withheld)

From: Daniel Grant Schindel

Sent: Wednesday, June 27, 2012 12:23 PM

To: (withheld)

Subject: Permission to use article in my thesis

Date: June 27, 2012

Re: Permission to Use Copyrighted Material in a Doctoral Thesis

To whom it may concern,

I am a University of Western Ontario graduate student completing my Doctoral thesis entitled “Quantum Coherence and Interference in Photonic Heterostructures and Hybrid Systems”. My thesis will be available in full-text on the internet for reference, study and / or copy. Except in situations where a thesis is under embargo or restriction, the electronic version will be accessible through the Western Libraries web pages, the Library’s web catalogue, and also through web search engines. I will also be granting Library and Archives Canada and ProQuest/UMI a non-exclusive license to reproduce, loan, distribute, or sell single copies of my thesis by any means and in any form or format. These rights will in no way restrict republication of the material in any other form by you or by others authorized by you.

I would like permission to allow inclusion of the following material in my thesis: “Dipole-dipole interaction in a quantum dot and metallic nanorod hybrid system” in Applied Physics Letters, Volume 99, page 181106 (2011)

The material will be attributed through a citation.

Please confirm in writing or by email that these arrangements meet with your approval.

Sincerely,

Daniel

Schindel



# Curriculum Vitae

**Name:** Daniel Schindel

**Post-Secondary Education and Degrees:** University of Manitoba  
Winnipeg, Manitoba, Canada  
2000 - 2004 B. Sc.

Michigan State University  
East Lansing, Michigan, USA  
2004 - 2007 M. Sc.

University of Western Ontario  
London, Ontario, Canada  
2008 - 2012 Ph. D.

**Honours and Awards:** Canadian Association of Physicists  
Prize Exam Award  
University of Manitoba  
2000

Reginald K. Groome Memorial  
Scholarship  
Scouts Canada  
2001

Faculty of Science Undergraduate  
Student Research Award  
University of Manitoba  
2002

NSERC Undergraduate Research  
Award  
NSERC  
2003

Department of Physics and Astronomy  
Award of Excellence in Administration  
University of Western Ontario  
2010 - 2011

**Related Work Experience:** Teaching Assistant  
The University of Manitoba  
2002 - 2004

Teaching Assistant  
Michigan State University  
2004 - 2007

Science Demonstrator (K - 6)  
Mad Science  
2008

Teaching Assistant  
University of Western Ontario  
2008 - 2012

### **Publications:**

M. R. Singh, C. Racknor, and **D. G. Schindel**, "Controlling the photoluminescence of acceptor and donor quantum dots embedded in a nonlinear photonic crystal," *Appl. Phys. Lett.*, vol. 101, p. 051115, 2012.

M. R. Singh, **D. G. Schindel**, and A. Hatef, "Dipole-dipole interaction in a quantum dot and metallic nanorod hybrid system," *Appl. Phys. Lett.*, vol. 99, p. 181106, 2011.

M. R. Singh and **D. G. Schindel**, "The theory of cylindrical photonic wires," *Solid State Commun.*, vol. 151, p. 582, 2011.

M. R. Singh and **D. G. Schindel**, "Photon absorption in interacting quantum dots doped in nanofibers," *J. Opt. Soc. Am. B*, vol. 27, p. 2759, 2010.

P. D. Loly, I. Cameron, W. Trump, and **D. G. Schindel**, "Magic Square Spectra," *Linear Algebra Appl.*, vol. 430, p. 2659, 2009

**D. G. Schindel**, M. Rempel, and P. D. Loly, "Enumerating the bent diagonal squares of Dr. Benjamin Franklin FRS," *Proc. R. Soc. London Ser. A*, vol. 462, p. 2271, 2006.

J. M. Vail, **D. G. Schindel**, A. Yang, O. Penner, R. Pandey, H. Jiang, M. A. Blanco, A. Costales, Q. C. Qiu, and Y. Xu, "Effect of dielectric polarization on the properties of charged point defects in insulating crystals: the nitrogen vacancy in AlN," *J. Phys. Condens. Matter*, vol. 16, p. 3371, 2004.